Springer ThesesRecognizing Outstanding Ph.D. Research

Mi Li

Investigations of Cellular and Molecular Biophysical Properties by Atomic Force Microscopy Nanorobotics



Springer Theses

Recognizing Outstanding Ph.D. Research

Aims and Scope

The series "Springer Theses" brings together a selection of the very best Ph.D. theses from around the world and across the physical sciences. Nominated and endorsed by two recognized specialists, each published volume has been selected for its scientific excellence and the high impact of its contents for the pertinent field of research. For greater accessibility to non-specialists, the published versions include an extended introduction, as well as a foreword by the student's supervisor explaining the special relevance of the work for the field. As a whole, the series will provide a valuable resource both for newcomers to the research fields described, and for other scientists seeking detailed background information on special questions. Finally, it provides an accredited documentation of the valuable contributions made by today's younger generation of scientists.

Theses are accepted into the series by invited nomination only and must fulfill all of the following criteria

- They must be written in good English.
- The topic should fall within the confines of Chemistry, Physics, Earth Sciences, Engineering and related interdisciplinary fields such as Materials, Nanoscience, Chemical Engineering, Complex Systems and Biophysics.
- The work reported in the thesis must represent a significant scientific advance.
- If the thesis includes previously published material, permission to reproduce this must be gained from the respective copyright holder.
- They must have been examined and passed during the 12 months prior to nomination.
- Each thesis should include a foreword by the supervisor outlining the significance of its content.
- The theses should have a clearly defined structure including an introduction accessible to scientists not expert in that particular field.

More information about this series at http://www.springer.com/series/8790

Investigations of Cellular and Molecular Biophysical Properties by Atomic Force Microscopy Nanorobotics

Doctoral Thesis accepted by University of Chinese Academy of Sciences, Beijing, China



Author
Dr. Mi Li
State Key Laboratory of Robotics, Shenyang
Institute of Automation
Chinese Academy of Sciences
Shenyang
China

Supervisor
Prof. Ning Xi
Shenyang Institute of Automation
Chinese Academy of Sciences
Shenyang
China

ISSN 2190-5053 ISSN 2190-5061 (electronic) Springer Theses ISBN 978-981-10-6828-7 ISBN 978-981-10-6829-4 (eBook) https://doi.org/10.1007/978-981-10-6829-4

Library of Congress Control Number: 2017955355

© Springer Nature Singapore Pte Ltd. 2018

This work is subject to copyright. All rights are reserved by the Publisher, whether the whole or part of the material is concerned, specifically the rights of translation, reprinting, reuse of illustrations, recitation, broadcasting, reproduction on microfilms or in any other physical way, and transmission or information storage and retrieval, electronic adaptation, computer software, or by similar or dissimilar methodology now known or hereafter developed.

The use of general descriptive names, registered names, trademarks, service marks, etc. in this publication does not imply, even in the absence of a specific statement, that such names are exempt from the relevant protective laws and regulations and therefore free for general use.

The publisher, the authors and the editors are safe to assume that the advice and information in this book are believed to be true and accurate at the date of publication. Neither the publisher nor the authors or the editors give a warranty, express or implied, with respect to the material contained herein or for any errors or omissions that may have been made. The publisher remains neutral with regard to jurisdictional claims in published maps and institutional affiliations.

Printed on acid-free paper

This Springer imprint is published by Springer Nature
The registered company is Springer Nature Singapore Pte Ltd.
The registered company address is 152 People Read #21 01/04 Cetavaya Fact Si

The registered company address is: 152 Beach Road, #21-01/04 Gateway East, Singapore 189721, Singapore

Supervisor's Foreword

Micro-/nanorobotics in biomedical applications is an emerging area expected to have tremendous impact on medical and pharmaceutical technologies, thus providing unprecedented opportunities for the development of robotics and automation. The achievement in physics, engineering, and nanotechnology in the past decades has led to the birth of various robots with the capabilities to perform manipulations at the micro-/nanometer scale. Among these robots, due to the unique advantages (including nanometer spatial resolution, piconewton force sensitivity, and its ability to work in liquids), atomic force microscopy (AFM)-based nanorobotics is particularly appropriate for detecting behaviors of living cells. However, studies on utilizing AFM nanorobotics to detect cellular and molecular behaviors involved in the physiological processes of real-world clinical environment have been scarce. By combining engineering with clinical applications, this research focuses on the detection of cellular and molecular biophysical properties involved in lymphoma rituximab targeted therapy based on AFM nanorobotics.

The scientific achievement in this thesis could be divided into several parts. First, an efficient immobilization method based on micropillar/microwell mechanical trapping and poly-L-lysine electrostatic adsorption is developed for observing the ultra-microstructures on the surface of lymphoma cells, remarkably improving the detection precision of AFM nanorobotics on living mammalian suspended cells. Second, series methods are established for reliably detecting the multiple biophysical parameters of single cells and single molecules, including cellular topography, cellular mechanics, molecular binding affinity, and molecular distribution density on cell surface, all laying a solid foundation for the biomedical applications of AFM nanorobotics. Finally, biochemical methods based on cellular surface-specific markers are developed for recognizing cancerous cells from the biopsy samples of lymphoma patients, and the molecular interactions taking place in the primary cancerous cells and normal cells are quantitatively detected by the established AFM single-cell and single-molecule methods, which are significantly correlated with the clinical therapeutic outcomes of patients treated with rituximab. This thesis has enabled AFM nanorobotics to effectively detect in situ cellular and molecular biophysical properties in their native states, facilitating further development of nanorobotics-based methods in biomedical applications. The preliminary experimental results on primary cells from biopsy samples of patients demonstrate the active role of AFM nanorobotics in predicting efficacies of targeted drugs, which provide novel insights into robotic medical treatment at the micro-/nanoscale. These remarkable achievements have ranked his thesis as an Outstanding Doctoral Dissertation by Chinese Academy of Sciences.

Over the past years while Dr. Li was working his thesis, I have witnessed his extraordinary dedication to research. He distinguished himself by completing well-researched experiment. Dr. Li is very personal, and I absolutely have enjoyed interacting with him.

Not only as his academic advisor, but also a researcher in the field, it is my pleasure to recommend Dr. Li's thesis to readers, in particular those specializing and/or interested in the related areas.

Shenyang, China August 2017 Prof. Ning Xi

Parts of this thesis have been published in the following journal articles:

- 1. **Li M**, Liu L, Xi N, Wang Y (2017) Applications of micro/nano automation technology in detecting cancer cells for personalized medicine. IEEE Trans Nanotechnol 16: 217–229.
- 2. **Li M**, Liu L, Xi N, Wang Y (2016) Applications of atomic force microscopy in exploring drug actions in lymphoma-targeted therapy at the nanoscale. Bionanoscience 6: 22–32.
- 3. **Li M**, Xiao X, Liu L, Xi N, Wang Y (2016) Rapid recognition and functional analysis of membrane proteins on human cancer cells using atomic force microscopy. J Immunol Methods 436: 41–49.
- 4. **Li M**, Liu L, Xi N, Wang Y, Xiao X, Zhang W (2015) Quantitative analysis of drug-induced complement-mediated cytotoxic effect on single tumor cells using atomic force microscopy and fluorescence microscopy. IEEE Trans Nanobioscience 14: 84–94.
- 5. **Li M**, Liu L, Xi N, Wang Y, Xiao X, Zhang W (2014) Nanoscale imaging and mechanical analysis of Fc receptor-mediated macrophage phagocytosis against cancer cells. Langmuir 30: 1609–1621.
- 6. **Li M**, Xiao X, Zhang W, Liu L, Xi N, Wang Y (2014) Nanoscale distribution of CD20 on B-cell lymphoma tumour cells and its potential role in the clinical efficacy of rituximab. J Microsc 254: 19–30.
- 7. **Li M**, Xiao X, Zhang W, Liu L, Xi N, Wang Y (2014) AFM analysis of the multiple types of molecular interactions involved in rituximab lymphoma therapy on patient tumor cells and NK cells. Cell Immunol 290: 233–244.
- 8. **Li M**, Xiao X, Liu L, Xi N, Wang Y, Dong Z, Zhang W (2013) Atomic force microscopy study of the antigen-antibody binding force on patient cancer cells based on ROR1 fluorescence recognition. J Mol Recognit 26:432–438.
- 9. **Li M**, Xiao X, Liu L, Xi N, Wang Y, Dong Z, Zhang W (2013) Nanoscale mapping and organization analysis of target proteins on cancer cells from B-cell lymphoma patients. Exp Cell Res 319: 2812–2821.
- 10. **Li M**, Liu L, Xi N, Wang Y, Xiao X, Zhang W (2013) Imaging and measuring the biophysical properties of Fc gamma receptors on single macrophages using atomic force microscopy. Biochem Biophys Res Commun 438: 709–714.
- 11. **Li M**, Liu L, Xi N, Wang Y, Dong Z, Xiao X, Zhang W (2013) Atomic force microscopy imaging of live mammalian cells. Sci China Life Sci 56: 811–817.
- 12. **Li M**, Liu L, Xi N, Wang Y, Dong Z, Xiao X, Zhang W (2012) Atomic force microscopy imaging and mechanical properties measurement of red blood cells and aggressive cancer cells. Sci China Life Sci 55: 968–973.
- 13. **Li M**, Liu L, Xi N, Wang Y, Dong Z, Xiao X, Zhang W (2012) Drug-induced changes of topography and elasticity in living B lymphoma cells based on atomic force microscopy. Acta Phys Chim Sin 28: 1502–1508.
- 14. **Li M**, Liu L, Xi N, Wang Y, Dong Z, Tabata O, Xiao X, Zhang W (2011) Imaging and measuring the rituximab-induced changes of mechanical properties in B-lymphoma cells using atomic force microscopy. Biochem Biophys Res Commun 404: 689–694.

- 15. **Li M**, Liu L, Xi N, Wang Y, Dong Z, Li G, Xiao X, Zhang W (2011) Detecting CD20-rituximab interaction forces using AFM single-molecule force spectroscopy. Chin Sci Bull 56: 3829–3835.
- 16. **Li M**, Liu L, Xi N, Wang Y, Dong Z, Li G, Xiao X, Zhang W (2010) Detecting CD20-rituximab specific interactions on lymphoma cells using atomic force microscopy. Sci China Life Sci 53: 1189–1195.

Acknowledgements

I would like to express my sincere gratitude to my supervisor, Prof. Ning Xi, for his guidance throughout the journey of my Ph.D. study. His profound knowledge and visionary thinking has benefited my life. He is always giving me constructive suggestions and also has guided my academic career.

I would like to thank Prof. Lianqing Liu. From the day of my entry into SIA, I performed studies under his direct guidance. He has taught me many experimental skills and provided full support for my researches, which helped me to continuously forge ahead with my research.

I would like to thank Prof. Weijing Zhang and Dr. Xiubin Xiao from the Affiliated Hospital of Military Medical Academy of Sciences (Beijing, China), for their useful suggestions and support from the aspect of clinical medicine.

I would like to thank Prof. Yuechao Wang, Prof. Guangyong Li, Prof. Heping Chen, Prof. Jun Xi, Prof. Uche Weijinya, Prof. Osamu Tabata, Prof. Zhidong Wang, Prof. Hongyi Li, and Prof. Yandong Tang, for their valuable advice and comments on my research work.

I would like to thank the discussions with the present and former members of micro- and nanorobotics research group of SIA: Dr. Niandong Jiao, Dr. Haibo Yu, Dr. Wenxue Wang, Zhu Liu, Peng Yu, Lei Zhou, Yang Yang, Yan Li, Na Cong, Bin Liu, Minglin Li, Shuai Yuan, Yongliang Yang, Zhiqian Wang, Jing Hou, Zhikun Zhan, Shue Wang, Zhiyu Wang, Changlin Zhang, Peng Li, Yu Zhang, Dong Wang, Ping Yao, Zengxu Zhao, Zhibo Wang, Jialin Shi, Chuang Zhang, and so on.

I would like to thank the group of Prof. Enlong Ma from Shenyang Pharmaceutical University: Wenjiao Tai, Te Li, Pengfei Zhang, Wenyuan Shang, Ju Chen, Hui Zhang, and Mingjing Zheng, for their assistance about cell bioassay.

I would like to thank the staff of Personnel Department of SIA: Yuehong Ma, Lei Sun, Desheng Li, Luanli Xuan, and Qiang Ma, for their kind help during my studies.

x Acknowledgements

I appreciate the grant from National Natural Science Foundation of China (61503372, 60904095) and the Youth Innovation Promotion Association CAS (2017243).

My special thanks go to my family and my wife Jing Gao. Their constant love accompanies and supports me throughout my life. I would like to devote this thesis to them.

Shenyang, China Mi Li

Contents

1	mu	oduction to Atomic Force wheroscopy-based Nanorobotics	
	for 1	Biomedical Applications	1
	1.1	Background and Motivation	1
	1.2	Cellular Physiological Properties Detection	4
	1.3	Single-Cell and Single-Molecule Techniques	5
	1.4	Nanorobot Based on AFM	10
	1.5	Opportunities and Challenges	12
	1.6	Thesis Contents and Chapter Organization	14
	Refe	erences	16
2	Imn	nobilization Methods for Observing Living Mammalian	
		pended Cells by AFM	21
	2.1	•	21
	2.2	Biological Experiment Platform Based on AFM Nanorobot	22
	2.3	Immobilizing Mammalian Suspended Cells by Micropillar	
		Array	24
	2.4	Imaging Living Mammalian Suspended Cells Based	
		on Micro-Pillar Immobilization	26
	2.5	Imaging Living Mammalian Suspended Cells Based	
		on Micro-Well Immobilization	27
	2.6	Summary	29
	Refe	erences	30
3	Mea	suring the Mechanical Properties of Single Cells by AFM	33
	3.1	Current Status of Measuring Cell Mechanics by AFM	34
	3.2	Principle and Methods of Measuring Cell Mechanics	
		by AFM	35
	3.3	Fabrication of AFM Spherical Tip	39

xii Contents

	3.4		aring the Mechanics of Cancerous Cells with Different	40
	2.5		ve Abilities	
	3.5		ary	45 45
	Keit	erences		43
4	Sing	le-Mol	ecule Recognition and Force Measurements by AFM	49
	4.1	Currer	nt Status of AFM Single-Molecule Force Measurements	50
	4.2	Princip	ple of AFM Single-Molecule Force Spectroscopy	51
	4.3	Tip Fu	unctionalization and Verification	53
	4.4		rring the CD20-Rituximab Interaction Forces	56
		4.4.1	Purified CD20s on Mica	56
		4.4.2	Native CD20s on Lymphoma Cell	59
	4.5	Summ	ary	61
	Refe	erences		62
5	Mar	ning N	Membrane Proteins on Cell Surface by AFM	65
	5.1		nt Status of Mapping Membrane Proteins	00
	0.1		Il Surface by AFM	65
	5.2		Force Tapping AFM	66
	5.3		ing Protein Distributions by PFT	67
		5.3.1		68
		5.3.2		71
	5.4		ary	75
	Refe		····	76
6	Ann	lication	ns of AFM Cellular and Molecular Biophysical	
U			n Clinical Lymphoma Rituximab Treatment	79
	6.1		ar Ultra-Microstructure and Mechanics Detection	79
	0.1		PCD Mechanism	79
		6.1.2	ADCC Mechanism	83
		6.1.3	CDC Mechanism	91
	6.2		ag Target Proteins on Primary Cells from Clinical	71
	0.2		homa Patients	99
		6.2.1	Detecting CD20-Rituximab Interactions on Patient	- //
		0.2.1	Cancerous Cells	99
		6.2.2	Detecting FcR-Rituximab Interactions on Patient	
		0.2.2	Effector Cells	110
	6.3	Comp	arison of AFM Detection Results and Clinical	110
	0.0		peutic Outcomes	119
		6.3.1	CD20-Rituximab Interaction on Patient Cancerous Cells	
			and Clinical Efficacies	119
		6.3.2	FcR-Rituximab Interaction Patient Effector Cells	
		2.2 .2	and Clinical Efficacies	120
	6.4	Summ	ary	125
	Dof			

Contents	xiii
----------	------

7	Cone	clusion and Future Work	129
	7.1	Conclusion	129
	7.2	Future Work	130
	Refe	rences	132
Cu	rricu	lum Vitae	133

Chapter 1 Introduction to Atomic Force Microscopy-Based Nanorobotics for Biomedical Applications

1.1 Background and Motivation

The threat to human health from cancers is becoming increasingly serious [1-3]. About 14.1 million new cancer cases and 8.2 million deaths occurred in 2012 worldwide [2]. By 2030 the incidence of cancer cases will increase to 22.2 million and the cancer-related deaths will increase to 13.2 million [3]. The struggle between mankind and cancer has a long history. The first description of a disease resembling cancer is found in Egyptian papyri and dates back to about 1600 BC, but until the nineteenth century when anaesthesia allowed painless surgery, cancer was more or less regarded as incurable [4]. Afterwards, the discovery of X-ray (1900s) and nitrogen mustard (1940s) leads to radiotherapy and chemotherapy respectively [5]. These three traditional cancer treatments (surgery, radiotherapy, and chemotherapy) have obvious disadvantages, e.g., the treatments are often not complete, the cancers are prone to metastasis and recurrence, and the toxic and side effects are severe. The development of modern biotechnology significantly improves our understanding of cancer, and molecular targeted treatments which aim at cancerous cells come true in the past two decades. The clinical practice demonstrates that molecular targeted therapy possesses huge potential in treating cancers, but also indicates that molecular targeted therapy has its indications and drug resistance problem. Due to the progress of biomedicine, now we know more about the pathogenesis of cancers. The treatment method of cancer is becoming diverse and the quality of life of cancer patients is improving. However, we are still unclear about the cause of cancers (the only cancer we know the cause is cervical carcinoma [6]). It is disappointing that the age-adjusted mortality rate for cancer is about the same in the 21st century as it was 50 years ago [7]. There is still a long way to go before we totally conquer cancer. For China, modernization has made glorious achievements in the past forty years and people's living standards continue to improve. Health has become a more and more hot topic of concern to the broad masses of the people. Since the 1970s, the incidence and mortality of cancer has been increasing in China.

1

Cancer is becoming the leading cause of death in China since 2010 [8]. Cancer prevention and treatment has become an important issue needing to be solved urgently in the field of biomedicine, which is of great significance for maintaining social stability, improving the quality of people's life, and promoting the healthy development of economy.

Non-Hodgkin's lymphoma (NHL) is a class of malignant tumor, accounting for 4% of all cancers [9]. Approximately 85% of NHL in adults are of B cell origin [10]. In 1997 rituximab was approved by Food and Drug Administration (FDA) in USA for treating B-cell NHL. Rituximab is the first monoclonal antibody drug approved for treating cancers. The target of rituximab is the CD20 antigen on the surface of B cell. In vitro experiments demonstrate that the binding of rituximab to CD20 causes the lysis of target cells via three main mechanisms, including antibody dependent cellular cytotoxicity (ADCC), complement dependent cytotoxicity (CDC), and programmed cell death (PCD) [11, 12], as shown in Fig. 1.1. Although the in vivo mechanisms of rituximab are still unknown, rituximab achieves unprecedented success in clinical practice. The use of rituximab in combination

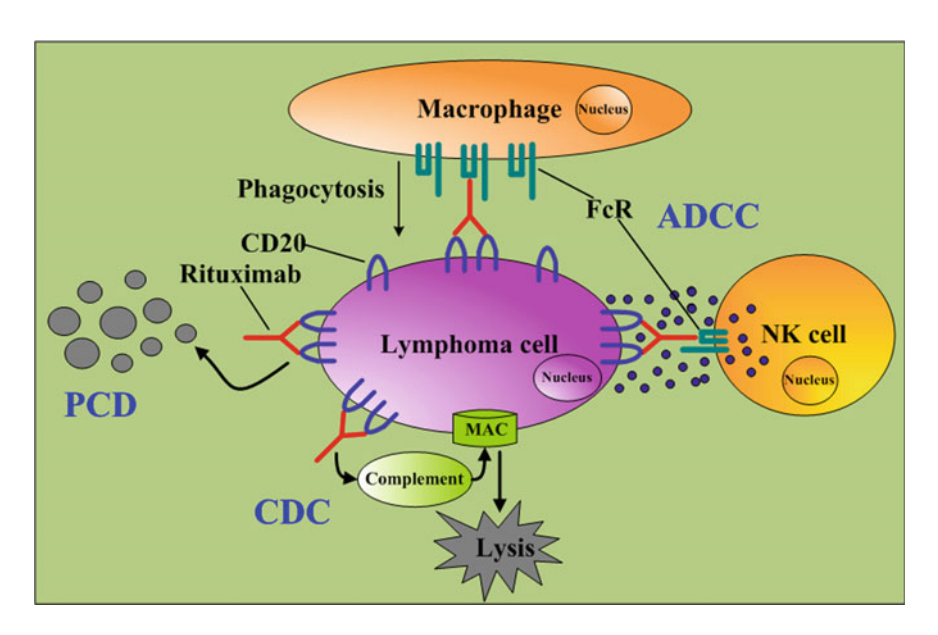


Fig. 1.1 The three killing mechanisms of rituximab [12]. The binding of rituximab to the CD20 on the lymphoma cell can directly induce the programmed cell death (PCD) of the lymphoma cell. Besides, the binding can trigger the classical pathway of complement-dependent cytotoxicity (CDC). The final products of CDC are the membrane attack complexes (MACs), which lead to the lysis of the cells. After the binding of rituximab to CD20 on the lymphoma cell, the F_c portion of rituximab can bind to the F_c receptors on the surface of effector cells (e.g., NK cell and macrophage) and these effector cells can then attack the target cells (e.g., NK cells release cytotoxin to kill the cell and macrophages kill the cell via phagocytosis)

with conventional chemotherapy significantly improves the overall remission rates and long-term survival rates of NHL patients [13, 14]. Rituximab (used alone or combined with chemotherapy) has now become the standard treatment of B-cell NHL [15]. The use of rituximab greatly improves the life quality of NHL patients, but there are still many patients who are insensitive or develop resistance to rituximab, and thus the current challenge lies in how to provide effective therapy for these patients [16]. Researchers have presented several mechanisms that may cause rituximab resistance, e.g., downregulation of CD20, blocking the activation of complement, and impaired rituximab-mediated ADCC, but the exact contribution of these mechanisms to the clinical phenomenon of rituximab resistance is difficult to evaluate [17]. Many second generation antibodies (humanized with unmodified Fc domain to reduce immunogenicity) and third generation antibodies (humanized with engineered Fc domain to improve the effector functions) have been developed (e.g., Ofatumumab, Ocrelizumab, Veltuzumab, AME-133V, PRO131921) and entered the clinical trials [18]. But the true efficacies of these antibodies on rituximab resistance patients remain to be tested in clinical practice [16] and so far none of the newer anti-CD20 antibodies have been shown to be clinically more effective than rituximab in a direct comparison [15].

In order to develop anti-CD20 monoclonal antibodies with enhanced potency to provide effective therapies for the patients who develop resistance to rituximab, we need to thoroughly understand the underlying mechanisms causing the different clinical therapeutic outcomes of rituximab treatment. Traditional drug assays are based on the tests performed on a large number of cells and the results of these cells are then statistically averaged [19]. This method provides a wealth of information about cellular processes, but also has obvious disadvantages. The results only reflect the averaged behaviors of the ensemble cells, and the unique behaviors of small sub-populations or individual cells are masked [20]. Tumor formation involves the co-evolution of cancerous cells together with micro-environments, including extracellular matrix, tumor vasculature and immune cells [21]. The complex interactions between cancerous cells and micro-environments are important causes of tumor heterogeneity. Studies have shown that not only there are genetic and phenotypic variations between patients with the same tumor type (this is called intertumor heterogeneity), but also there are differences between the cancerous cells within the same tumor (this is called intratumor heterogeneity) [22]. This heterogeneity of cancerous cells is closely related to the drug resistance of tumors in the clinic [23]. In the coming era of precision medicine, the success of personalized medicine depends on having accurate diagnostic tests that identify patients who can benefit from targeted therapies [24]. Hence, in 2012, researchers have pointed out that investigating cell-to-cell variability is a new era in molecular biology [25]. Probing the physiological activities at the single-cell level can reveal novel regulatory mechanisms for diverse cellular processes, which may be of great significance for us to better understand drug resistance of cancers and eventually achieve the personalized treatment of cancers.

1.2 Cellular Physiological Properties Detection

Cells are the structural and functional unit of living organisms. As the cytologist E.B. Wilson said at the outset of his influential book *The cell in development and heredity*: the key to all ultimate biological problems must, in the last analysis, be sought in the cell [26]. Cells are composed of various biomolecules, including proteins, DNAs, RNAs, carbohydrates, and lipids. These biomolecules interact with each other to fulfill the various cellular biological functions, and thus maintain the normal functioning of tissues, organs and living organisms. The cell states are closely related to the health of living organisms. Deviations of cells from their normal states may lead to the pathogenic changes of cells, which can then result in diseases. Hence detecting cellular physiological properties is of great significance for revealing life mysterious, guiding clinical practice and promoting drug development.

Observing cellular morphology is one of the most important methods for cell assays. There are various types of cells in the human body, and each type of cell has its unique morphology. Cell morphology is closely related to the physiological functions of the cell [27]. Normal erythrocytes are biconcave disks (Fig. 1.2a) [28], which facilitates erythrocytes to carry oxygen; neurons are filamentous, which facilitates them to deliver signal. When pathogenic changes occur inside the cell, cellular morphology often changes. For sickle cell anemia patients, their erythrocytes are sickle (Fig. 1.2b) [28] and the capability of carrying oxygen is only half that of normal erythrocytes. There are significant differences between the morphology of cancerous cells and their normal counterparts, including geometry (e.g., size, volume, shape), cell nucleus (e.g., size, shape, number of nucleus, nucleus-cytoplasm ratio) (Fig. 1.2c, d) [29], and cell surface ultra-microstructures (Fig. 1.2e, f) [30]. In fact, the main methods in the clinic for pathological diagnosis are based on the cellular morphological observations of paraffin sections.

Recent studies have shown that cell mechanics plays an important role in maintaining cellular physiological functions [31]. Cells sense the external mechanical stimuli through the surface proteins and convert the mechanical signals into intracellular chemical signals to regulate the physiological activities of cells [32].

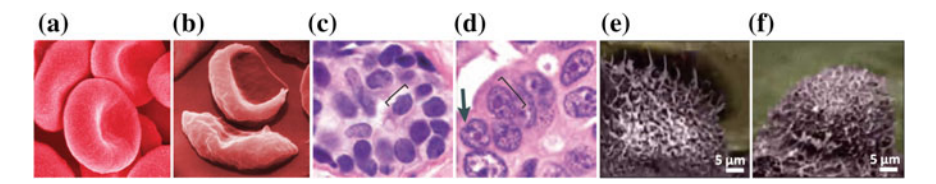


Fig. 1.2 Cellular morphology is closely related to cellular functions. Erythrocytes from healthy volunteers (a) and from sickle cell anemia patients [28] (b). Nucleus of normal breast cells (c) and cancerous breast cells (d). Reprinted with permission from [29]. Copyright 2012 Macmillan Publishers Limited. Cell surface brush of cervical cancerous cells (e) and cervical normal cells (f). Reprinted with permission from [30]. Copyright 2009 Macmillan Publishers Limited

The pathologic changes inside the cell can result in the changes of cellular mechanical properties [33]. In 2007, Suresh summarized the relationship between cell mechanics and cancer development [34]. Suresh pointed out that pathologic changes can result in the changes of cell mechanics (e.g., deformability, cytoadherence, stiffness) and induce the changes of cell physiological properties (e.g., protein expression, viability, proliferation, locomotion), which eventually cause the formation of cancers. It is reported that the cancerous cells are significantly softer than normal cells [35], and the stiffness profile of tumor tissues remarkably changes at the different stages (normal tissue, benign lesion, invasive cancer) of cancer development [36], showing that cell mechanics is a label-free biomarker for indicating cell states.

Due to the reliable efficacy, low toxicity, and less side effects, molecular targeted therapy has become an important strategy in clinical cancer treatment. So far more than 25 monoclonal antibodies have been approved worldwide and novel monoclonal antibodies are entering clinical trials at a rate of nearly 40 per year [37, 38], greatly promoting the development of molecular targeted therapy. In molecular targeted therapy, monoclonal antibodies bind to the target molecules specifically expressed on the surface of cancerous cell, which can then deplete the cancerous cells via immune mechanisms, such as the binding of rituximab to CD20 on lymphoma cell shown in Fig. 1.1. Antibody-target interactions directly influence the therapeutic outcomes of antibodies. The larger binding strength between antibody molecules and target molecules allows the longer time the antibody molecules reside on the cell surface, meaning the longer time of actions of antibody molecules. The larger number of target molecules on cancerous cells can recruit more antibody molecules binding to the cell surface, which results in enhanced efficacies. Hence, investigating antibody-target interactions at the single-molecule level can improve our understanding of antibody actions, which is useful for complementing drug development.

1.3 Single-Cell and Single-Molecule Techniques

The above text presents the significance of cellular physiological properties detection (cell morphology, cell mechanics, and molecular interactions). This section will review the current typical single-cell and single-molecule techniques. Looking at the history of exploring cells, we can easily find that our understanding of cells always deepens with the continuous progress of observation methods. Before the advent of optical microscope, humans cannot observe the cell, since the spatial resolution of human eyes is about 0.2 mm, whereas the diameter of most animal and plant cells is in the range of 20–30 µm. The invention of optical microscope allows cells to be observed by humans. In 1665, English scientist Robert Hooke, who game us Hooke's law of elasticity, firstly observed the cell walls of cork cells using a compound microscope and gave us the word "cell" in his book *Micrographia* [39]. In 1674, Dutch businessman Anton Philips van

Leeuwenhoek firstly observed the living cells via a microscope consisting of a single high-quality lens. Due to the limit of light wavelength, the limit resolution of the conventional optical microscope is 200 nm. Though the resolution of improved optical microscope can reach 100 nm [40], it is still difficult to meet our requirements of observing the fine structures of cells, as the single protein molecules on cell membrane are only several nanometer [41]. In 1931, German physicist Ernst Ruska invented the electron microscope (EM) [42]. EM obtains the topography of samples using electron beam whose wavelength is much shorter than that of visible light. The spatial resolution of EM can be 0.1 nm [43], allowing us to observe the ultra-microstructures of cells. However, the imaging condition of EM is vacuum which requires that samples be fixed and dried. Thus EM cannot observe living cells. Environmental scanning electron microscope (ESEM) can observe samples containing certain moisture, but there is still a big gap between the conditions in ESEM (0 °C, 600 Pa pressure) [44] and the real environments (37 °C, standard atmosphere) living cells reside in. Especially for relatively fragile samples, such as living cell, ESEM cannot directly image them and often requires chemical fixation [45]. Besides, the water membrane covered on cell surface usually makes it difficult to detect the fine structures of cell surface [46], resulting in the low spatial resolution (the maximum resolution was about 1 nm [47]).

In 1986, Binnig et al. [48] invented atomic force microscope (AFM). AFM uses a cantilever with a sharp tip mounted at its end to raster scan the sample. The imaging principle of AFM is shown in Fig. 1.3. The deflection of cantilever is detected by a four-quadrant position sensitivity detector (PSD) that senses a beam of laser reflected from the backside of the cantilever [49]. According to Hooke's law (F = kx, k is the spring constant of the AFM cantilever and x is the deflection of the cantilever), the interaction force between AFM tip and sample surface is acquired. The main AFM imaging modes are contact mode and tapping mode. During the contact mode scanning, according to the feedback control system, the piezoelectric ceramic driver controls the cantilever to move vertically to maintain a constant interaction force between AFM tip and sample surface by detecting the

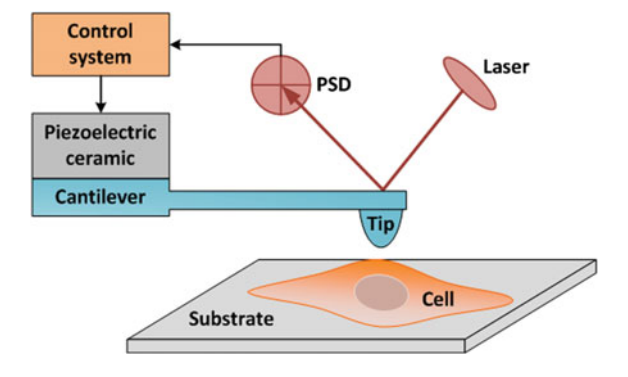


Fig. 1.3 The principle of AFM imaging

cantilever deflection. The forces involved in tip-sample interactions include van der Waals attractive force and electronic repulsive force. The contact mode scanning may cause damage to the sample due to the scratch. Tapping mode scanning eliminates the influence of lateral force on the sample by intermittently touching the sample. During tapping imaging, the amplitude of the vibrating cantilever is detected and the piezoelectric driver moves vertically to main a constant amplitude. The displacements of the AFM cantilever in vertical direction correspond to the topographical information of the sample surface. AFM not only has atomic spatial resolution [50], but also can work in liquids, allowing us to observe the fine structures of single living cells.

Single-molecule techniques mainly include single-molecule fluorescence method and single-molecule force measurement method [51]. Typical single-molecule fluorescence methods include total internal reflection fluorescence microscopy (TIRFM) [52, 53], fluorescence correlation spectroscopy (FCS) [54, 55], near-field scanning optical microscopy (NSOM) [56], fluorescence resonance energy transfer (FRET) [57, 58], and quantum dot (QD) [59]. TIRFM uses the evanescent field generated by total internal reflection to selectively illuminate the junction area between two types of optical medium with different refractive indexes (such as glass and water) and excite the fluorescent molecules within the thin layer of illumination area (the depth of the illumination area is in the range 50–150 nm [55]). TIRFM has high signal-to-noise ratio and thus is widely used for observing the dynamic behaviors of single molecules on cell surface [52, 53]. FCS measures the fluorescence intensity of the luminescent particles in the tiny area of the solution caused by random diffusion or chemical reactions, and then analyzes the changes of fluorescence intensity versus time to obtain the information of luminescent particles, such as concentration and chemical kinetics. FCS is particularly well suited for studying cell membrane events, as the cell membrane has lower spontaneous motion than do the cytoplasm and intracellular compartments, and diffusion of molecules within the cell membrane is slower [55]. NSOM is based on the scanning probe microscopy. NSOM uses a fiber probe to scan the surface of the sample and maintains the distance between probe and sample surface stable to yield the images that reflect the topography of the sample surface. The spatial resolution of NSOM image depends on the size of the probe aperture (often 50–100 nm [56]). When the target molecules on the cell surface are fluorescently labeled, the excitation light emitted from the NSOM fiber probe can be used to detect the behaviors of the target molecules. In FRET techniques, two different color dyes can be positioned at specific locations of the protein [58]. Upon radiation of light with the appropriate frequency, the donor absorbs the radiation and then transfers the energy to the acceptor. When the molecular conformation changes (that is the distance between the donor and the acceptor changes), the energy conversion efficiency between the donor and the acceptor changes, thereby the molecular conformation changes can be sensed by detecting the energy conversion efficiency. QDs are single crystals whose diameter is a few nanometers [59]. QDs are inorganic fluorescent dyes. Conventional organic and genetically encoded fluorophores have broad absorption/emission profiles and low photobleaching thresholds, and thus cannot long-term mark the molecules [60].

ODs have high fluorescence intensity, high resistance to photobleaching, broad excitation spectrum and narrow emission spectrum [61], which make it easy to identify and track single QDs. QDs are thus well suited for fluorescence imaging of single molecules. However, QDs cannot pass through the cell membrane. Labeling of intracellular targets requires delivery of the ODs into cells, either by carriers (e.g., lipids) or microjection [55], which is complex and can cause damage to cells. Single-molecule fluorescence techniques provide powerful tools for probing the real-time molecular activities of single cells, but there are still many issues needing to be addressed. The first issue is that current single-molecule fluorescence techniques are commonly focused on the proteins on the cell surface and are not yet applicable to intracellular proteins [61]. The second issue is that cell autofluorescence can disturb the labeled molecules [59]. In addition, commonly used fluorescent dyes have low fluorescence brightness and are prone to quench, which influence the interpretation of experimental results. Though ODs have many advantages compared with conventional fluorescent dyes, they are prone to be internalized on cell surface [62] and their toxicity [63] is often not trivial.

Single-molecule force measurement method directly measures forces generated during molecular activities. Forces are generally involved in life activities. Biomolecular interactions generate tiny forces ranging from piconewtons to nanonewtons [64]. These forces drive the progress of various physiological behaviors, e.g., the folding of the polypeptide into the functional state, stabilizing of protein structure, supramolecular assembly and ligand binding [65]. The advent of single-molecule force measurement techniques allows directly measuring the dynamics of single molecules, which facilitates us to better understand the underlying mechanisms guiding life activities. Typical single-molecule force measurement methods include optical tweezers, magnetic tweezers, biomembrane force probe (BFP), and AFM [66–68]. Light carries both linear and angular momentum and thus exerts force and torques on matter. Optical tweezers exploit this fundamental property to capture objects in a potential well formed by light [69, 70]. For measuring molecular behaviors by optical tweezers, one end of a protein is linked to a bead and the other end of the protein is linked to another bead. One bead is held in place at the end of a micropipette by suction, and the other bead is captured by the optical trap [71]. By moving the bead on the pipette relative to the bead in the optical trap, molecules are stretched and relaxed, generating force-extension curves. The sudden changes in the force-extension curves reflect the unfolding and refolding of the protein. For manipulating single molecules with magnetic tweezers, one end of the molecule is linked to the glass surface, and the other end is linked to a magnetic bead. A pair of small permanent magnets produces a magnetic field gradient along the axial direction, which results in a force on the bead directed up toward the magnets [66, 72, 73]. The force is controlled by moving magnets in the axial direction, which is used to manipulate the molecules. The disadvantage of optical tweezers is that the high intensity (typically $10^9 - 10^{12} \text{ W cm}^{-1}$) at the focus of the trapping laser results in local heating, which can influence enzymatic activity and change the local viscosity of the medium [66]. The disadvantage of magnetic tweezers is that it has limited spatial resolution (only 10 nm) and do not allow full three-dimensional manipulation [67]. BFP uses a micropipette-aspirated human ervthrocvte with a glass bead (probe bead) attached to its apex as a force transducer to measure molecular interactions [74]. The probe bead is coated by ligands. A target cell is fixed by another micropipette. The target cell is controlled to first contact the erythrocyte and then retract from the erythrocyte. If the receptors on the target cell bind to the ligands on the bead of the erythrocyte during the contact, then the retract process results in the deformation of the erythrocyte. Hence the receptor-ligand interactions are sensed by detecting the deformation of the erythrocyte. The disadvantage of BFP is that multiple receptor-ligand interactions can occur during the measurement and is relative complex (e.g., it requires preparing erythrocyte and calibrating the spring constant of the erythrocyte). For measuring molecular interactions by AFM, ligands are linked onto AFM tip which is then controlled to obtain force curves on substrate coated by receptors or directly on cell surface. The receptor-ligand interactions are observed by analyzing the force curves. Compared with optical tweezers, magnetic tweezers, and BFP, the unique advantage of AFM is that it can probe and manipulate the single native molecules on the surface of living cells [75, 76]. Besides, AFM can simultaneously acquire topography and molecular recognition on the cell surface [77], which facilitates us to comprehensively understand the behaviors of single molecules on cell surface. The contrast of the single-cell and single-molecule techniques described above is summarized in Table 1.1. Among these single-cell and single-molecule techniques, AFM occupies a unique position. AFM is a micro/nano multifunctional toolbox that can measure multiple physical parameters (e.g., cell morphology, cell mechanics, molecular force, molecular distribution on cell surface) of native biological

Table 1.1 Comparison of typical single-cell and single-molecule techniques for detecting the cellular biophysical properties

Techniques	Spatial resolution (nm)	Force resolution (pN)	Imaging cell topography	Measuring cell mechanics	Detecting molecular behaviors	Mapping molecules on cell surface
Optical microscope	100–200 [40]	N/A	Yes	No	No	No
Electron microscope	0.2–10 [75]	N/A	Yes	No	No	No
ESEM	~1 [47]	N/A	Yes	No	No	No
Single-molecule fluorescence	20–100 [55]	N/A	Yes	No	No	Yes
AFM	1-50 [75]	10–10 ⁴ [66]	Yes	Yes	Yes	Yes
Optical tweezers	0.1–2 [66]	0.1–100 [66]	No	Yes	Yes	No
Magnetic tweezers	5–10 [66]	10 ⁻³ -10 ² [66]	No	Yes	Yes	No
BFP	2–5 [68]	0.2–0.5 [68]	No	Yes	Yes	No

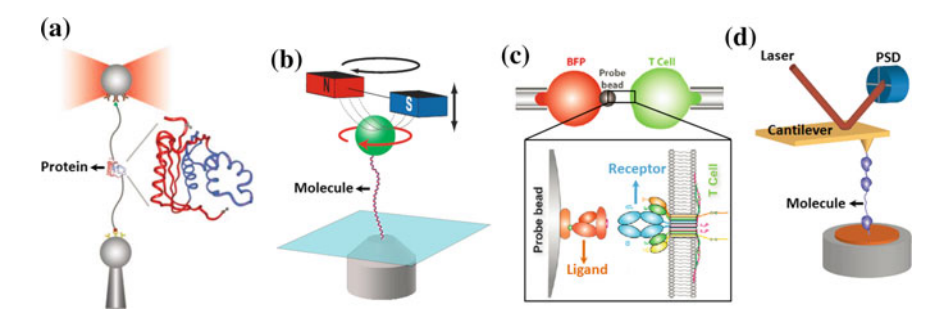


Fig. 1.4 Typical single-molecule force measurement techniques. **a** Optical tweezers. Reprinted with permission from [71]. Copyright 2005 AAAS. **b** Magnetic tweezers. Reprinted with permission from [66]. Copyright 2008 Nature Publishing Group. **c** BFP. Reprinted with permission from [74]. Copyright 2014 Elsevier Inc. **d** AFM. Reprinted with permission from [66]. Copyright 2008 Nature Publishing Group

samples, providing novel insights into cellular and molecular behaviors and promoting the development of nanobiotechnology [78] (Fig. 1.4).

1.4 Nanorobot Based on AFM

In 1959 Novel physicist Richard P. Feynman said in his prescient talk "There's plenty of room at the bottom" that we could arrange the atoms one by one the way we want them [79]. In order to achieve this goal, instruments that can manipulate single atoms are required. The technology envisioned in Feynman's talk is now called nanotechnology. Nanotechnology is the ability to control and restructure the matter at the atomic and molecular levels in the range of approximately 1–100 nm, and exploiting the distinct properties and phenomena at that scale as compared to those associated with single atoms or molecules or bulk behavior [80]. About 30 years after Feynman's talk, manipulating single atoms becomes true. In 1990, researchers from IBM company [81] successfully positioned individual xenon atoms on a single-crystal nickel surface with atomic precision using scanning tunneling microscope (STM) which was invented in 1981. STM uses a sharp tip to locate single atoms and carry them to new positions. The advent of STM and its derivative AFM provides the hand-eye system for manipulating nanoobjects, opening the door to the nanoworld [82]. At the nanoscale, the behaviors of matter dramatically change from our living world, which can be exploited for the benefit of mankind. Control of matter at the nanoscale has already played an important role in diverse scientific disciplines, including physics, chemistry, materials science, biology, medicine, engineering, and computer simulation [83]. USA established national nanotechnology initiative in 2000 and then many other countries (e.g., Japan, European Community) announced nanotechnology program [84], greatly promoting the development of nanotechnology. Now nanotechnology has been expected as the 'next big thing' with potential impact comparable to the steam, electricity or Internet revolutions [85], which is presenting new opportunities for upgrading traditional industries [86].

Nanotechnology allows us to conceive manufacturing tiny products with special functions based on precisely manipulating atoms and molecules. Such a tiny device is nanorobots. In the movie Fantastic Voyage (1966), a submarine and its crew were miniaturized and injected into the bloodstream of a wounded diplomat to save his life [87]. The tiny submarine described in Fantastic Voyage is the prototype of nanorobots [88]. Currently in the field of robotics, nanorobots are divided into two categories. The first type is the robots that are nanoscale in size [89]. However, the proposed nano-sized robots (e.g., artificial erythrocyte [90], medical nanorobotics for diabetes control [91]) are still in the conceptual stage. Currently, it is challenging to fabricate a nanorobot capable of performing even a simple medical task by traditional engineering method [92]. Biological nanomaterials have been exploited to construct complex "machinery" capable of actuation, propulsion, sensing, computation, and decision making [93]. In 2012, Douglas et al. [94] used DNA molecules to create a nanorobot (35 \times 35 \times 45 nm) which can deliver drugs to target cancerous cells and the results showed that nanorobots can induce a variety of tunable changes in cell behavior, practically opening the door to the applications of nanorobotic medicine, such as killing cancerous cell, cleaning clogged arteries, repairing tissues, and crushing stones that form inside organs [95]. The other type of nanorobot is a large robot that can be used to manipulate nanosized objects, often called a nanomanipulator [89]. The overall nanomanipulator system size can be very large, while only the manipulation tools, manipulated objects, and sensing, actuation, and manipulation precision are required to be at the nanoscale [96]. Nanomanipulator systems are constructed by using new material, fabrication, sensing, actuation, control, and assembly techniques due to the new situations (such as new physics, scaling effects, quantum effects and precision requirements) at the nanoscale [83]. So far typical nanomanipulators are based on scanning electron microscopy (SEM), ESEM or AFM [44, 97, 98]. The disadvantage of SEM-based nanomanipulator is that it requires the sample dried and fixed, meaning that it cannot handle living cells. Though ESEM can manipulate samples containing some moisture, currently living cells cannot be observed by ESEM under the physiological conditions [99]. In contrast, AFM can work in liquids, enabling robotic manipulations on single living cells under physiological conditions [87], such as drug injection [100], nanodissection [101], nanoindentation [102] and nanovisualization [103]. Hence, AFM-based nanomanipulator is particularly suited for biological applications at the nanometer scale. For simplicity, AFM-based nanorobot is used in the following to indicate AFM-based nanomanipulator.

Early AFM-based nanorobot lacks real-time feedback and is with low efficiency. We have developed AFM nanorobot system that has real-time haptic and visual feedback based on augmented reality [104–106], as shown in Fig. 1.5a). Using the augmented reality environment, the operator can sense the real-time contact force of the nano-objects being manipulated by the AFM tip (end effector) and also watch the real-time AFM images of the nanomanipulation [87]. The operator can determine the

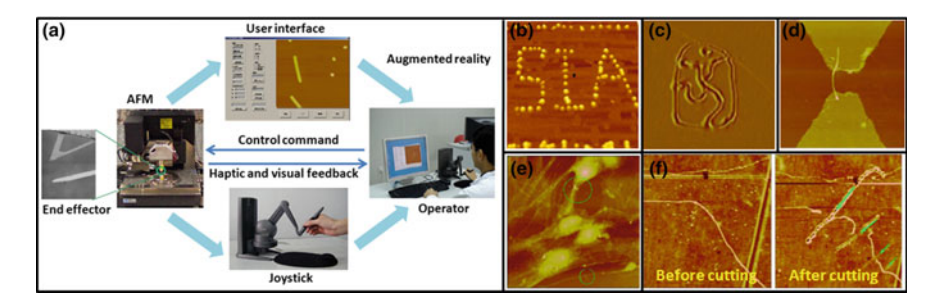


Fig. 1.5 AFM-based nanorobotic system and its applications. **a** System configuration [87]. **b** Pushing nanoparticles to form "SIA" pattern [107]. **c** Carving Olympic emblem [107]. **d** Pushing carbon nanotube onto the micro electrodes [107]. **e** Cutting surgery on single living neuron cell [108]. Circles indicate the cutting positions. **f** Cutting DNAs [108]. Arrows indicate cutting directions

next manipulation strategy based on the haptic and visual feedback results. The advantage of human-in-the-loop (closed-loop) nanorobot system is that we can perform serial manipulations without AFM imaging, thus greatly improving the efficiency of nanomanipulation. Since AFM only has one tip as an end effector and, therefore, can only apply a point force to the nano-object, it is difficult to achieve stable manipulation, especially when working with rod-shaped objects. Recently, we have developed a nanohand-manipulation strategy (using a single tip to mimic the manipulation effect that a multi-AFM tip can achieve through planned high-speed sequential tip pushing) to stably transfer nano-objects [106]. Experiments using zinc oxide (ZnO) nanorods demonstrated the efficiency and reliability of the nano-hand-manipulation method. The AFM-based nanorobot can perform various manipulations, for example, pushing nanoparticles to form special patterns (Fig. 1.5b), carving pattern on substrate (Fig. 1.5c), pulling carbon nanotube to form microelectric chip (Fig. 1.5d) [107], cutting single living cells (Fig. 1.5e) and single DNAs (Fig. 1.5f) [108].

1.5 Opportunities and Challenges

In 2009, Susan Hockfield, the president of the Massachusetts Institute of Technology, said in the AAAS Forum that the third revolution in life sciences, the convergence of life sciences, physical sciences, and engineering, is taking place [109]. In the past decades, new scientific techniques and instruments (e.g., electron microscope, X-ray computed tomography, nuclear magnetic resonance imaging, positron emission tomography) developed by physicist and engineers have been widely utilized both in revealing molecular behaviors and biomedical applications. In recent years, new single-molecule techniques are continually emerged, which greatly promote the progress of life sciences. Many systems which are inaccessible by traditional ensemble experiments (e.g., molecular transcription in single cells

[110], conformational changes of single native proteins [111], rotary dynamics of single rotor protein [112], and walking of single myosin molecule along the actin [113]) are now acquiring significant achievements due to the applications of single-molecule techniques. The deep penetration and convergence of life sciences, physical sciences, and engineering has become an important trend in the development of science and technology. This convergence will not only affect life sciences, but will also revolutionize science and technology, and thus affect human life.

AFM-based nanorobotics is a new emerging area in the field of robotics and automation. It has unique advantages such as accessing to small areas, increased flexibility, functionality and robustness, and being low cost [114]. The third revolution of life sciences presents biomedical nanorobotics with unprecedented opportunities. It combines the established theory and techniques of robotics with nanoscale technology to significantly improve the quality of our lives [115]. However, applying robotics to investigate cell behaviors at the micro/nano scale is quite different from the robotics at the macro scale [1]. In the pipeline of automotive industry, the automotive parts are designed manually and have the same sizes, which facilitate the industrial robots to perform repetitive tasks. While cells are highly heterogeneous and different cells have different properties (e.g., shape, density, size, stiffness, deformability), meaning that the objects being manipulated by micro/nano robots are very unstructured. Besides, cells are dynamic (various metabolic activities take place within cells during the life of cells), which results in the temporal heterogeneity. Investigating cellular variability has recently been considered to be a new era in molecular biology, which can reveal novel regulatory mechanisms for cellular processes [25]. The daunting challenge in life sciences is to determine which components of the observed cellular heterogeneity serve a biological function or contain meaningful information [20]. Consequently, cellular variability presents difficulties when applying micro/nano automation technology to detect the behaviors of cells.

In order to develop a micro/nano automation system for detecting cancerous cells prepared from individual patients, there are many technical challenges needing to be addressed, mainly including automated cell isolation and delivery, automatically acquiring the physiological features of cells, and data analysis [1], as shown in Fig. 1.6. After preparing the clinical biological samples (e.g., biopsy tissues acquired by surgery, bone marrow acquired by aspiration, and peripheral blood extracted from vessels) from clinical patients, cancerous cell isolation methods are applied to collect cancerous cells which are then delivered to the micro/nano automation pipeline. Micro/nano robots automatically perform sequential manipulations on the cells in the pipeline. Like industrial robots in the automation pipeline of automotive industry, each micro/nano robot performs a specific task, e.g., delivering or injecting drugs onto/into the cell, indenting the cell, visualizing the cellular structures, and probing the target molecules on cell surface. After the robotic manipulations, the detection results of each cell in the pipeline are recorded. By modeling the process of robotic detection and analyzing the detection data, quantitative cellular features (e.g., surface roughness, surface topography, mechanical properties, and target molecules' properties) are obtained. By inputting

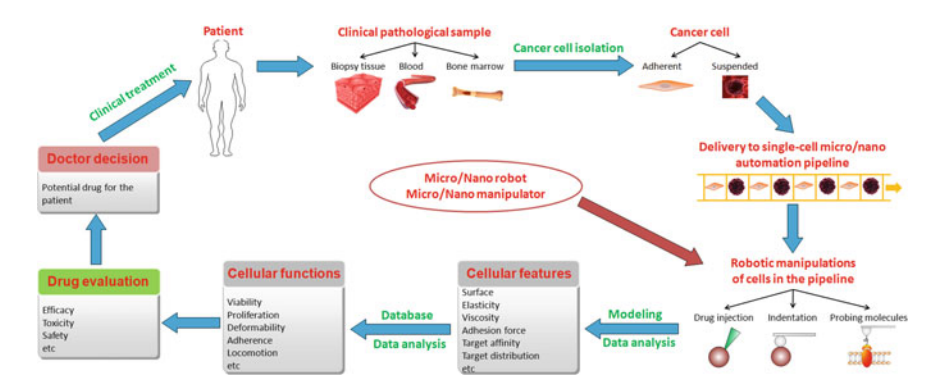


Fig. 1.6 Flowchart of automated drug susceptibility test in personalized cancer treatment based on label-free micro/nano robotics [1]

these quantitative parameters into the database and according to the relation models, the changes of cellular biological functions (e.g., viability, proliferation, the ability of deformation, adherence and locomotion [34]) are acquired, which are then used for drug evaluation and doctor decision making (e.g., recognizing the potential sensitive drugs for the patient). After decision making, the potential sensitive drugs are used for the clinical therapy of the patient.

1.6 Thesis Contents and Chapter Organization

In this thesis, by combining engineering with medicine, AFM-based nanorobot was used to investigate the clinical rituximab actions from three aspects (imaging cell topography, measuring cell mechanics, and recognizing molecular interactions) to address the problem of variable therapeutic outcomes between different patients in the lymphoma rituximab targeted therapy and expand the biomedical applications of nanorobotics. This thesis focuses on the investigations of the following four issues (as shown in Fig. 1.7). The first issue is the cell immobilization method in liquids for AFM observation. The ideal condition for AFM detection is that the position of the sample relative to the AFM tip is constant. However, the membranes of mammalian cells are very soft and dynamic [99], which makes it difficult to observe the living cells with molecular resolution. Hence appropriate methods are required to decrease the influence of cell membrane movement on AFM detection. The second issue is the dynamic changes of cell mechanics in the development and clinical therapy of lymphoma. Recent studies have shown that cell mechanics is a novel biomarker for indicating cell states [34–36], but so far the role of cell mechanics in lymphoma rituximab therapy is unknown. Hence utilizing AFM-based nanorobot to detect cell mechanics in lymphoma rituximab therapy may provide novel insights into lymphoma and rituximab actions. The third issue is quantitatively probing the behaviors of target molecules on cell surface. As shown

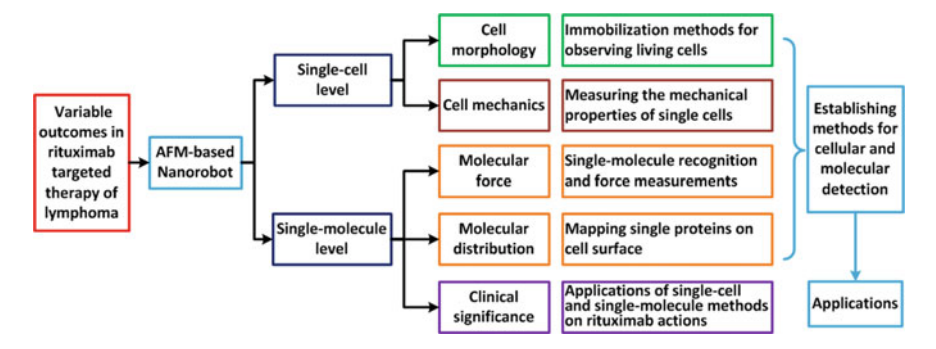


Fig. 1.7 Research frame of the thesis

in Fig. 1.1, various molecular interactions take place during the actions of rituximab. In order to better understand the efficacies of rituximab, probing the target molecules on the cell surface is indispensable. Finally is the applications on clinical biopsy samples. Cell lines grown in vitro are quite different from the cells in the human body. In order to examine the translational significance of AFM-based nanorobotics, primary cancerous cells from clinical lymphoma patients need to be prepared and tested.

The chapter organizations are following:

Chapter 2 presents studies on developing immobilization methods for observing living mammalian suspended cells by AFM nanorobotics. A review of the current status of living cell imaging by AFM was presented firstly, along with the establishment of single-cell experimental platform based on AFM and its applications on imaging adherent cells. Next, according to the characteristics of mammalian suspended cells, immobilization methods based on micro-pillar/micro-well mechanical trapping and poly-L-lysine electrostatic adsorption were developed to visualize the fine structures of single living lymphoma cells.

Chapter 3 presents studies on measuring the mechanical properties of single cells by AFM nanorobotics. First, the motivation of single-cell mechanical assay was presented, along with a review of the current status of measuring cell mechanics by AFM. Then the principle of measuring cell mechanics by AFM was detailed. Next, single micro-spheres were attached onto the AFM cantilever via AFM micro-manipulation and the fabricated sphere probes were used to measure the Young's modulus of different types of cancerous cells with variable aggressive capabilities.

Chapter 4 presents studies on single-molecule recognition and force measurements by AFM nanorobotics. First, the motivation of AFM in investigating membrane proteins was presented, along with a review of the current status of measuring molecular interactions by AFM. Then the principle and method of measuring the binding force of single molecular pair was detailed. Next, AFM tip functionalization and verification were presented. The functionalized tips were then used to measure the molecular interactions between rituximab and CD20.

Chapter 5 presents studies on mapping single proteins on cell surface by AFM nanorobotics. The current status of observing the distributions of target molecules on cell surface was firstly reviewed. Next, the introduction of peak force tapping (PFT) mode was presented. With the use of functionalized tips, purified proteins on mica and native proteins on lymphoma cell surface were recognized at PFT mode. Quantitative cluster information of target molecules was calculated from the recognition images.

Chapter 6 presents studies on the applications of the established AFM single-cell and single-molecule methods in lymphoma rituximab therapy. First, the dynamic changes of cellular morphology and cellular mechanics in the three killing mechanisms (PCD, ADCC, CDC) of rituximab were investigated. Then the binding affinities and distributions of two target molecules (CD20 on lymphoma cell and Fc receptor on effector) were detected on primary cancerous cells and effector cells prepared from the bone marrow of clinical lymphoma patients based on the fluorescence recognition of specific cell surface markers. Next, the relationships between AFM-obtained results and clinical rituximab efficacies were analyzed.

Chapter 7 is the conclusion and future work of the thesis.

References

- Li M, Liu L, Xi N et al (2017) Applications of micro/nano automation technology in detecting cancer cells for personalized medicine. IEEE Trans Nanotechnol 16:217–229
- Torre LA, Bray F, Siegel RL et al (2015) Global cancer statistics, 2012. CA Cancer J Clin 65:87–108
- 3. Bray F, Jemal A, Grey N et al (2012) Global cancer transitions according to human development index(2008–2030): a population-based study. Lancet Oncol 13:790–801
- Schrama D, Reisfeld RA, Becker JC (2006) Antibody targeted drugs as cancer therapeutics. Nat Rev Drug Discov 5:147–159
- DeVita VT, Rosenberg SA (2012) Two hundred years of cancer research. N Engl J Med 366:2207–2214
- Schiffman M, Castle PE, Jeronimo J et al (2007) Human papillomavirus and cervical cancer. Lancet 370:890–907
- 7. Varmus H (2006) The new era in cancer research. Science 312:1162-1165
- 8. Chen W, Zheng R, Baade PD et al (2016) Cancer statistics in China, 2015. CA Cancer J Clin 66:115–132
- Siegel R, Naishadham D, Jemal A (2013) Cancer statistics, 2013. CA Cancer J Clin 63: 11–30
- Cheson BD, Leonard JP (2008) Monoclonal antibody therapy for B-cell non-Hodgkin,s lymphoma. N Engl J Med 359:613

 –626
- 11. Cartron G, Watier H, Golay J et al (2004) From the bench to the bedside: ways to improve rituximab efficacy. Blood 104:2635–2642
- 12. Li M, Liu L, Xi N et al (2016) Applications of atomic force microscopy in exploring drug actions in lymphoma-targeted therapy at the nanoscale. Bionanoscience 6:22–32
- Glennie MJ, French RR, Cragg MS et al (2007) Mechanisms of killing by anti-CD20 monoclonal antibodies. Mol Immunol 44:3823–3837
- 14. Lim SH, Beers SA, French RR et al (2010) Anti-CD20 monoclonal antibodies: historical and future perspectives. Haematologica 95:135–143

References 17

 Maloney DG (2012) Anti-CD20 antibody therapy for B-cell lymphomas. N Engl J Med 366:2008–2016

- Alduaij W, Illidge TM (2011) The future of anti-CD20 monoclonal antibodies: are we making progress. Blood 117:2993–3001
- Rezvani AR, Maloney DG (2011) Rituximab resistance. Best Pract Res Clin Haematol 24:203–216
- Oflazoglu E, Audoly LP (2010) Evolution of anti-CD20 monoclonal antibody therapeutics in oncology. mAbs 2: 14–19
- 19. Xie XS, Yu J, Wang WY (2006) Living cells as test tubes. Science 312:228-230
- Altschuler SJ, Wu LF (2010) Cellular heterogeneity: do differences make a difference. Cell 141:559–563
- Junttila MR, de Sauvage FJ (2013) Influence of tumour micro-environment heterogeneity on therapeutic response. Nature 501:346–354
- 22. Burrell RA, McGranahan N, Bartek J et al (2013) The causes and consequences of genetic heterogeneity in cancer evolution. Nature 501:338–345
- Bedard PL, Hansen AR, Ratain MJ et al (2013) Tumour heterogeneity in the clinic. Nature 501:355–364
- Humburg MA, Collins FS (2010) The path to personalized medicine. N Engl J Med 363:301–304
- Pelkmans L (2012) Using cell-to-cell variability—a new era in molecular biology. Science 336:425–426
- 26. Wilson EB (1925) The cell in development and heredity. Macmillan, New York
- 27. Mogilner A, Keren K (2009) The shape of motile cells. Curr Biol 19:R762–R771
- 28. https://www.britannica.com/science/sickle-cell-anemia
- Chow KH, Factor RE, Ullman KS (2012) The nuclear envelope environment and its cancer connections. Nat Rev Cancer 12:196–209
- 30. Lyer S, Gaikwad RM, Subba-Rao V et al (2009) Atomic force microscopy detects differences in the surface brush of normal and cancerous cells. Nat Nanotechnol 4:389–393
- 31. Fletcher DA, Mullins RD (2010) Cell mechanics and the cytoskeleton. Nature 463:485–492
- 32. Janmey PA, McCulloch CA (2007) Cell mechanics: integrating cell responses to mechanical stimuli. Annu Rev Biomed Eng 9:1–34
- 33. Li QS, Lee GYH, Ong CN et al (2008) AFM indentation study of breast cancer cells. Biochem Biophys Res Commun 374:609–613
- 34. Suresh S (2007) Biomechanics and biophysics of cancer cells. Acta Biomater 3:413-438
- Cross SE, Jin YS, Rao JY et al (2007) Nanomechanical analysis of cells from cancer patients. Nat Nanotechnol 2:780–783
- 36. Plodinec M, Loparic M, Monnier C et al (2012) The nanomechanical signature of breast cancer. Nat Nanotechnol 7:757–765
- 37. Reichert JM (2010) Antibodies to watch in 2010. mAbs 2: 84-100
- 38. Reichert JM (2013) Antibodies to watch in 2013. mAbs 5: 513–517
- 39. Mow VC, Guilak F, Tran-Son-Tay R et al (1994) Cell mechanics and cellular engineering. Springer, New York
- 40. Puttern EGV, Akbulut D, Bertolotti J et al (2011) Scattering lens resolves sub-100 nm structures with visible light. Phys Rev Lett 106:193905
- 41. Oesterhelt F, Oesterhelt D, Pfeiffer M et al (2000) Unfolding pathways of individual bacteriorhodopsins. Science 288:143–146
- 42. Mulvey T (1989) The electron microscope: the British contribution. J Microsc 155:327–338
- 43. Smith DJ (2008) Ultimate resolution in the electron microscope. Mater Today 11:30–38
- 44. Ahmad MR, Nakajima M, Kojima S et al (2010) Nanoindentation methods to measure viscoelastic properties of single cells using sharp, flat, and buckling tips inside ESEM. IEEE Trans Nanobiosci 9:12–23
- 45. Kirk SE, Skepper JN, Donald AM (2009) Application of environmental scanning electron microscopy to determine biological surface structure. J Microsc 233:205–224

- 46. Muscariello L, Rosso F, Marino G et al (2005) A critical overview of ESEM applications in the biological field. J Cell Physiol 205:328–334
- 47. Toth M, Lobo CJ, Ralph W et al (2007) Nanostructure fabrication by ultra-high-resolution environmental scanning electron microscopy. Nano Lett 7:525–530
- 48. Binnig G, Quate CF, Gerber C (1986) Atomic force microscope. Phys Rev Lett 56:930-933
- 49. Li M, Dang D, Liu L et al (2017) Imaging and force recognition of single molecular behaviors using atomic force microscopy. Sensors 17:200
- 50. Gross L, Mohn F, Moll N et al (2009) The chemical structure of a molecule resolved by atomic force microscopy. Science 325:1110–1114
- 51. Dupres V, Alsteens D, Andre G et al (2009) Fishing single molecules on live cells. Nano Today 4:262–268
- Axelrod D (2001) Total internal reflection fluorescence microscopy in cell biology. Traffic 2:764–774
- 53. Mashanov GI, Tacon D, Knight AE et al (2003) Visualizing single molecules inside living cells using total internal reflection fluorescence microscopy. Methods 29:142–152
- 54. Ries J, Schwille P (2012) Fluorescence correlation spectroscopy. BioEssays 34:361-368
- Jaiswal JK, Simon SM (2007) Imaging single events at the cell membrane. Nat Chem Biol 3:92–98
- Zanten TSV, Lopez-Bosque MJ, Garcia-Parajo MF (2010) Imaging individual proteins and nanodomains on intact cell membranes with a probe-based optical antenna. Small 6:270–275
- 57. Jares-Erijman EA, Jovin TM (2003) FRET imaging. Nat Biotechnol 21:1387-1395
- Ritort F (2006) Single-molecule experiments in biological physics: methods and applications. J Phys: Condens Matter 18:R531–R583
- Michalet X, Pinard FF, Bentolila LA (2005) Quantum dots for live cells, in vivo imaging and diagnostics. Science 307:538–544
- Medintz IL, Uyeda HT, Goldman ER et al (2005) Quantum dot bioconjugates for imaging, labeling and sensing. Nat Mater 4:435

 –446
- 61. Jain A, Liu R, Ramani B et al (2011) Probing cellular protein complexes using single-molecule pull-down. Nature 473:484–488
- 62. Lagerholm BC, Wang M, Ernst LA et al (2004) Multicolor coding of cells with cationic peptide coated quantum dots. Nano Lett 4:2019–2022
- 63. Bottrill M, Green M (2011) Some aspects of quantum dot toxicity. Chem Commun 47: 7039–7050
- 64. Stewart MP, Toyoda Y, Hyman AA et al (2011) Force probing cell shape changes to molecular resolution. Trends Biochem Sci 36:444–450
- Kedrov A, Janovjak H, Sapra KT et al (2007) Deciphering molecular interactions of native membrane proteins by single-molecule force spectroscopy. Ann Rev Biophys Biomol Struct 36:233–260
- 66. Neuman KC, Nagy A (2008) Single-molecule force spectroscopy: optical tweezers, magnetic tweezers and atomic force microscopy. Nat Methods 5:491–505
- 67. Walter NG, Huang CY, Manzo AJ et al (2008) Do-it-yourself guide: how to use the modern single-molecule toolkit. Nat Methods 5:475–489
- 68. Merkel R, Nassoy P, Leung A et al (1999) Energy landscapes of receptor-ligand bonds explored with dynamic force spectroscopy. Nature 397:50–53
- 69. Moffitt JR, Chemla YR, Smith SB et al (2008) Recent advances in optical tweezers. Annu Rev Biochem 77:205–228
- Jing P, Wu J, Liu GW et al (2016) Photonic crystal optical tweezers with high efficiency for live biological samples and viability characterization. Sci Rep 6:19924
- 71. Cecconi C, Shank EA, Bustamante C et al (2005) Direct observation of the three-state folding of a single protein molecule. Science 309:2057–2060
- 72. Strick TR, Croquette V, Bensimon D (2000) Single-molecule analysis of DNA uncoiling by a type II topoisomerase. Nature 404:901–904
- 73. Le S, Liu R, Lim CT et al (2016) Uncovering mechanosensing mechanisms at the single protein level using magnetic tweezers. Methods 94:13–18

References 19

74. Liu B, Chen W, Evavold BD et al (2014) Accumulation of dynamic catch bonds between TCR and agonist peptide-MHC triggers T cell signaling. Cell 157:357–368

- Dufrene YF, Ando T, Garcia R et al (2017) Imaging modes of atomic force microscopy for application in molecular and cell biology. Nat Nanotechnol 12:295–307
- 76. Hinterdorfer P, Dufrene YF (2006) Detection and localization of single molecular recognition events using atomic force microscopy. Nat Methods 3:347–355
- 77. Senapati S, Lindsay S (2016) Recent progress in molecular recognition imaging using atomic force microscopy. Acc Chem Res 49:503–510
- 78. Muller DJ, Dufrene YF (2008) Atomic force microscopy as a multifunctional molecular toolbox in nanobiotechnology. Nat Nanotechnol 3:261–269
- 79. Feynman RP (1960) There's plenty of room at the bottom. Caltech's Eng Sci 23:22–36
- Roco MC (2011) The long view of nanotechnology development: the national nanotechnology initiative at 10 years. J Nanopart Res 13:427–445
- 81. Eigler DM, Schweizer EK (1990) Positioning single atoms with a scanning tunneling microscope. Nature 344:524–526
- 82. Gerber C, Lang HP (2006) How the doors to the nanoworld were opened. Nat Nanotechnol 1:3–5
- 83. Fukuda T, Arai F, Nakajima M (2013) Micro-nanorobotic manipulation systems and their applications. Springer, New York
- 84. Roco MC (2005) Environmentally responsible of nanotechnology. Environ Sci Technol 39:106–112
- Grzybowski BA, Huck WTS (2016) The nanotechnology of life-inspired systems. Nat Nanotechnol 11:585–592
- 86. Bai C (2005) Ascent of nanoscience in China. Science 309:61-63
- 87. Li M, Liu L, Xi N et al (2015) Biological applications of a nanomanipulator based on AFM: in situ visualization and quantification of cellular behaviors at the single-molecule level. IEEE Nanotechnol Mag 9:25–35
- 88. Abbott JJ, Nagy Z, Beyeler F et al (2007) Robotics in the small part I: microrobotics. IEEE Robot Autom Mag 14:92–103
- Dong LX, Nelson BJ (2007) Robotics in the small part II: nanorobotics. IEEE Robot Autom Mag 14:111–121
- 90. Freitas RA (2005) What is nanomedicine. Nanomedicine 1:2-9
- Cavalcanti A, Shirinzadeh B, Kretly LC (2008) Medical nanorobotics for diabetes control. Nanomedicine 4:127–138
- Nelson BJ, Kaliakatsos IK, Abbott JJ (2010) Microrobots for minimally invasive medicine. Ann Rev Biomed Eng 12:55–85
- 93. Lenaghan SC, Wang Y, Xi N et al (2013) Grand challenges in bioengineered nanorobotics for cancer therapy. IEEE Trans Biomed Eng 60:667–673
- Douglas SM, Bachelet I, Church GM (2012) A logic-gated nanorobot for targeted transport of molecular payloads. Science 335:831–834
- Wang J, Gao W (2012) Nano/microscale motors: biomedical opportunities and challenges.
 ACS Nano 6:5745–5751
- 96. Sitti M (2007) Microscale and nanoscale robotics systems. IEEE Robot Autom Mag 14: 53-60
- 97. Onal CD, Sitti M (2010) Teleoperated 3-D force feedback from the nanoscale with an atomic force microscope. IEEE Trans Nanotechnol 9:46–54
- 98. Xie H, Regnier S (2012) High-efficiency automated nanomanipulation with parallel imaging/manipulation force microscopy. IEEE Trans Nanotechnol 11:21–33
- 99. Li M, Liu L, Xi N et al (2013) Progress of AFM single-cell and single-molecule morphology imaging. Chin Sci Bull 58:3177–3182
- Guillaume-Gentil O, Potthoff E, Ossola D et al (2014) Force-controlled manipulation of single cells: from AFM to fluidFM. Trends Biotechnol 32:381–388
- 101. Yang R, Song B, Sun Z et al (2015) Cellular level robotic surgery: nanodissection of intermediate filaments in live keratinocytes. Nanomedicine 11:137–145

- 102. Li M, Liu L, Xi N et al (2014) Nanoscale imaging and morphological analysis of Fc receptor-mediated macrophage phagocytosis against cancer cells. Langmuir 30:1609–1621
- 103. Li M, Xiao X, Liu L et al (2016) Nanoscale quantifying the effects of targeted drug on chemotherapy in lymphoma treatment using atomic force microscopy. IEEE Trans Biomed Eng 63:2187–2199
- Li G, Xi N, Yu M et al (2004) Development of augmented reality system for AFM-based nanomanipulation. IEEE-ASME Trans Mechatron 9:358–365
- Liu L, Luo Y, Xi N et al (2008) Sensor referenced real-time videolization of atomic force microscopy for nanomanipulations. IEEE-ASME Trans Mechatron 13:76–85
- Hou J, Liu L, Wang Z et al (2013) AFM-based robotic nano-hand for stable manipulation at nanoscale. IEEE Trans Autom Sci Eng 10:285–295
- 107. Liu L (2009) Study on task space oriented real-time feedback in robotic nanomanipulation. Ph.D. thesis of University of Chinese Academy of Sciences
- Li G, Xi N, Wang DH (2005) In situ sensing and manipulation of molecules in biological samples using a nanorobotic system. Nanomedicine 1:31–40
- 109. Hockfield S (2009) The next innovation revolution. Science 323:1147
- 110. Taniguchi Y, Choi PJ, Li GW et al (2010) Quantifying *E.coli* proteome and transcriptome with single-molecule sensitivity in single cells. Science 329:533–538
- 111. Mari SA, Pessoa J, Altieri S et al (2011) Gating of the mlotik1 potassium channel involves large rearrangements of the cyclic nucleotide-binding domains. Proc Natl Acad Sci USA 108:20802–20807
- 112. Uchihashi T, Iino R, Ando T et al (2011) High-speed atomic force microscopy reveals rotary catalysis of rotorless F₁-ATPase. Science 333:755–758
- 113. Kodera N, Yamamoto D, Ishikawa R et al (2010) Video imaging of walking myosin V by high-speed atomic force microscopy. Nature 468:72–76
- Sitti M (2004) Micro- and nano-scale robotics. In: Proceeding of the 2004 American Control Conference, Boston, 2004
- 115. Hill C, Amodeo A, Joseph JV et al (2008) Nano- and microrobotics: how far is the reality. Expert Rev Anticancer Ther 8:1891–1897

Chapter 2 Immobilization Methods for Observing Living Mammalian Suspended Cells by AFM

Imaging cellular topography is the basic application of AFM in cell biology. The studies about AFM cell imaging began in the early 1990s [1]. According to the different imaging environments, AFM cell imaging can be divided into two types, including imaging cells in air and imaging cells in liquid. For imaging cells in air, cells are chemically fixed to maximally maintain the native structures of the cells. The most commonly used chemical fixatives are 2.5% glutaraldehyde and 4% paraformaldehyde [2]. In 2005, Yang et al. [3] used AFM to image the interactions between nanoparticles and cells in air based on glutaraldehyde fixation and AFM images clearly showed the endocytosis of nanoparticles taking place during the process of internalization. In 2009, Wu et al. [4] investigated the membrane surface nanostructures of T lymphocytes by AFM imaging in air based on glutaraldehyde fixation, revealing that there were significant differences in the nanoscale cellular topography between resting T lymphocytes and activated T lymphocytes. The process of imaging chemically fixed cells in air is simple and the recorded AFM images are often with high spatial resolution, which is useful for visualizing the detailed structures of cell surface. However, the drying process can inevitably cause the changes of cellular structures, which produces difficulty in the interpretation of the obtained AFM images. Besides, in many cases, researchers are more interested in living cells, since the results from living cells can better reflect the real situations and allow investigating the real-time dynamics of cellular fine structures during physiological activities.

2.1 Current Status of Immobilizing Living Cell for AFM Imaging

The prerequisite of imaging living cells by AFM is immobilizing living cells firmly on a substrate to resist the lateral forces exerted by the scanning tip [5]. For the different cell types, the immobilization methods are varied. Adherent cells (e.g.,

fibroblasts, epithelial cells, and neurons) can directly grow on the substrate (e.g., petri dish, glass slide), and thus they can be imaged by AFM after being cultured for 1 or 2 days on the substrate [6]. Sometimes the substrate is coated by a layer of poly-L-lysine to promote cell adhesion [7]. For microbial cells (e.g., bacterium, yeast), they cannot naturally adhere to the substrate. Electrostatic adsorption method and porous polymer membrane method are commonly used to immobilize microbial cells [8]. In electrostatic adsorption, positively charged macromolecules such as poly-L-lysine are coated on the substrate so that the negatively charged microbial cells readily adsorb. Alternatively, cell suspensions are filtered through a porous polymer membrane by an injector, which can trap microbial cells in the pores of the polymer membrane. The polymer membrane is then attached to a substrate with double-sided adhesion tape. It should be noted that the porous polymer membrane immobilization method is based on commercial membranes and is thus best suited for round-shaped microbial cells whose sizes are comparable to the pore size. It is not well suited for rod-shaped cells [9]. In 2010, Fantner et al. [10] used high-speed AFM to image the morphological dynamics of Escherichia coli cells based on the poly-L-lysine method, clearly revealing the rougher of the cell surface after the stimulation of antimicrobial peptide. In 2010, Andre et al. [11] used the porous polymer membrane to immobilize the living Lactococcus lactis cells and observed the nanoscale organization of the peptidoglycan in the cell by AFM imaging.

The electrostatic adsorption and porous polymer membrane methods are not applicable for mammalian suspended cells (e.g., blood cells) which are much larger than microbial cells and have soft surface (microbial cells have stiff cell walls). There are no commercially available polymer membranes whose pores are comparable to the size of mammalian suspended cells. Researchers have used microwells fabricated in the silicon substrate to trap mammalian suspended cells (e.g., leukamia cells [12], chondrocytes [13]) for measuring cell mechanics. Although the microwells can help cells to withstand the lateral forces exerted by scanning tip, in the vertical direction there are no forces to attach the cells to the bottom of the well, causing that cells in the wells can easily be moved when being probed by AFM tip. Currently, the spatial resolution for AFM imaging of mamalian cells is only about 50 nm [14]; this is because the cell membranes are soft and dynamic in nature, which in turn causes the scanning tip to deform the cell membrane. Besides, there are adhesive interactions between the AFM tip and cell membrane [15]. All of these factors seriously influence the resolution of AFM imaging of mammalian cells and so far it has not been able to resolve single proteins on living cells.

2.2 Biological Experiment Platform Based on AFM Nanorobot

The biological experiment platform based on AFM nanorobot developed here includes AFM (Bruker, Santa Barbara, USA), cell incubator (Thermo Fisher, Waltham, USA), biological safety cabinet (Thermo Fisher, Waltham, USA), optical

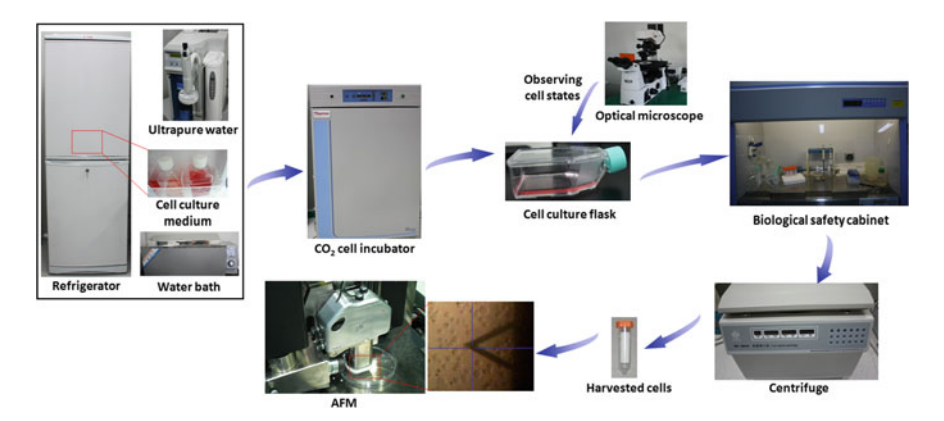


Fig. 2.1 AFM nanorobot biological experiment platform. Cells cultured in the CO₂ incubator are transported to the biological safety cabinet for sample preparation, and the samples are then transported to AFM for experiments, such as imaging cellular topography, measuring cellular mechanics, and recognizing molecular interactions on cell surface

microscope (Nikon, Tokyo, Japan), centrifuge (Zonkia, Hefei, China), refrigerator (Zhongke Meiling, Hefei, China), ultrapure water system (Millipore, Billerica, USA), and water bath, as shown in Fig. 2.1. Cell incubator provides the environment (37 °C, 5% CO₂) for cellular survival and proliferation in vitro. Cell culture mediums provide necessary nutrients that promote cell growth. Ultrapure water provides sterile deionized water for cell assay. The cell culture medium is stored in the refrigerator at 4 °C. The cell culture medium is heated to 37 °C in the water bath before being used. Optical microscope is used to observe the growth state of cells to judge whether or not cell passage is needed. The biological safety cabinet is used for related manipulations in the experiments, such as preparing cell culture medium, drug stimulation, and fluorescence staining. Centrifuge is used to harvest cells, which are then delivered to the workspace of AFM for various experiments.

With the established biological experiment platform, three types of adherent cells (MCF-7 human breast cancer cell line, HeLa human cervical cancer cell line, U251 human glioblastoma cell line) were imaged, as shown in Fig. 2.2. Under the guidance of optical microscope (Fig. 2.2a–c), the AFM probe was moved to the living cells to perform contact mode imaging. The three types of cells (MCF-7, HeLa, U251) firmly adhere to the substrate, which allows them easily imaged by AFM. Figure 2.2d, g are the AFM height image and corresponding deflection image of MCF-7 cells respectively. The scan size was 100 μ m. We can see that four MCF-7 cells clustered together. MCF-7 cells were triangular or polygonal, and cellular edges were obviously discernible. Figure 2.2e, h are the AFM height image and corresponding deflection image of HeLa cells respectively. The scan size was 80 μ m. Nine HeLa cells which adhered to the substrate were visible. Figure 2.2f, i are the AFM height image and corresponding deflection image of U251 cells respectively. The scan size was 120 μ m. Comparing the three types of cells, we can

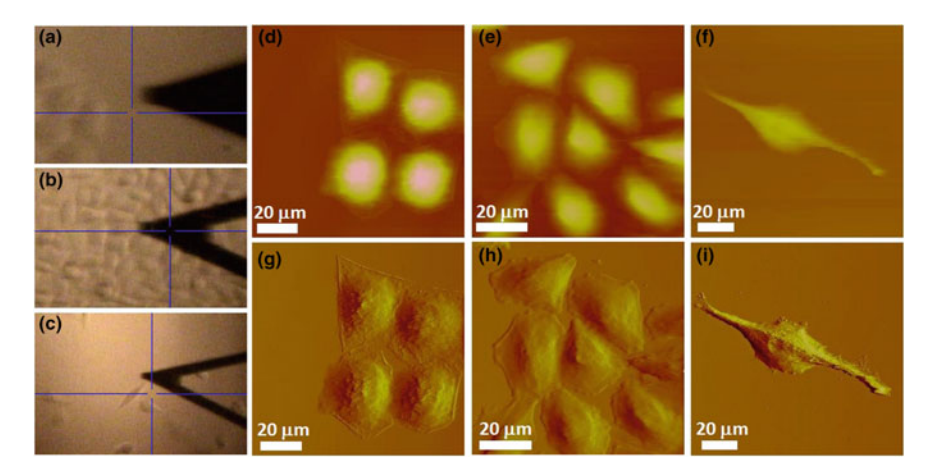


Fig. 2.2 AFM contact mode images of living adherent cells. (\mathbf{a} - \mathbf{c}) Under the guidance of optical image, the AFM tip was moved to the cells. (\mathbf{d} - \mathbf{f}) AFM height images of MCF-7 cells \mathbf{d} , HeLa cells \mathbf{e} , and U251 cells \mathbf{f} . (\mathbf{g} - \mathbf{i}) Corresponding AFM deflection images of MCF-7 cells \mathbf{g} , HeLa cells \mathbf{h} , and U251 cells \mathbf{i}

see that MCF-7 and HeLa cells had polygonal shape, while U251 cells were fusiform. This morphology structure caused that the diameter of U251 cells along the long axis was significantly larger than the size of MCF-7 and HeLa cells. Collectively, adherent cells can naturally grow and spread on the substrate, and thus facilitates AFM imaging on them.

2.3 Immobilizing Mammalian Suspended Cells by Micropillar Array

In order to image mammalian suspended cells, here an immobilization method combining micropillar mechanical trapping in the horizontal direction and poly-L-lysine electrostatic adsorption in the vertical direction was developed. Based on the method, AFM images of fine structures of lymphoma living cells were successfully recorded at tapping mode, and the schematic diagram is shown in Fig. 2.3. Current immobilization methods only consider trapping cells in the horizontal direction [12, 13]. Cells are still motile in the vertical direction, which makes it difficult to image the cell topography with AFM. Here micropillar array chip was fabricated on the silicon substrate which was then covered by a layer of poly-L-lysine, allowing cells trapped in both horizontal and vertical directions. Since cell surface was soft, tapping mode which can efficiently eliminate the influence of lateral forces exerted by the scanning tip on imaging was adopted.

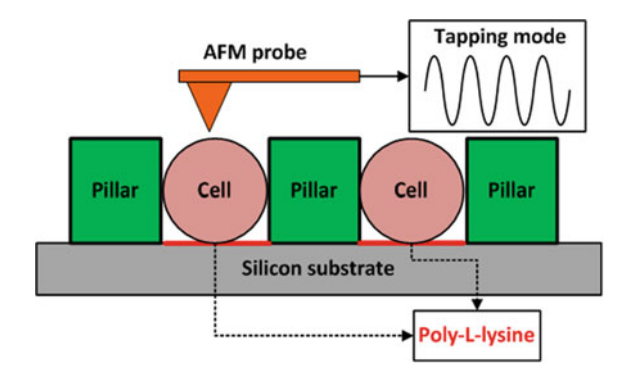


Fig. 2.3 Immobilizing mammalian suspended cells by micropillar trapping and poly-L-lysine electrostatic adsorption. Cellular morphology was acquired by AFM tapping mode imaging

The micropillar array chips were fabricated by photolithography technology [16]. The fabrication process includes photoresist application, exposure, etching, and stripping, as shown in Fig. 2.4a. Figure 2.4b is the photograph of a chip. The length, width, and height of a chip was 20, 10, and 1 mm respectively. The pillar height was 5 μ m, and the pillar diameter was 10 μ m. Because of the variable cell sizes, the distance between two adjacent pillars was designed with three sizes (5, 10, 15 μ m). The chips were imaged by SEM and AFM. From the SEM images (Fig. 2.4c, d), we can see the ordered pillars. Figure 2.4e–g are the AFM height image, three-dimensional image, and section profile of the pillars respectively, showing that the actual height of the pillar was about 4 μ m.

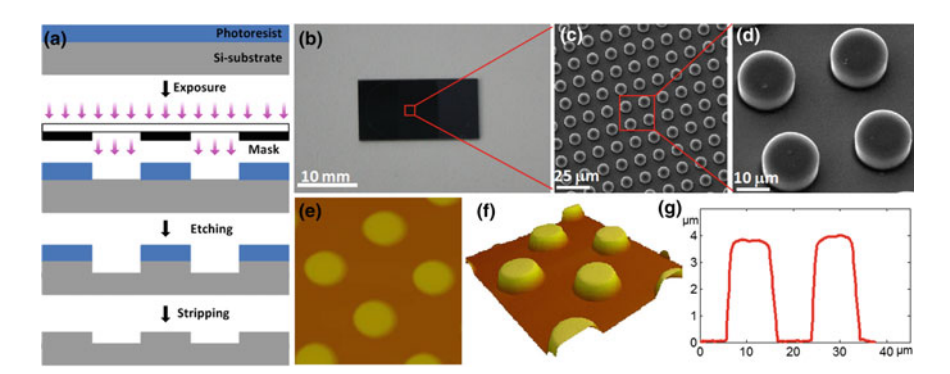


Fig. 2.4 Fabricating micro-pillar array chips with photolithography. **a** Fabricating principle. **b** Photograph of micro-pillar array chip. **c** SEM image of micro-pillar array. **d** SEM image of one unit of micro-pillar. (**e**, **f**) AFM images of micro-pillar unit. **e** Height image. **f** Three-dimensional image. **g** A section profile of two pillars

2.4 Imaging Living Mammalian Suspended Cells Based on Micro-Pillar Immobilization

In order to examine the effectiveness of the presented method, lymphoma Raji cells (a type of mammalian suspended cell) were used for tests. The experimental procedure was following. (1) Raji cells were cultured in RPMI-1640 medium containing 10% fetal bovine serum at 37 °C (5% CO₂) for 24 h. (2) Dilute 0.1% poly-L-lysine 10 times with Milli-O ultrapure water (18.2 M Ω cm) and then drop the poly-L-lysine solution onto the pillar chips and stored at room temperature for air drying. (3) Add 5 ml of cell suspension into an eppendorf tube and centrifuge for 5 min at the speed of 1000 r/min. (4) After the centrifugation, the supernatant of the eppendorf tube was removed and then 1 ml fresh PBS was added into the tube. After stirring the solution with a pipette, a drop of solution was placed onto the poly-L-lysine-coated pillar array chip and incubated for 1 min. (5) The chip was attached to a glass slide using a small piece of double-sided adhesive tape and then placed into a Petri dish containing PBS. (6) After placing the Petri dish on the sample stage of AFM, AFM imaging was immediately performed. Under the guidance of optical microscope, AFM probe was moved to the cells trapped by pillars. The Si₃N₄ probe with a nominal spring constant of 0.12 N/m was used. Imaging was performed in tapping mode with a driving frequency of ~ 9 kHz. The scan rate was 0.5 Hz. The scan line was 256 and the sampling point for each scan line was also 256.

Figure 2.5 shows the results of imaging living Raji cells by AFM tapping mode based on the presented cell immobilization method. Figure 2.5a is the schematic diagram of trapping cells by pillars. Figure 2.5f is the optical image. Large-size scan was performed first to acquire the topography of the whole cell, and then small-size scan was performed to acquire the topography of the cellular local area. Figure 2.5b-e was the AFM height image, phase image, amplitude image, and three-dimensional image of a whole Raji cell respectively. The scan size was 40 μm. Figure 2.5f-i was the AFM height image, phase image, amplitude image, and three-dimensional image of the cellular local area respectively. The scan size was 4 µm. We can see that the Raji cells trapped by pillars could be imaged by AFM. Cells adhered to the substrate in the vertical direction by poly-L-lysine. Pillars trapped cells in the horizontal direction. This allowed the three-dimensional immobilization of the cells. The imaging results showed the corrugated surface of the living Raji cell. Poly-L-lysine electrostatic adsorption alone can attach mammalian suspended cells onto the substrate, but this adsorption is too weak to acquire AFM images on living cells. We have performed AFM imaging on living Raji cells attached on the substrate by poly-L-lysine, and the results showed that the scanning tip could easily move the cells on the substrate (data not shown). Collectively, the experimental results confirmed that the proposed method was suited to trap living mammalian suspended cells for AFM imaging.

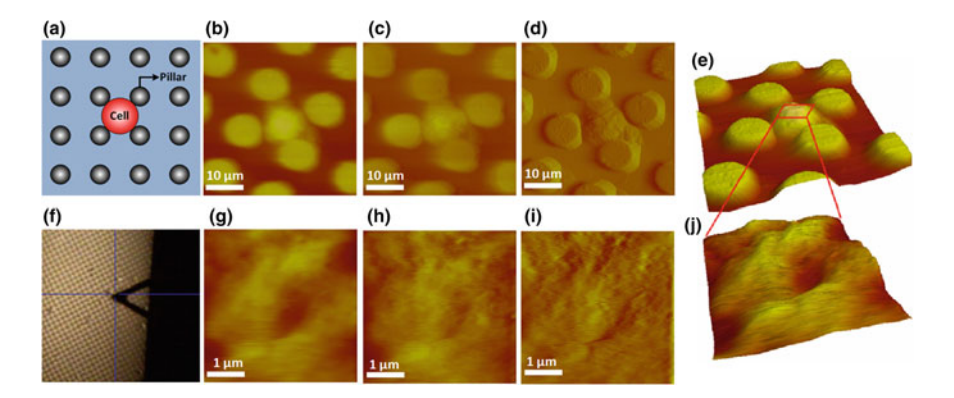


Fig. 2.5 AFM imaging of lymphoma living cells based on the immobilization of pillar mechanical trapping and poly-L-lysine electrostatic adsorption [16]. **a** Principle of mechanical trapping by pillars. (**b**–**e**) AFM images of a whole cell. **b** Height image. **c** Phase image. **d** Amplitude image. **e** Three-dimensional image. **f** Under the guidance of optical image, AFM tip was moved to the trapped cell. (**g**–**j**) AFM images of local area on the cell surface. **g** Height image. **h** Phase image. **i** Amplitude image. **j** Three-dimensional image

2.5 Imaging Living Mammalian Suspended Cells Based on Micro-Well Immobilization

Based on the micropillar chip, polydimethylsiloxane (PDMS) microwell chips were fabricated. Unlike traditional micro-fabrication materials, such as silicon and glass, PDMS is a low-cost material, and PDMS molding processes are simple and rapid [17]. Therefore, we explored fabricating PDMS microwell chips to trap mammalian suspended cells based on the micropillar mold [18]. Liquid PDMS was poured into the pillar mold that was then placed into an 80 °C oven for 2 h. After being separated from the mold, the solid PDMS well chips were acquired. Figure 2.6a is a photo of a PDMS-fabricated well chip and Fig. 2.6e is an optical image of the ordered wells. The height and diameter of the well was 10 and 20 µm respectively. Because PDMS is hydrophobic, the wells should be made hydrophilic before being used for cell immobilization. Hydrophobic wells had rounded drops of PBS, as shown in the AFM images in Fig. 2.6b, c. From the line profile (Fig. 2.6d), we can see that the rounded drop exhibited a parabola shape. If the rounded drop was in the well, cells pushed by the AFM probe could not sink into the well. Several methods can make the PDMS surface hydrophilic, such as plasma cleaning and concanavalin A [19]. We used oxygen plasma to clean the chip for 2 min to make the PDMS surface more hydrophilic, which then allows cells to settle into the wells. AFM images of the chip after being cleaned by oxygen plasma are shown in Fig. 2.6f, g. From the line profile in Fig. 2.6h we can see that the surface wettability of the PDMS ship was enhanced and the rounded drop vanished.

By combining the PDMS microwells and poly-L-lysine electrostatic adsorption, living Raji cells were immobilized for AFM imaging and the results are shown in

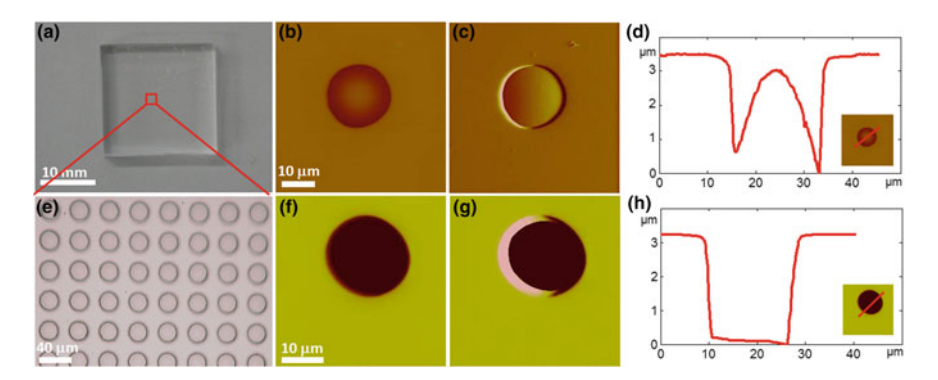


Fig. 2.6 PDMS-fabricated wells and hydrophilic treatment [18]. **a** PDMS well chip. **b**—**c** AFM images of the PDMS well before plasma cleaning. **b** AFM Height image and corresponding **c** deflection image. **d** Line profile. **e** Optical image of the wells. **f** and **g** were the AFM images of PDMS wells after plasma cleaning. **f** AFM height image and corresponding **g** deflection image. **h** Line profile

Fig. 2.7. Figure 2.7a is the schematic diagram of the immobilization based on microwells. The well can help the cells withstand the lateral scanning force and the polv-L-lysine vertically fixes the cells in the well. AFM images were recorded at tapping mode in PBS. The driving frequency of the cantilever was 9.5 kHz. The scan rate was 0.3 Hz. The scan line was 256 and the sampling point for each scan line was also 256. With the assistance of optical image (Fig. 2.7e), the AFM tip was moved onto a cell trapped in a well (denoted by the circle). Figure 2.7b, d, f shows the AFM height image, three-dimensional rendering of the height image, and phase image of the whole cell, respectively. Figure 2.7c, g, h shows the AFM phase image, amplitude image and the three-dimensional rendering of the height image of a local area on the cell, respectively. In the local area, the cell exhibited a rough and corrugated morphology. If the well was not coated by poly-L-lysine, we found that cells in the wells moved during AFM scanning. Poly-L-lysine thus provides an adhesive force between the cell and the bottom surface of the well. The quality of the AFM images of the whole cell are not as good as those obtained when we used micro-fabricated pillars with electrostatic adsorption to immobilize living Raji cells (Fig. 2.5). This may because that silicon is hydrophilic, while PDMS is hydrophobic. Though oxygen plasma treatment can increase the hydrophilicity of PDMS, thare are still significant differences between silicon and PDMS. Furthermore, silicon is stiff, while PDMS is soft, which may also affect the immobilization. Compared with the images of the whole cell (Fig. 2.7b, d, f), the image quality of the reduced area scans (Fig. 2.7c, g, h) was remarkably improved. This is because that as the scan size decreased, the influence of cell membrane movement decreased ant thus the image quality increased.

The proposed micropillar/microwell immobilization methods can be used to immobilize living mammalian suspended cells for AFM imaging, but notably the acquired AFM images have limited spatial resolution. This is because that the

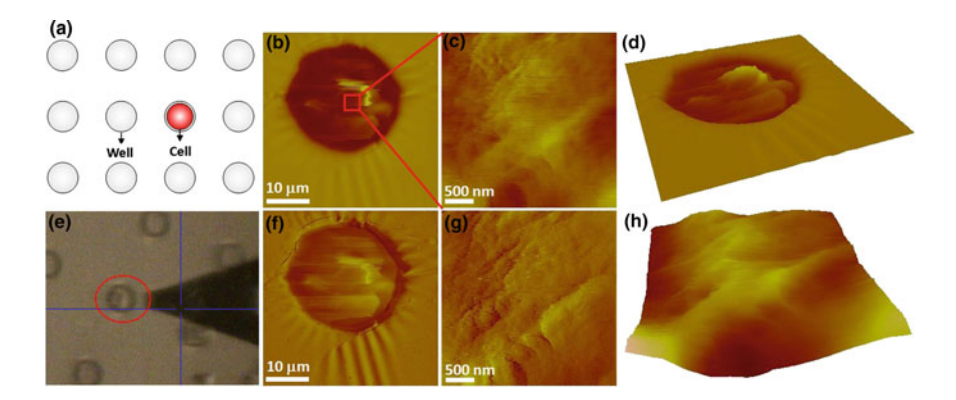


Fig. 2.7 Imaging living Raji cells trapped in PDMS wells in PBS [18]. a Principle of well-based trapping. b Height images of the whole cell. c Phase image of the cellular local area. d Three-dimensional image of the whole cell. e AFM probe was moved to the trapped cell (denoted by the circle) under the guidance of optical image. f Phase image of the whole cell. g Amplitude image of cellular local area. h Three-dimensional image of the cellular local area

micropillar/microwell immobilization only eliminates the influence of the whole cell on AFM imaging, but cannot eliminate the influence of cytomembrane dynamics on AFM imaging. Dague et al. [19] have used PDMS stamps to trap microbial cells (Saccharomyces cerevisiae yeasts and Aspergillus fumigatus fungal spores) for AFM imaging. Microbial cells have stiff cell walls, which allows easier acquisition of high quality of AFM images. In contrast, it is challenging to obtain high quality images of softer and larger mammalian suspended cells, since they are easily deformed by the scanning probe [14]. To increase the AFM spatial resolution, methods that can inhibit the dynamics of the cell membrane are required, such as using films which contain small pores of ~ 100 nm diameter [20]. Cell surface exposed to the pores are relatively rigid and therefore may be imaged. In addition, since the AFM tip can easily deform the soft cell membrane, non-contact AFM imaging techniques, such as scanning ion conductance microscopy (SICM) [14], may potentially improve the spatial resolution of living cell imaging. Novak et al. [21] have used SICM to image the surface living cells with high spatial resolution (about 20 nm). SICM can provide the true topography of soft cells [22], which significantly complements AFM imaging.

2.6 Summary

- (1) Biological experiment platform based on AFM nanorobot was established, which was used to image the topography of three different types of living adherent cells.
- (2) An immobilization method based on micropillar mechanical trapping and poly-L-lysine electrostatic adsorption was developed, which allowed the

- efficient immobilization of mammalian suspended living cells in both horizontal and vertical directions and AFM images of living lymphoma Raji cells were acquired.
- (3) Based on the micropillar, PDMS microwell chips were fabricated. By combining microwell mechanical trapping with poly-L-lysine electrostatic adsorption, living Raji cells were immobilized for successful AFM imaging.

References

- Butt HJ, Wolff EK, Gould SAC et al (1990) Imaging cells with the atomic force microscope. J Struct Biol 105:54–61
- Chao Y, Zhang T (2011) Optimization of fixation methods for observation of bacterial cell morphology and surface ultrastructures by atomic force microscopy. Appl Microbiol Biotechnol 92:381–392
- 3. Yang PH, Sun X, Chiu JF et al (2005) Transferrin-mediated gold nanoparticle cellular uptake. Bioconjugate Chem 16:494–496
- Wu Y, Lu H, Cai J et al (2009) Membrane surface nanostructures and adhesion property of T lymphocytes exploited by AFM. Nanoscale Res Lett 4:942–947
- Dufrene YF (2004) Using nanotechniques to explore microbial surfaces. Nat Rev Microbiol 2:451–460
- Matzke R, Jacobson K, Radmacher M (2001) Direct, high-resolution measurement of furrow stiffening during division of adherent cells. Nat Cell Biol 3:607–610
- Puntheeranurak T, Wildling L, Gruber HJ et al (2006) Ligands on the string: single-molecule AFM studies on the interaction of antibodies and substrates with the Na⁺-glucose co-transporter SGLT1 in living cells. J Cell Sci 119:2960–2967
- Li M, Liu L, Xi N et al (2013) Progress of AFM single-cell and single-molecule morphology imaging. Chin Sci Bull 58:3177–3182
- Dufrene YF (2008) Atomic force microscopy and chemical force microscopy of microbial cells. Nat Protoc 3:1132–1138
- Fantner GE, Barbero RJ, Gray DS et al (2010) Kinetics of antimicrobial peptide activity measured on individual bacterial cells using high-speed atomic force microscopy. Nat Nanotechnol 5:280–285
- 11. Andre G, Kulakauskas S, Chartier MPC et al (2010) Imaging the nanoscale organization of peptidoglycan in living *lactococcus lactis* cells. Nat Commun 1:27
- Rosenbluth MJ, Lam WA, Fletcher DA (2006) Force microscopy of nonadherent cells: a comparison of leukemia cell deformability. Biophys J 90:2994–3003
- Ng L, Hung HH, Sprunt A et al (2007) Nanomechanical properties of individual chondrocytes and their developing growth factor-stimulated pericellular matrix. J Biomech 40:1011–1023
- 14. Muller DJ, Dufrene YF (2011) Force nanoscopy of living cells. Curr Biol 21:R212-R216
- Deng Z, Lulevich V, Liu F et al (2010) Applications of atomic force microscopy in biophysical chemistry of cells. J Phys Chem B 114:5971–5982
- Li M, Liu L, Xi N et al (2011) Imaging and measuring the rituximab-induced changes of mechanical properties in B-lymphoma cells using atomic force microscopy. Biochem Biophys Res Commun 404:689–694
- 17. Jo BH, Lerberghe LMV, Motsegood KM et al (2000) Three-dimensional micro-channel fabrication in polydimethylsiloxane (PDMS) elastomer. J Microelectromech Syst 9:76–81
- 18. Li M, Liu L, Xi N et al (2013) Atomic force microscopy imaging of live mammalian cells. Sci China Life Sci 56:811–817

References 31

 Dague E, Jauvert E, Laplatine L et al (2011) Assembly of live micro-organisms on microstructured PDMS stamps by convective/capillary deposition for AFM bio-experiments. Nanotechnology 22:395102

- Ando T (2012) High-speed atomic force microscopy coming of age. Nanotechnology 23:062001
- 21. Novak P, Li C, Shevchuk AI et al (2009) Nanoscale live-cell imaging using hopping probe ion conductance microscopy. Nat Methods 6:279–281
- 22. Rheinlaender J, Geisse NA, Proksch R et al (2011) Comparison of scanning ion conductance microscopy with atomic force microscopy for cell imaging. Langmuir 27:697–704

Chapter 3 Measuring the Mechanical Properties of Single Cells by AFM

Cell mechanics plays an important role in regulating cellular physiological activities. Cells within tissues are continuously exposed to mechanical cues including hydrostatic pressure, shear stress, compression force, tension force, and extracellular matrix stiffness [1, 2]. Cells dynamically respond to the stimulation of these mechanical cues by modifying their behaviors and remodeling their microenvironments [1]. This response is important in embryonic development as well as adult physiology, and is involved in many diseases, including atherosclerosis, hypertension, osteoporosis, muscular dystrophy, and cancer [3]. The interactions between cells and mechanical cues are often accompanied by the changes of cellular mechanical properties which have been shown to be effective biomarkers for indicating the pathological changes of cells [4]. For example, studies have found that red blood cells (RBCs) obtained from patients with malarial or sickle cell anemia are found to be stiffer and more viscous compared with healthy RBCs [5]. When normal cells become cancerous cells, the cellular elastic modulus significantly decreases: cancerous cells are more than 70% softer than benign cells [6]. The elasticity of cancerous cells is closely related to their metastatic ability: aggressive cancerous cells are softer than indolent cancerous cells [7, 8]. Hence detecting cell mechanics is attracting the attention of researchers for its potentials in complementing clinical medicine diagnosis. So far the diagnosis of cancer mainly relies on the morphological assay of biopsy cells, which is a very complex process, involving surgically removing tissue samples, staining and optical observation [9]. Besides, this method is not always 100% accurate because of the overlap between normal cells and cancerous cells on morphology at times. The detection of cellular mechanical properties can potentially be a useful complement to the traditional morphological assay. A study by Reich et al. [10] has shown that there were no significant differences in morphology between the diseased dermal fibroblasts from scleroderma patients and normal dermal fibroblasts from healthy donors, but diseased fibroblasts had reduced elastic constant than healthy fibroblasts, demonstrating the active role of detecting cellular mechanical properties in recognizing pathological cells. Plodinec et al. [11] have showed that there are significant differences in stiffness maps between normal breast tissues, benign breast tissues and malignant breast tissues, confirming the indicative role of cell mechanics in cellular physiological processes.

3.1 Current Status of Measuring Cell Mechanics by AFM

AFM was initially utilized to measure the mechanical properties of biomaterials in the early 1990s [12-15]. In 1992, Tao et al. [13] measured the local Young's modulus of cow tibia, and the experimental results proved that quantitative data on the mechanical properties of biomaterials can be obtained with unprecedented resolution by AFM. In 1995, Radmacher et al. [14] measured the Young's modulus of mica coated with gelatin films in different liquids (including water, propanol, and mixtures of the two liquids), showing that the measured Young's modulus of gelatin varied from 20 kPa to 0.1 GPa depending on the ratio of propanol to water. In 1991, Maivald et al. [15] simultaneously obtained the height image and stiffness image of the carbon fibre and epoxy composite by AFM force modulation technology and the results revealed the mechanical variations between the two materials, showing the potential of AFM in directly investigating the relationships between structural and mechanical properties of biomaterials. Since the mid-1990s, researchers began to utilize AFM indentation technique to measure the mechanical properties of living cells [16, 17]. In 1994, Hoh et al. [16] investigated the morphology and mechanical properties of Madin-Darby canine kidney (MDCK) cells, showing that the spring constant of MDCK cells was about 0.002 N/m. In 1996, Radmacher et al. [17] quantified the Young's modulus of human platelets by adhering them to the glass substrate and the results showed that the Young's modulus of human platelets were in the range of 1-50 kPa. With AFM indentation technique, we can monitor the dynamics of cell mechanics either by adding chemical molecules that can alter the cells or activate particular cellular biological activities. In 2000, Rotsch et al. [18] monitored the real-time changes of cellular Young's modulus after the addition of drugs and the results showed that the disaggregation of cytoskeleton proteins can cause the significant changes of cellular Young's modulus. In 2009, Cuerrier et al. [19] monitored the changes of Young's modulus of human umbilical vein endothelial cells (HUVEC) after the stimulation of thrombin and bradykinin, showing that the two physiological agonists can make HUVEC stiffen. By combining AFM with confocal microscopy, in 2009, Pelling et al. [20] investigated the mechanical dynamics of single fibroblasts during early apoptosis. In 2009, Hu et al. [21] measured the Young's modulus of lymphocytes in different states (using drug molecules to control cell states) and found that activated lymphocytes (~20 kPa) had a larger Young's modulus than resting and apoptosis lymphocytes (5–11 kPa). In 2012, Liu et al. [22] quantified the drug-induced mechanical changes of single living cardiomyocytes and found that the contraction force of cardiomyocytes significantly decreased after the stimulation of ibutilide.

The above studies were performed with conventional AFM tips (conical tip). Conical tip is sharp and measures the mechanical properties of cellular local areas, which facilitates us to correlate cellular mechanics with cellular structures (such as cytoskeleton) by simultaneously imaging and measuring cells. However, linking a microsphere to the AFM cantilever to measure cell mechanics can better characterize the mechanics of the whole cell. Using spherical tip to measure the cellular mechanical properties began in the early 2000s. In 2000, Mahaffy et al. [23] measured the Young's modulus of 3T3 fibroblasts (1-3 kPa) by gluing a polystyrene bead to the cantilever. In 2005, Berdyyeva et al. [24] measured the mechanical properties of old and young human epithelial cells using spherical tip (silica bead with 5 µm diameter), showing that the Young's modulus of older cells was 2-4 times larger than younger cells. In 2006, Leporatti et al. [25] measured the mechanics of resting and activated macrophages (lipopolysaccharide-stimulated), indicating that the Young's modulus of macrophages decreased from $1.5 \pm 1.1 \text{ kPa}$ to 0.51 ± 0.31 kPa after the activation. In 2009, Oberleithner et al. [26] investigated the influence of potassium on the stiffness of endothelium cells using spherical tip (10 µm diameter) bead and found that the increase of potassium can soften the endothelial cells. In 2010, Lulevich et al. [27] found that keratinocytes were 6–70 times stiffer than other cell types (e.g., white blood cell, breast epithelial, fibroblast, or neuronal cells) using 40 µm diameter spherical tip. In 2011, Nikkhah et al. [28] used spherical tip to investigate the influence of growth medium on cell mechanics, showing that the reduction of serum in the culture medium can result in the decrease of cellular Young's modulus.

3.2 Principle and Methods of Measuring Cell Mechanics by AFM

The principle of measuring cell mechanics by AFM indenting technology is shown in Fig. 3.1. Cells are immobilized on a substrate (for cell immobilization methods, readers are referred to Chap. 2). The mechanical properties (e.g., Young's modulus) of cells are measured by obtaining force curves on the cells using conical tip (Fig. 3.1a) or spherical tip (Fig. 3.1b). Figure 3.2 shows the optical and SEM images of conical tip and spherical tip. At the force ramp mode, the AFM probe is controlled to perform approach-retract movement in the vertical direction on the cell surface. The deflection of cantilever is detected by a beam of laser via a four-quadrant photodiode position sensitivity detector (PSD) and the vertical distance between probe and substrate is acquired from the positional changes of piezoelectric ceramic driver. Figure 3.1c shows a typical force curve obtained on living cells, which reflects the approach-retract movement of AFM probe. For obtaining a force curve, the AFM probe firstly approaches and touches the cell. Before touching the cell, the deflection of cantilever is constant and the force curve is straight (denoted by the I in Fig. 3.1c). After the tip indents the cell, the deflection

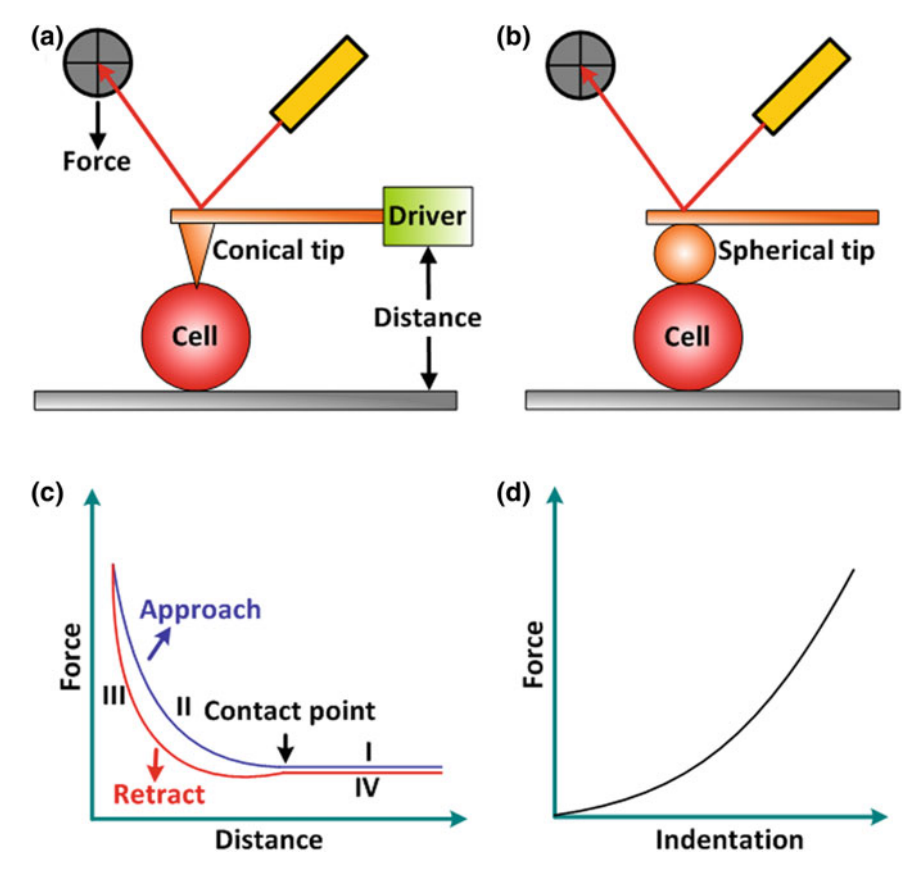


Fig. 3.1 Measuring the cell mechanical properties by AFM. Controlling AFM conical tip (a) or spherical tip (b) to obtain force curves on cells (c, d) Schematic diagram of a force curve (c) and an indentation curve (d)

of cantilever changes and the force curve becomes bent (denoted by the II in Fig. 3.1c). When the loading force of the cantilever reaches the preset value, the tip retracts from the cell (denoted by the III in Fig. 3.1c). The retract curve becomes straight when the tip is separated from the cell (denoted by the IV in Fig. 3.1c). Cellular Young's modulus can be obtained from both approach curve and retract curve depending on the theoretical models applied [29], while the retract curve can also be used for analyzing the adhesion forces [30].

There are many models for extracting the cellular Young's modulus from the AFM-obtained approach curve, mainly including Hertz-Sneddon, Johnson-Kendall-Roberts (JKR), Derjaguin-Muller-Toporov (DMT), and Oliver-Pharr. Hertz model is applicable to spherical tip, while Sneddon extended it to conical tip [31]. Hertz-Sneddon model does not consider electrostatic forces, adhesion or friction between contact surfaces [32]. Hence, Hertz-Sneddon theory can only be applied

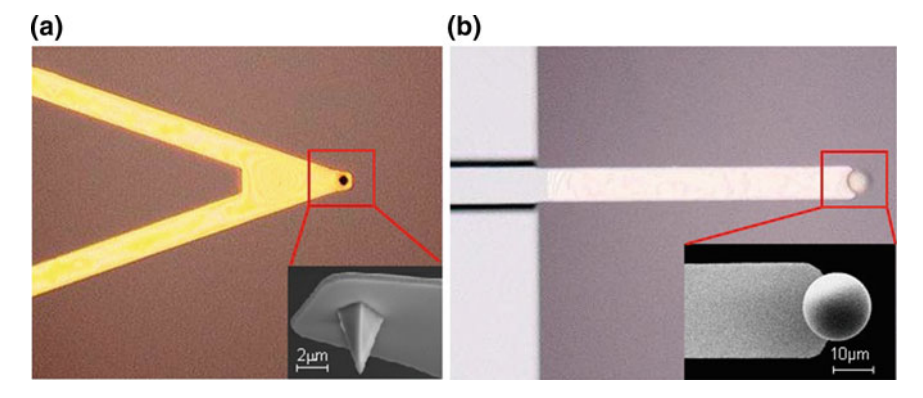


Fig. 3.2 Optical and SEM images (insets) of AFM tips a Conical tip. b Spherical tip

when the adhesion force is much smaller than the maximum load [33]. JKR model considers the adhesion forces inside the contact area whereas DMT model considers the forces outside the contact area [34]. Hence, JKR model can be applied in the case of large tips and soft samples with a large adhesion, and DMT model is applicable in the case of small tips and stiff samples with a small adhesion. Oliver-Pharr model considers the elastic response in the presence of plastic deformations to be the same as in the case of purely elastic deformation and also does not take into account the probe-sample adhesion. In practice, however, Hertz-Sneddon model is the most widely used model [32]. Hertz-Sneddon model is based on several assumptions that the sample being indented is homogeneous, isotropic, and infinitely thick [31]. It is obvious that these assumptions are not truly met in the case of indenting cells (cells are highly heterogeneous and anisotropic with a finite thickness). Nevertheless, studies have shown that when the indentation depth is less than 10% of the cell thickness, Hertz-Sneddon model is applicable [35]. When the indentation depth is larger than 10% of the cell thickness, then the AFM tip will feel the underlying substrate, which will make cells appear stiffer than they really are. In order to avoid the influence of substrate, Gavara et al. [36] integrated a correction factor into Hertz-Sneddon model and the results showed that the corrected model can effectively eliminate the substrate effects for thin samples (such as the peripheral areas of adherent cells). However, this method [36] requires the sample thickness which is obtained independently, increasing the complexity of this method.

By converting an approach curve into an indentation curve (Fig. 3.1d) according to the contact point (the indentation is obtained by subtracting the cantilever deflection from the vertical displacement of the probe), the Young's modulus is extracted by applying Hertz-Sneddon model on the indentation curve. In most cases, the contact point is visually determined by manual [37]. The formulae of Hertz-Sneddon model are:

$$F_{cone} = \frac{2E\delta^2 tan\theta}{\pi} \tag{1}$$

$$F_{sphere} = \frac{4ER^{0.5}\delta^{1.5}}{3} \tag{2}$$

$$\frac{1}{E} = \frac{1 - v_{tip}^2}{E_{tip}} + \frac{1 - v_{cell}^2}{E_{cell}} \tag{3}$$

$$\frac{1}{R} = \frac{1}{R_{tin}} + \frac{1}{R_{cell}} \tag{4}$$

where v_{tip} and v_{cell} are the Poisson ratio of tip and cell respectively, F is the loading force of tip, δ is the indentation depth, E is the effective Young's modulus, E_{tip} is the Young's modulus of tip, E_{cell} is the Young's modulus of cell, θ is the half-opening angle of the tip, R is the effective radius, R_{tip} is the radius of tip, R_{cell} is the radius of cell. Because the Young's modulus of living cells is much less than that of tip ($E_{cell} < E_{tip}$), we can rewrite the formula (3) to:

$$\frac{1}{E} = \frac{1 - v_{cell}^2}{E_{cell}} \tag{5}$$

Then the formula (1) and (2) can be rewritten as:

$$F_{cone} = \frac{2E_{cell}\delta^2 tan\theta}{\pi (1 - v_{cell}^2)} \tag{6}$$

$$F_{sphere} = \frac{4E_{cell}R^{0.5}\delta^{1.5}}{3(1 - v_{cell}^2)} \tag{7}$$

Living cells are often considered as incompressible materials, and thus the v_{cell} is 0.5. According to the Hooke's law:

$$F = kx \tag{8}$$

where k is the spring constant of the cantilever, the loading force F can be calculated from the cantilever deflection x. After obtaining the loading force F and the indentation depth δ , the cellular Young's modulus E_{cell} can be calculated according to the formula (6) and (7). The remaining parameters involved in (6), (7) are known or can be acquired by experimental measurement. The half-opening angle can be obtained from manufacturer or measured by SEM, and the spring constant of cantilever can be exactly calibrated by thermal noise method.

During the indenting process, the AFM tip firstly encounters the glycocalix, then the cytomembrane, and then either the intracellular organelles or the cytoskeleton [38]. For eukaryotic cells, the glycocalix and cytomembrane are very soft and can be neglected in AFM experiments [38]. Cell cytoskeleton is the main factor determining the Young's modulus extracted from the force curves obtained on living eukaryotic cells [39]. In practice, in order to obtain the results with statistical significance, thousands of force curves are often recorded on many cells [34]. For each force curve, a Young's modulus is extracted by applying Hertz-Sneddon model to fit the corresponding indentation curve. Then many Young's modulus values are acquired and distribution of these Young's modulus values is often fitted with Gaussian function (for symmetric histograms) or lognormal distribution (for non-symmetric histograms) [40]. The mean value and standard deviation are acquired from the normal/log-normal distribution fitting, which statistically quantify the different mechanical properties of cells. For example, not only tumor cells have a much smaller mean value of Young's modulus than that of benign mesothelial cells, but also tumor cells display a narrow, spiked peak with little spread, wheareas benign mesothelial cells display a broad peak [6].

3.3 Fabrication of AFM Spherical Tip

The spherical probe was fabricated by gluing a sphere to the cantilever of an AFM probe based on AFM micromanipulation [41]. The detailed process of spherical probe preparation is as follows (Fig. 3.3). (1) An AFM probe was mounted onto the head of AFM and the laser signal reflected off the probe cantilever was adjusted. (2) A drop of the polystyrene sphere solution (the diameter of sphere was $\sim 20 \ \mu m$) was placed on a fresh glass slide and a drop of two-part epoxy adhesive (Araldite adhesive) was placed on another position of the same glass slide by using a toothpick. (3) Under the guidance of optical microscopy, the AFM cantilever was moved to contact the epoxy adhesive and then retracted immediately. (4) The AFM cantilever was moved to contact a single sphere for 10 s and then retracted. After step (4), if the target sphere disappears from the glass slide, then the micromanipulation is successful, else repeating steps (2-4) are needed. Figure 3.3a is the optical image of AFM micromanipulations for gluing spheres and Fig. 3.3b is the optical image of spheres. The prepared spherical probes are placed in a probe box (Bruker, Santa Barbara, CA, USA) for 24 h at room temperature for the hardening of epoxy adhesive. The fabricates spherical probes were imaged by optical microscopy and SEM. Figure 3.3c, d are the optical top view image and SEM side view image of a microsphere glued to a tipless cantilever. With the method, microspheres can also be glued to conventional AFM probe with conical tip, as shown in Fig. 3.3e, f.

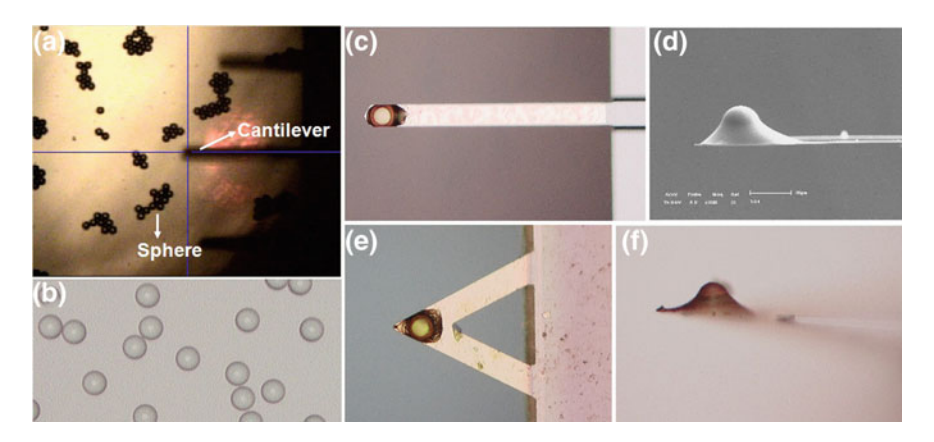


Fig. 3.3 Fabricating spherical probe. **a** Attaching microspheres onto the AFM probe cantilever by epoxy glue. **b** Optical image of microspheres. **c**, **d** A microsphere was glued onto a tipless cantilever. **c** Optical image and **d** SEM side view image. **e**, **f** A microsphere was glued onto a conventional cantilever with cone tip. **e** Optical top view image and **f** side view image

3.4 Measuring the Mechanics of Cancerous Cells with Different Invasive Abilities

With the use of the fabricated spherical tips, the Young's modulus of four types of suspended cells was measured, including RBC, lymphoma Raji cell line, lymphoma Hut cell line, and leukemia K562 cell line. RBCs from healthy volunteers were diluted in phosphate buffered saline (PBS) and harvested by centrifugation for 10 min at 2000 rpm. Raji/Hut/K562 cells were cultured at 37 °C (5% CO₂) in RPMI-1640 containing 10% fetal bovine serum for 24 h before experiments. For AFM imaging, cells were dropped onto poly-L-lysine-coated glass slides and chemically fixed for 30 min by 4% paraformaldehyde. The glass slide was then washed for three times by Milli-Q ultrapure water (18.2 M Ω cm) and dried with a stream of nitrogen. For AFM mechanical measurements, living cells were dropped onto poly-L-lysine-coated glass slides. After one min, the glass slides were placed in a Petri dish containing Hank's balanced salt solution (HBSS).

AFM cell imaging experiments were performed in air using a conventional probe (MLCT, Veeco Company, Santa Barbara, CA, USA) at contact mode with a scan rate of 1 Hz. The scan line was 256 and the sampling point for each scan line was also 256. Force curves were obtained at a constant loading rate and the sampling point for each force curve was 512. The cantilever deflection sensitivity was calibrated on the bare area of the glass slide and then the thermal tune adapter (Veeco Company, Santa Barbara, CA, USA) was utilized to calibrate the spring constant of the cantilever. Five cells of each type (RBCs, Raji, Hut, K562) were selected for measurements and 50 force curves were obtained on each cell. Cell Young's modulus was extracted by fitting the force curves with Hertz-Sneddon model.

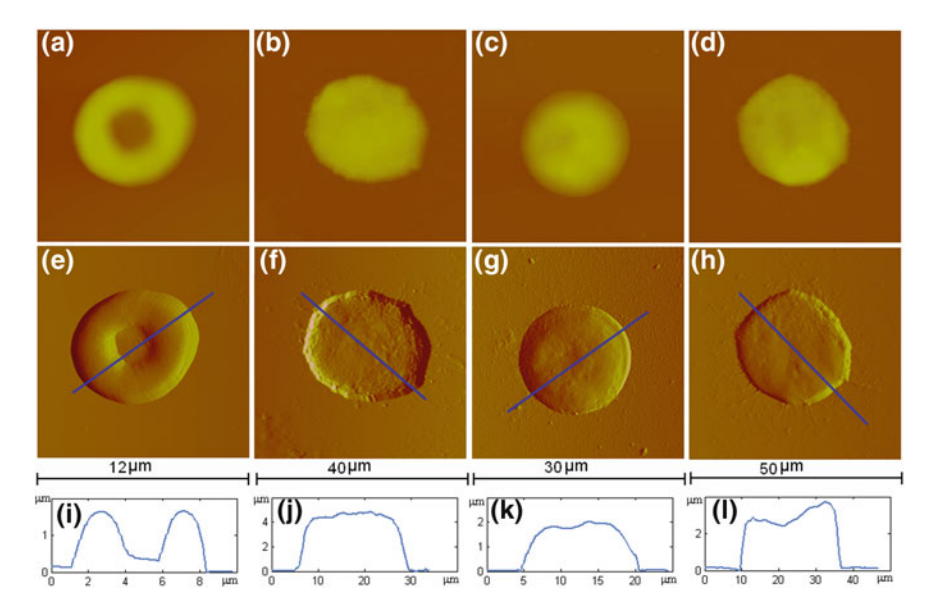


Fig. 3.4 AFM images of RBC, Raji, Hut, K562 cells [8]. (a–h) AFM height images (a–d) and the corresponding deflection images (e–h). a, e RBC. b, f Raji. c, g Hut. d, h K562. i–l Section curves of i RBC, j Raji, k Hut, and l K562 obtained along the lines in (e–h) respectively

Figure 3.4 are AFM images of RBCs, Raji, Hut, and K562 cells. Figure 3.4a, e are AFM height image and deflection image of a RBC respectively. The scan size was 12 µm. The unique bi-concave disk shape can be clearly seen. The section profile (Fig. 3.4 i) indicates that the diameter of the RBC was 7.5 µm. Figure 3.4b, f are AFM images of a Raji cell. The scan size was 40 µm. We can see that Raji cell was plump and circular. The line profile (Fig. 3.4j) reveals that the diameter of the cell is 25 µm. Mature RBCs do not have nuclei and are bio-concave disks, whereas Raji cells have nuclei and exhibit plump shapes. Hut cells and K562 cells are T lymphocytes and neutrophils respectively, both of which have cell nuclei. From the AFM images we can see that both of Hut (Fig. 3.4c, g) and K562 cells (Fig. 3.4d, h) are also circular and plump. From the line profiles, it can be seen that the diameter of the Hut cell is 16 µm (Fig. 3.4k), while the diameter of K562 cell is 28 µm (Fig. 3.41). The RBC is clearly smaller than the three cancerous cells. The normal diameters of healthy human RBCs are 7.5-8.5 µm, whereas the normal diameters of lymphocytes and neutrophils are 6–20 µm and 10–12 µm respectively [8]. We can see that here the RBC diameter measured in Fig. 3.4 is in the normal range. The diameter of the Hut cell measured in Fig. 3.4 is also in the normal range. However, the Raji and K562 cells are significantly larger than their normal counterparts. This may because that the RBCs used here were from healthy volunteers, while Raji and K562 are cancerous cells which are often larger than healthy cells.

Figure 3.5 shows the process of measuring the Young's modulus of RBCs by AFM. Figure 3.5a is a typical force curve recorded on living RBC. The force curve

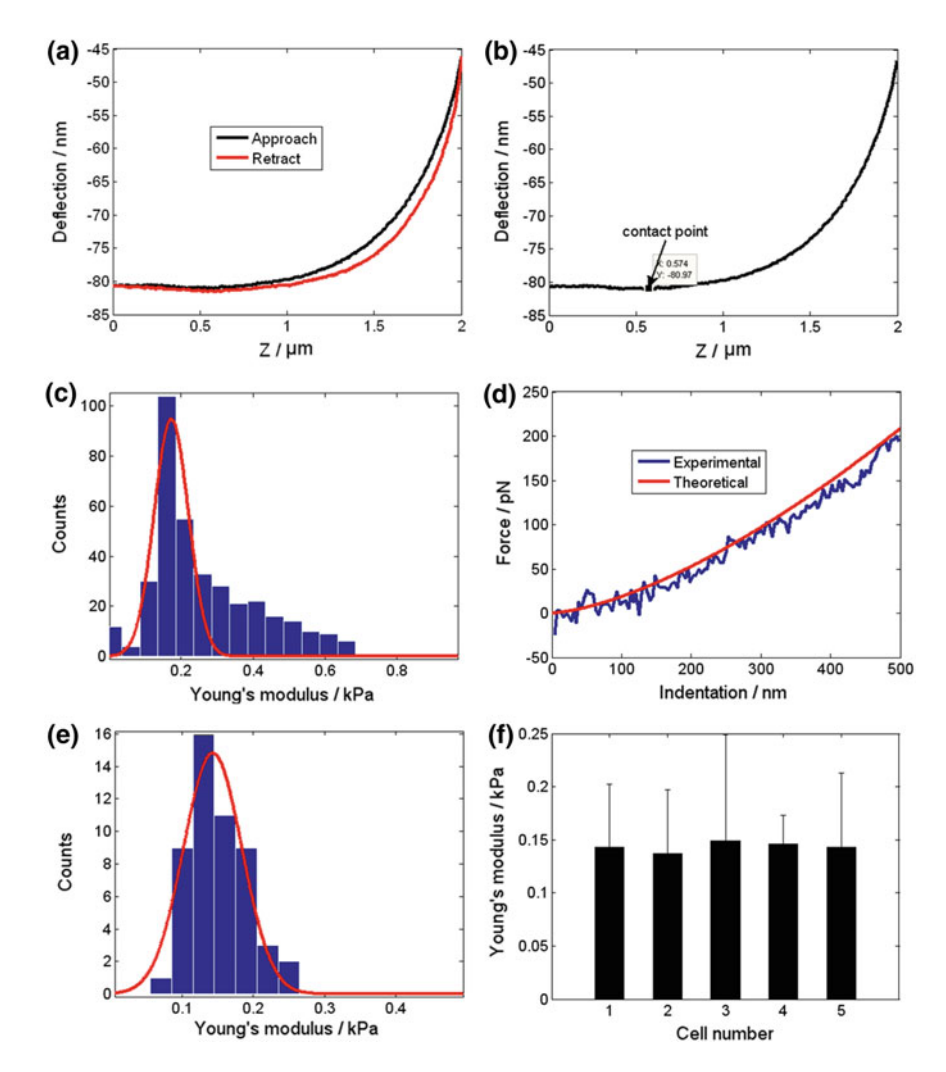


Fig. 3.5 Process of measuring the Young's modulus of RBC by AFM [8]. a A typical force curve recorded on living RBCs. b Approach curve in (a). c Histogram of the Young's modulus extracted from the approach curve (b) and Gaussian fiting. d Contrast of experimental indention curve and theoretical indentation curve. e Histogram of the Young's modulus extracted from many force curves recorded on a cell and Gaussian fit. f Histogram of the Young's modulus of five RBCs

includes an approach curve (black) and a retract curve (red). There is a gap (hysteresis) between approach curve and retract curve, which is caused by cellular viscosity. Cell is viscoelastic, possessing a viscosity of fluids and an elasticity of solids [33]. Besides, the gap is small (the gap between approach curve and retract curve recorded on the other three types of cells was significantly larger than that on RBC), indicating that during the approach-retract process, the viscosity of the RBC

was small and the elasticity was dominant. This is a consistent characteristic of RBCs since they have high elasticity. Biomembrane force probe technology is based on the use of the high elasticity of RBC [42]. The approach curve was converted into an indentation curve according to the contact point (Fig. 3.5b) and then the 500 nm range of the indentation curve was used to compute Young's modulus. For each force curve, there were hundreds of discrete data points and each data points can be used to calculate a Young's modulus. Therefore, many values of Young's modulus were computed from an indentation curve, and a histogram was plotted (Fig. 3.5c). The histogram was well fitted by Gaussian fitting. Insertion of Gaussian fitted Young's modulus (0.173 kPa) into the Hertz model formula produced a theoretical indentation curve that is compared with the experimental data in Fig. 3.5d. The good agreement indicates that the Hertz model is an adequate approximation of the sphere indentation process. For each RBC, 50 force curves were obtained and 50 values of Young's modulus were computed; a histogram is shown in Fig. 3.5e. A Gaussian fit indicates that Young's modulus of the RBC was 0.143 ± 0.059 kPa. Values of Young's modulus for four other RBCs were 0.137 ± 0.06 , 0.149 ± 0.1 , 0.146 ± 0.027 , and 0.143 ± 0.07 kPa. Figure 3.5f is the histogram of Young's modulus of the five RBCs, showing that the Young's modulus of RBCs was about 0.1-0.2 kPa.

By applying the procedure described above, the Young's modulus of Raji, Hut, and K562 cells were measured and the results are shown in Fig. 3.6. We can see that the Young's modulus of Raji, Hut, and K562 cells was 0.2–0.4 kPa, 1–1.4 kPa, and 0.6–0.7 kPa respectively. The Young's modulus of Raji cells measured by conical tip was 150 ± 60 kPa [43, 44], which was significantly larger than the Young's modulus of Raji cells measured by spherical tip (0.2–0.4 kPa) here. This may due to the different cellular structures probed by the tips. Spherical tip has a

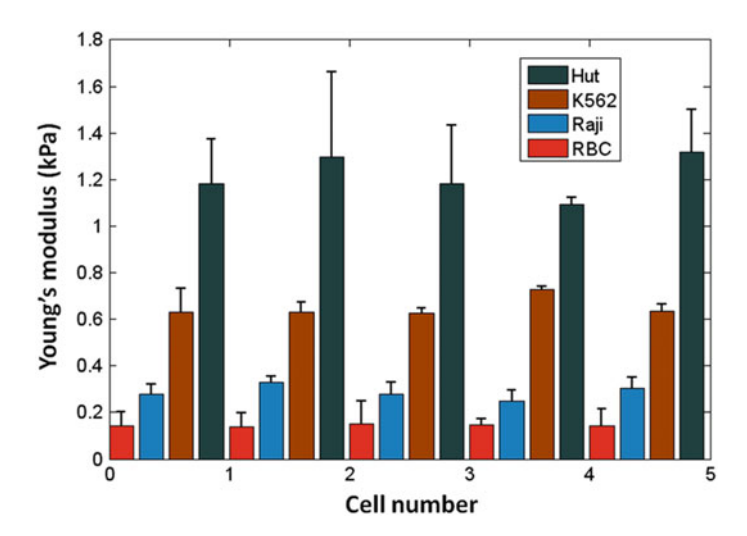


Fig. 3.6 Histogram of the Young's modulus of RBC, Raji, Hut, K562 cells [8]

larger contact area than conical tip. Conical tip primarily probes the cell cortex, whereas spherical tip probes both cortex and the underlying cytoplasm. Cell cortex is an actin-dense region of the cell lying immediately beneath the cell membrane [45]. Cell cortex is much stiffer than the underlying cellular structures (cytoskeleton and cytoplasm), resulting in that the Young's modulus measured by conical tips is larger than that measured by spherical tips [34]. Previously, a study by Nikkhah et al. [28] has shown that the Young's modulus of breast cancerous cells measured by spherical tip was 0.2–1.2 kPa, and Leporatti et al. [25] have shown that the Young's modulus of macrophages was about 0.5 kPa. Here we can see that the Young's modulus of RBCs, Raji, Hut, and K562 cells measured here with spherical tip are comparable to these results.

Comparing the Young's modulus of these four types of cells, we can see that the order of increasing Young's modulus is RBCs (smallest), Raji, K562, and Hut cells (largest). Mature RBCs do not have cell nuclei, whereas the other three types of cells have cell nuclei (as shown in Figs. 3.4, 3.7a), which may result in that RBCs are the softest among the four types of cells. The softness of an RBC makes it easy to deform, facilitating it to traverse narrow capillaries to carry oxygen to various parts of the parts in the body. Comparing the Young's modulus of Raji and Hut cells, we can see that Hut cells are much stiffer. Raji cells are from Burkitt's lymphoma that is an aggressive, malignant B-cell lymphoma characterized by a high degree proliferation [46]. The Hut cells are from Sezary syndrome, which is a cutaneous T-cell lymphoma characterized by indolent malignant cells [47]. We can see here that Raji cells are significantly softer than Hut cells. K562 cells are also from a type of indolent chronic myeloid leukemia cells [48], and we can see that K562 cells are significantly stiffer than Raji cells.

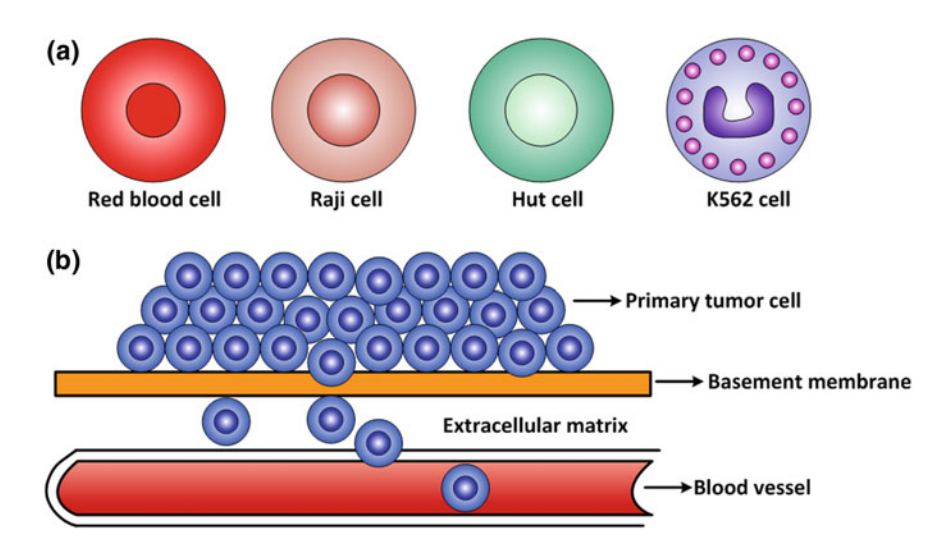


Fig. 3.7 Cell mechanics and cancer metastasis [8]. a Structure of RBC, Raji, Hut, K562 cells. b Cancer metastasis process

As shown in Fig. 3.7b, in the process of cancer metastasis from a primary site to a distant site, cancerous cells must successively pass through the basement membrane, the extracellular matrix, and the blood vessel walls [49]. The cancerous cells survive the harsh conditions within blood vessels and squeeze out of them in distant sites. Jin et al. [50] investigated the mechanical properties of breast cancerous cells after treatment with bone morphogenetic protein (BMP) which promotes cell migration. The results showed that the cells became softer after BMP stimulation. Cross et al. [6] have shown that cancerous cells were much softer than normal cells. These results indicate that cell stiffness plays an important role in cell movement. Softness may make it easier for cancerous cells to cross various obstacles in the body. Hence it is reasonable that cancerous cells with different metastatic capabilities may have different stiffness. For the three cancerous cells investigated here, Raji cells are the most aggressive and the softest, while the Hut and K562 cells are indolent and stiffer, showing the close links between cell stiffness and cancerous cell metastasis abilities. Cellular mechanical properties are closely related to their structures, such as the cytoskeleton. The results here indicated that aggressive cancerous cells are softer than indolent cancerous cells, providing a mechanical insight into cancer metastasis. However, the underlying mechanisms that cause these differences are unknown and further researches (e.g., comparison of cytoskeletons between cancerous cells with different stiffness) are required.

3.5 Summary

- (1) The procedure of measuring cellular Young's modulus by AFM was established and AFM spherical tip was fabricated with the use of epoxy glue based on AFM micromanipulations.
- (2) With the use of spherical tip, the Young's modulus of RBCs and three types of cancerous cells with different invasive capabilities were measured, showing that aggressive cancerous cells were significantly softer than indolent cancerous cells.

References

- Butcher DT, Alliston T, Weaver VM (2009) A tense situation: forcing tumor progression. Nat Rev Cancer 9:108–122
- Discher DE, Janmey P, Wang Y (2005) Tissue cells feel and respond to the stiffness of their substrate. Science 310:1139–1143
- 3. Hoffman BD, Grashoff C, Schwartz MA (2011) Dynamic molecular processes mediate cellular mechanotransduction. Nature 475:316–323
- 4. Di Carlo D (2012) A mechanical biomarker of cell state in medicine. J Lab Autom 17:32-42
- Lee GYH, Lim CT (2007) Biomechanics approaches to studying human diseases. Trends Biotechnol 25:11–118

- Cross SE, Jin YS, Rao JY et al (2007) Nanomechanical analysis of cells from cancer patients. Nat Nanotechnol 2:780–783
- 7. Xu W, Mezencev R, Kim B et al (2012) Cell stiffness is a biomarker of the metastatic potential of ovarian cancer cells. PLoS ONE 7:e46609
- Li M, Liu L, Xi N et al (2012) Atomic force microscopy imaging and mechanical properties measurement of red blood cells and aggressive cancer cells. Sci China Life Sci 55:968–973
- 9. Suresh S (2007) Elastic clues in cancer detection. Nat Nanotechnol 2:748-749
- Reich A, Meurer M, Eckes B et al (2009) Surface morphology and mechanical properties of fibroblasts from scleroderma patients. J Cell Mol Med 13:1644–1652
- 11. Plodinec M, Loparic M, Monnier C et al (2012) The nanomechanical signature of breast cancer. Nat Nanotechnol 7:757–765
- 12. Li M, Liu L, Xi N et al (2014) Research progress in quantifying the mechanical properties of single living cells using atomic force microscopy. Chin Sci Bull 59:4020–4029
- Tao NJ, Lindsay SM, Lees S (1992) Measuring the microelastic properties of biological material. Biophys J 63:1165–1169
- Radmacher M, Monika F, Hansma PK (1995) Imaging soft samples with the atomic force microscope: gelatin in water and propanol. Biophys J 69:264–270
- 15. Maivald P, Butt HJ, Gould SAC et al (1991) Using force modulation to image surface elasticities with the atomic force microscope. Nanotechnology 2:103–106
- Hoh JH, Schoenenberger CA (1994) Surface morphology and mechanical properties of MDCK monolayers by atomic force microsocopy. J Cell Sci 107:1105–1114
- 17. Radmacher M, Fritz M, Kacher CM et al (1996) Measuring the viscoelastic properties of human platelets with the atomic force microscope. Biophys J 79:556–567
- 18. Rotsch C, Radmacher M (2000) Drug-induced changes of cytoskeleton structure and mechanics in fibroblast: an atomic force microscopy study. Biophys J 78:520–535
- Cuerrier CM, Gagner A, Lebel R et al (2009) Effect of thrombin and bradykinin on endothelial cell mechanical properties monitored through membrane deformation. J Mol Recognit 22:389–396
- Pelling AE, Veraitch FS, Chu CPK et al (2009) Mechanical dynamics of single cells during early apoptosis. Cell Motil Cytoskeleton 66:409

 –422
- 21. Hu M, Wang J, Zhao H et al (2009) Nanostructure and nanomechanics analysis of lymphocyte using AFM: from resting, activated to apoptosis. J Biomech 42:1513–1519
- Liu Y, Feng J, Shi L et al (2012) In situ mechanical analysis of cardiomyocytes at nano scales.
 Nanoscale 4:99–102
- Mahaffy RE, Shih CK, MacKintosh FC et al (2000) Scanning probe-based frequencydependent microrheology of polymer gels and biological cells. Phys Rev Lett 85:880–883
- Berdyyeva TK, Woodworth CD, Sokolov I (2005) Human epithelial cells increase their rigidity with ageing in vitro: direct measurements. Phys Med Biol 50:81–92
- Leporatti S, Gerth A, Kohler G et al (2006) Elasticity and adhesion of resting and lipopolysaccharide-stimulated macrophages. FEBS Lett 580:450–454
- Oberleithner H, Callies C, Kusche-Vihrog K et al (2009) Potassium softens vascular endothelium and increases nitric oxide release. Proc Natl Acad Sci USA 106:2829–2834
- Lulevich V, Yang H, Isseroff RR et al (2010) Single cell mechanics of keratinocyte cells. Ultramicroscopy 110:1435–1442
- 28. Nikkhah M, Strobl JS, Schmelz EM et al (2011) Evaluation of the influence of growth medium composition on cell elasticity. J Biomech 44:762–766
- 29. Gavara N (2017) A beginner's guide to atomic force microscopy probing for cell mechanics. Microsc Res Tech 80:75–84
- 30. Li M, Liu L, Xi N et al (2013) Mapping CD20 molecules on the lymphoma cell surface using atomic force microscopy. Chin Sci Bull 58:1516–1519
- Radmacher M (2007) Studying the mechanics of cellular processes by atomic force microscopy. Methods Cell Biol 83:347–372
- 32. Kasas S, Longo G, Dietler G (2013) Mechanical properties of biological specimens explored by atomic force microscopy. J Phys D Appl Phys 46:133001

References 47

33. Butt HJ, Cappella B, Kappl M (2005) Force measurements with the atomic force microscope: technique, interpretation and applications. Surf Sci Rep 59:1–152

- 34. Li M, Dang D, Liu L et al (2017) Atomic force microscopy in characterizing cell mechanics for biomedical applications: a review. IEEE Trans Nanobiosci 16:523–540
- 35. Kuznetsova TG, Starodubtseva MN, Yegorenkov NI et al (2007) Atomic force microscopy probing of cell elasticity. Micron 38:824–833
- 36. Gavara N, Chadwick RS (2012) Determination of the elastic moduli of thin samples and adherent cells using conical atomic force microscopy tips. Nat Nanotechnol 7:733–736
- Bruckner BR, Noding H, Janshoff A (2017) Viscoelastic properties of confluent MDCK II cells obtained from force cycle experiments. Biophys J 112:724–735
- 38. Radmacher M (2002) Measuring the elastic properties of living cells by the atomic force microscope. Methods Cell Biol 68:67–90
- 39. Fletcher DA, Mullins RD (2010) Cell mechanics and the cytoskeleton. Nature 463:485-492
- Lekka M (2016) Discrimination between normal and cancerous cells using AFM. Bionanoscience 6:65–80
- 41. Li M, Liu L, Xiao X et al (2016) Effects of methotrexate on the viscoelastic properties of single cells probed by atomic force microscopy. J Biol Phys 42:551–569
- 42. Merkel R, Nassoy P, Leung A et al (1999) Energy landscapes of receptor-ligand bonds explored with dynamic force spectroscopy. Nature 397:50–53
- Li M, Liu L, Xi N et al (2011) Imaging and measuring the rituximab-induced changes of mechanical properties in B-lymphoma cells using atomic force microscopy. Biochem Biophys Res Commun 404:689–694
- 44. Li M, Liu L, Xi N et al (2012) Drug-induced changes of topography and elasticity in living B lymphoma cells based on atomic force microscopy. Acta Phys Chim Sin 28:1502–1508
- 45. Vargas-Pinto R, Gong H, Vahabikashi A et al (2013) The effect of endothelial cell cortex on atomic force microscopy measurements. Biophys J 105:300–309
- 46. Dave SS, Fu K, Wright GW et al (2006) Molecular diagnosis of Burkitt's lymphoma. N Engl J Med 354:2431–2442
- 47. Diamandidou E, Cohen PR, Kurzrock R (1996) Mycosis fungoides and sezary syndrome. Blood 88:2385–2409
- 48. Deininger MWN, Goldman JM, Melo JV (2000) The molecular biology of chronic myeloid leukemia. Blood 96:3343–3356
- 49. Kiberstis PA (2016) Metastasis: an evolving story. Science 352:162-163
- Jin H, Pi J, Huang X et al (2012) BMP2 promotes migration and invasion of breast cancer cells via cytoskeletal reorganization and adhesion decrease: an AFM investigation. Appl Microbiol Biotechnol 93:1715–1723

Chapter 4 Single-Molecule Recognition and Force Measurements by AFM

Membrane proteins account for 30% of human proteins and are critical for the fulfillment of many cellular biological functions, including signal transduction, energy conversion, solute transport and secretion, enzymatic activities, anchoring of the cytoskeleton, cell adhesion, and motility [1, 2]. Malfunction of membrane proteins is often accompanied by diseases [3], and thus membrane proteins are important targets for treating related diseases. In fact, more than half of the approved drugs target human membrane proteins [4–6]. Despite their importance, the structures of most membrane proteins are still unknown [7]. Due to the amphiphilic nature of membrane proteins, there are many challenges when we apply traditional structural biology methods (e.g., X-ray crystallography) to investigate membrane proteins, mainly in protein expression, purification, and crystallization [8]. Some three-dimensional structures of membrane proteins have been determined [9, 10]. However, since the synthesis of membrane protein in the cell is poorly understood [11] and it is difficult to select adequate detergents to dissolve proteins from cell membrane [12], specific experimental procedures must be developed for particular membrane proteins. There is unlikely to be a single 'one-size-fits-all' protocol suited for all membrane proteins [13]. Besides, structural biology methods investigate membrane proteins which are extracted from the cell membrane, and thus the results cannot faithfully reflect the real activities of native proteins [14]. Experiments have shown that the membrane is not a passive bystander in the function of membrane proteins but can at times have an essential role in determining the function of these proteins [15]. Because of the relative inaccessibility of membranes to classical biochemical methods, information about how proteins interact with lipids to carry out their function is still scarce [16–18], and thus methods that can quantitatively analyze the membrane effects are needed [17].

The advent of AFM provides a new tool for investigating native membrane proteins. Compared with classical structural biology methods, AFM can be used to

image the morphology of single native membrane proteins with high resolution and can also quantitatively measure their mechanical properties, without the need of detergents for extracting the proteins from the cell membranes [3]. With continuous improvements, such as high-speed AFM [19], AFM can sense unique information which significantly complements traditional structural biology. By attaching cell membranes onto flat supports, AFM can directly image two-dimensional morphologies of single native membrane proteins [20] and track the real-time motion of single proteins in the cell membrane [21]. Besides morphology imaging, another successful application of AFM in membrane protein investigation is single-molecule force spectroscopy (SMFS) [22], which allows us to understand the mechanical behaviors of native membrane proteins. In SMFS, AFM uses a functionalized tip to recognize the individual membrane proteins on the cell surface and quantify the binding affinity of the proteins to their antibodies, which is useful for us to understand the dynamics between molecular interactions.

4.1 Current Status of AFM Single-Molecule Force Measurements

The development of SMFS began with purified proteins in the mid-1990s. In 1994, Florin et al. [23] firstly used AFM to measure the unbinding force of individual molecular pair. AFM tip was firstly coated by a layer of biotinylated bovine serum albumin (BSA) and then incubated with avidin molecules. The AFM tip was moved to biotinylated agarose beads to obtain force curves. The obtained force curves clearly showed the adhesion peaks caused by the rupture of biotin-avidin pair. In 1996, Hinterdorfer et al. [24] measured single antibody-antigen recognition events by linking antibodies to the surface of AFM tip via a polyethylene glycol (PEG) spacer molecule. The length of the PEG molecule was about 8 nm. The antigen proteins were adsorbed onto mica by the same PEG spacer molecule. The density of antibodies on tips was adjusted to best meet the expectation that only one antibody might interact with the mica surface. The force curve showed a significantly specific unbinding peak and the rupture force of the single antigen-antibody bond was calculated from the magnitude of the peak. By attaching purified proteins onto substrates, various types of molecular forces have been measured by AFM, including ferritin [25], cadherin [26], and sLex-selectin [27].

Directly probing the native membrane proteins on cell surface can provide novel insights in understanding the molecular activities. In 2006, Puntheeranurak et al. [28] investigated molecular forces on SGLT1-transfected live Chinese hamster ovary (CHO) cells with AFM tips functionalized with an epitope-specific antibody which specifically binds to SGLT1. The specificity of molecular interactions was confirmed by the absence of events in nontransfected CHO cells and by the use of free antigen and free antibody superfusion. This study demonstrates the potential of AFM to study the presence and dynamics of plasma membrane transporters in intact

cells at the single-molecule level. In 2007, Yu et al. [29] investigated the molecular interactions of transforming growth factor β_1 (TGF- β_1) on live HEK 293 cells. By positioning TGF-β₁-modified tips on the cells expressing fluorescent protein tagged TGF-β receptors, the living cell force measurement was realized with a combined fluorescence microscopy and AFM, and the results revealed that the co-expression of T β RI with T β RII enhanced the binding force of TGF- β_1 . In 2009, Shi et al. [30] applied SMFS to study the effect of Herceptin on a HER2-modulated ligandreceptor interaction on living cells. The results demonstrated a more stable binding of Heregulin to the cells co-expressing HER3 and HER2 than to those expressing HER3 alone. Besides, the binding force of Herceptin and HER2 is as strong as that of HRG and HER3/HER2. In 2010, Carvalho et al. [31] applied SMFS on erythrocytes. The results demonstrated the existence of a single molecule interaction between fibrinogen and an unknown receptor on the erythrocyte membrane, with a lower but comparable affinity relative to platelet binding (79 pN). In 2012, Zhang et al. [32] investigated the specific molecular interactions between LHRH and LHRH-R on live HeLa cells. In 2013, Li et al. [33] investigated the specific molecular interactions between the extracellular matrix protein Tenascin-C and the aptamer GBI-10 on live U251 cells. The binding force and the dissociation constant for the GBI-10/Tenascin-C complex was measured.

4.2 Principle of AFM Single-Molecule Force Spectroscopy

The principle of AFM-based SMFS is shown in Fig. 4.1. In order to probe the target molecules on cell surface, the functionalized tip firstly approaches the cell surface until the maximum load is achieved. Then the tip retracts from cell surface. During the approach-retract process, the force curve is recorded. The force is acquired from the deflection of cantilever which is detected by a beam of laser reflected from the backside of AFM cantilever to a four-quadrant photodiode position sensitivity detector (PSD). The distance between AFM tip and cell surface is acquired by monitoring the positional changes of the piezoelectric ceramic tube in the vertical direction. If the ligands on the tip surface bind to the receptors on cell surface during the contact of tip and cell, the receptor-ligand pairs are pulled by the cantilever when the tip retracts from the cell surface [34]. When the pulling force is larger than the binding strength of the receptor-ligand pair, the receptor-ligand pair ruptures. The unbinding of receptor-ligand pairs can result in specific nonlinear peaks in the retraction curve when using PEG spacers as linkers. The occurrence of nonlinear peak is due to the stretching of PEG linker molecules which have a nonlinear elasticity. We can control the density of ligands on the tip to a low level so that only one receptor-ligand pair forms during the contact of tip and cell. In this case, the nonlinear peak in the retraction curve reflects the unbinding of single receptor-ligand pair and the binding force of single receptor-ligand pair is equal to the magnitude of the unbinding peak.

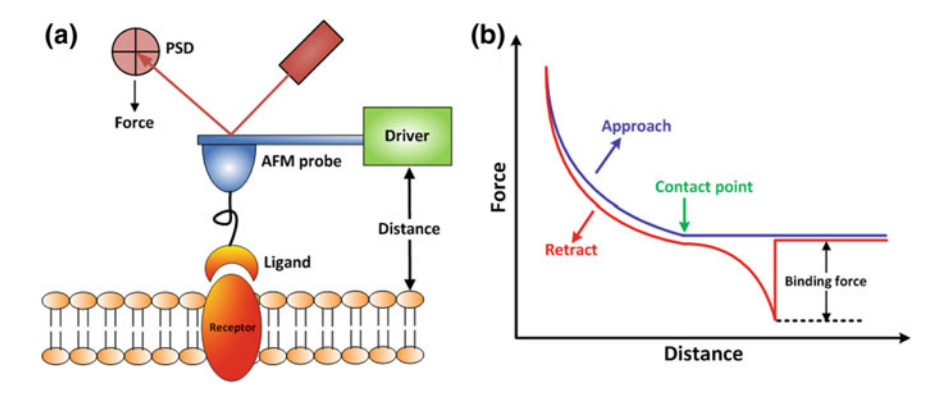


Fig. 4.1 Principle of SMFS [1]. **a** AFM tip carrying ligands is controlled to probe the membrane protein. **b** Schematic diagram of a typical force curve obtained with ligand-functionalized tip. AFM tip firstly approaches cell surface and then retracts from cell surface. A specific peak occurs in the retract curve when pulling force exerted by AFM probe is larger than the binding strength of receptor-ligand pair

The prerequisite for probing molecular interactions is linking ligands onto the AFM tip, which is called tip functionalization. There are mainly three methods for tip functionalization, including protein physisorption, chemisorption of alkanethiols on gold, and covalent coupling of silanes on silicon oxide [35], as shown in Fig. 4.2. The major drawback of protein physisorption is that it often exhibits many molecular binding events during the measurement and therefore it is difficult to accurately measure the binding force of a single molecular pair [1]. The disadvantage of alkanethiol chemisorption is that it requires the tip to be coated with a 5-nm-thick chromium layer, followed by a 30-nm-thick gold layer [36]. This causes

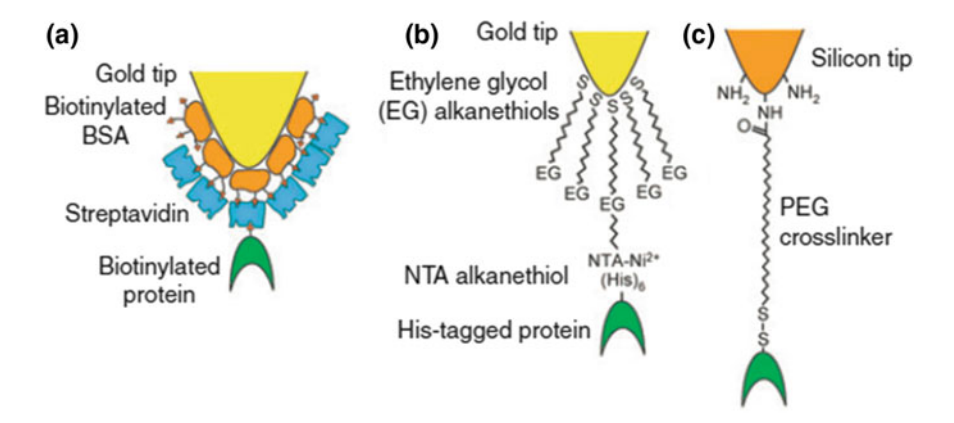


Fig. 4.2 Typical methods for tip functionalization. Reprinted with permission from [35]. Copyright 2006 Nature Publishing Group. **a** Physical adsorption. **b** Chemical adsorption of alkanethiols on gold. **c** Covalent coupling of silanes on silicon oxide

a significant increase in the tip radius and thus decreases the spatial resolution during measurements [37]. The third method is linking proteins onto the AFM silicon tip via PEG spacer molecules, which have several advantages [20]. First, the PEG linker is covalently bound to both AFM tip and proteins, and the covalent bond is much stronger than the receptor-ligand bond [38]. Hence the receptor-ligand bond ruptures first when receptor-ligand pair is pulled by AFM cantilever, which ensures that the unbinding peak is associated only with the receptor-ligand unbinding. Second, the PEG linker allows the ligand to freely reorient to interact with receptors and avoids compressing the receptors [35]. Third, the PEG linker allows a clear distinction between specific and unspecific molecular binding because of the soft and non-linear elasticity of the PEG linker [37]. There are many types of PEG linker molecules, including NHS-PEG-PDP [24], NHS-PEG-MAL [39], and NHS-PEG-Aldehyde [40]. For tip functionalization, the AFM tip is firstly coated by a layer of NH₂. The NHS end of the PEG linker can covalently bind to the NH₂. The PDP (MAL) end of the PEG linker can covalently bind to the thiol groups of the protein. Alternatively, the proteins can be linked to the aldehyde end of the PEG via the lysines in the proteins [35]. Antibodies do not have thiol groups, and thus antibodies are often treated by N-succinimidyl 3-(acetylthio) propionate (SATP) to form thiol groups [40].

4.3 Tip Functionalization and Verification

In order to probe the CD20-rituximab interactions, we used NHS-PEG-MAL spacer to link rituximab onto AFM tip surface according to the procedure in the reference [41]. Figure 4.3a shows the typical instruments and reagents used in tip functionalization, including glass desiccator with argon, pH meter, and electron balance (L204, METTLER TOLEDO, Switzerland). Figure 4.3b shows the schematic diagram of the process of tip functionalization [42]. First, the tip was coated with a

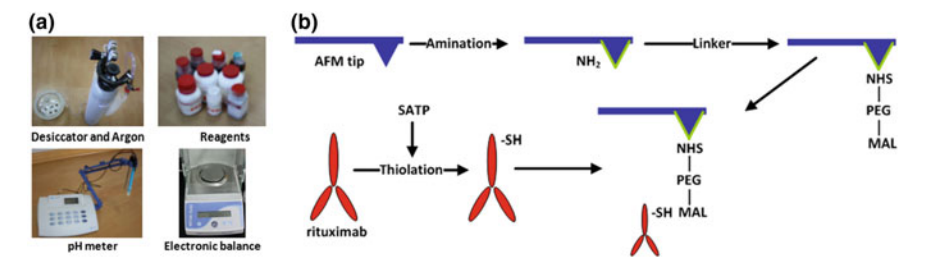


Fig. 4.3 AFM tip functionalization. **a** Experimental instruments. **b** Process of tip functionalization. First a layer of NH₂ was coated on the tip surface and NH₂ can react with the NHS group of the PEG molecule. Then antibodies were treated by SATP to form SH group which can react with the MAL group of the PEG molecule. Therefore, antibodies were linked onto the tip

layer of NH_2 by aminopropyltriethoxysilan (APTES) and N,N-diisopropylethylamine. Then the NHS group of the PEG linker can react with the NH_2 on the AFM tip. The MAL group of the PEG linker can react with the thiol group (SH) which is absent in antibodies. To make rituximab have SH groups, N-succinimidyl 3-(acetylthio) propionate (SATP) was used. After the treatment of SATP, rituximab had SH groups, and then could react with the MAL group of the PEG linker.

The following is the detailed protocol of rituximab functionalization here. (1) Coat AFM tip surface with a layer of NH₂. The glass desiccator is washed by argon for 2 min. 30 uL APTES is placed in a fresh Petri dish and 10 uL N.Ndiisopropylethylamine is placed in another fresh Petri dish. The two dishes are placed in the desiccator. Then the desiccator is washed by argon for 2 min. AFM probe is placed in a container which is then placed in the desiccator. After washing the desiccator by argon for 3 min, the desiccator is sealed for 2 h. (2) Link NHS-PEG-MAL to the NH₂-modified surface. 5 µL triethylamine is dropped into a centrifuge tube and then 20 mg NHS-PEG-MAL is added into the tube. Next, 1 mL chloroform is added into the tube. The mixture is placed in a container. The NH₂modified tip is put into the container and incubate for 3 h. After incubation, the tip is washed by chloroform and dried by argon. (3) Modify rituximab with SATP. 20 µL rituximab (10 mg/mL) and 480 µL buffer solution (100 mM NaCl, 50 mM NaH₂PO₄, 1 mM EDTA, pH 7.5) is added into a centrifuge tube (#1). 0.3 mL dimethyl sulfoxide (DMSO) and 0.5 mg SATP is added into another centrifuge tube (#2). 2 µL SATP solution (from #2) is added into the rituximab solution (#1). (4) Link SATP-treated rituximab to tip. The tip is placed in the mixture of rituximab solution, hydroxylamine (pH 7.5), and buffer (100 mM NaCl, 50 mM NaH₂PO₄, 1 mM EDTA, pH 7.5) and incubate for 1 h. After incubation, tips are washed by PBS and then stored at 4 °C. Rituximab is obtained from Chinese Affiliated Hospital of Military Medical Academy of Sciences (Beijing, China). The NHS-PEG3500-MAL is purchased from JenKem Technology (Beijing. China). The reagents are purchased from Sigma-Aldrich (Saint Louis, MO, USA).

In order to examine whether rituximab was attached to the AFM tip surface, SEM and fluorescence microscopy validation experiments were performed [43]. For SEM experiments, the normal and functionalized probes were attached to a copper substrate and then SEM images were recorded. For fluorescence experiments, the normal and functionalized probes were placed in a Petri dish containing PBS, and then rhodamine-labeled goat anti-human IgG which can specifically bind to rituximab was added into the dish and incubated for 1 h. After incubation, the probes were washed by PBS and then placed at the sample stage of fluorescence microscope (Ti-U-FL, Nikon, Japan) for fluorescence observation. The SEM experimental results are shown in Fig. 4.4. Figure 4.4a, b are the SEM images of a normal probe and Fig. 4.4c, d are the SEM images of a functionalized probe. From SEM images, we can see that there are many particles on the surface of functionalized tip, while the surface of normal tip is smooth. The fluorescence results are shown in Fig. 4.5. Figure 4.5a, b are the optical bright field image and

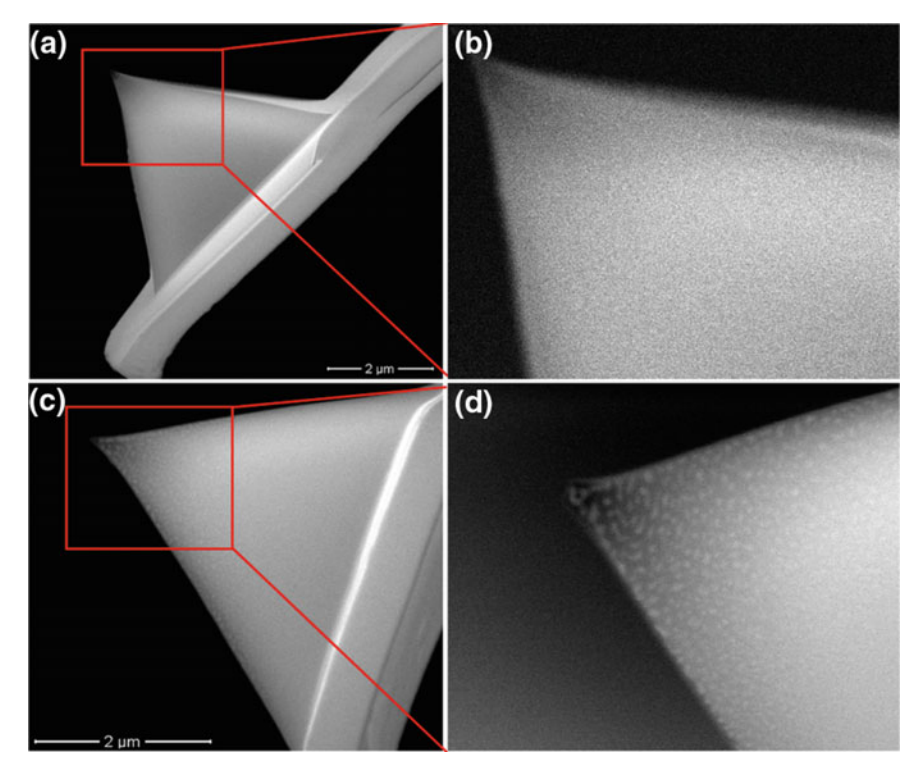


Fig. 4.4 SEM image of a normal probe and a functionalized probe [43]. **a**, **b** A normal probe. **c**, **d** A functionalized probe

fluorescence image of a normal probe. Figure 4.5c, d are the optical bright field image and fluorescence image of a functionalized probe. We can see that the fluorescence of functionalized tip was bright and the fluorescence around the tip (denoted by the white circle in Fig. 4.5d) was obviously brighter than other areas, while the fluorescence of the normal tip was dim. The tip shape was pyramidal and the tip height was in the range of 2.5–8 µm. After the functionalization procedure, rituximabs bound to the tip surface via PEG linker. Rituximabs should also bind to the cantilever of the probe. But the density of rituximabs on the tip was much larger than that on the cantilever. Then after the fluorescence staining, the density of rhodamine-labeled secondary antibody on the tip was much more than on the cantilever, resulting in that the fluorescence of the tip was markedly brighter than that of the cantilever. Collectively, SEM and fluorescence experiments confirmed that there were rituximabs on the tip surface.

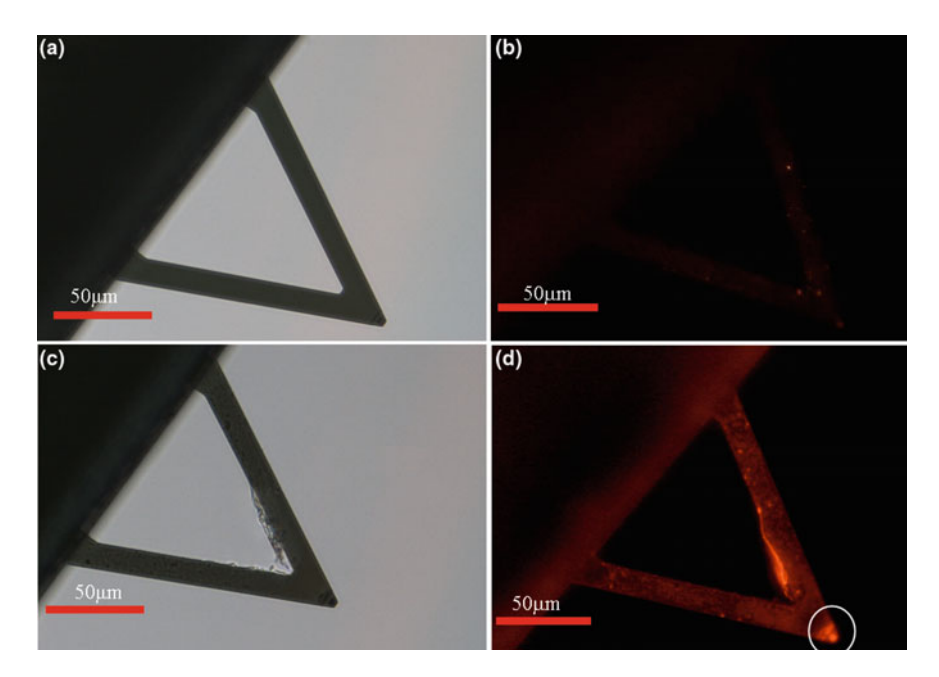


Fig. 4.5 Fluorescence image of a normal probe and a functionalized probe [43]. Optical image (a) and fluorescence image (b) of a normal probe. Optical image(c) and fluorescence image (d) of a functionalized probe

4.4 Measuring the CD20-Rituximab Interaction Forces

With the rituximab-functionalized probe, the CD20-rituximab interactions were examined on purified CD20s attached to mica surface and on native CD20s on lymphoma cell surface.

4.4.1 Purified CD20s on Mica

CD20 proteins were attached to freshly cleaved mica (1 cm \times 1 cm) according to established procedures [44]. A glass desiccator was washed by argon for 2 min. APTES (30 μ L) was pipetted into a small Petri dish and *N*,*N*-diisopropylethylamine (10 μ L) was pipetted into another small Petri dish. The freshly cleaved mica and the two Petri dishes were placed in the glass desiccator. After washing with argon for 2 min, the desiccator was sealed for 2 h to allow the APTES vapor to mix with the *N*,*N*-diisopropylethylamine vapor and form a layer of $-NH_2$ on the mica. Glutaraldehyde solution (200 μ L) was then added to the mica and incubated for 10 min (the glutaraldehyde reacts with the NH_2 on the tip surface). The mica was then rinsed with Milli-Q ultra-pure water. CD20 protein solution (100 μ L) was

added to the mica and incubated for 30 min. The mica was then rinsed with Milli-Q ultra-pure water again and placed in a Petri dish with PBS prior to measurements by AFM. AFM imaging and measurements were performed using a Dimension 3100 AFM (Veeco, Santa Barbara, CA, USA). The cantilever with nominal spring constant 0.06 N/m was used.

Figure 4.6 shows the results of measuring the interactions between purified CD20s and rituximab. After treating the mica with APTES and glutaraldehyde, the exposed aldehydes react with the lysine residues [44]. The CD20 proteins contain

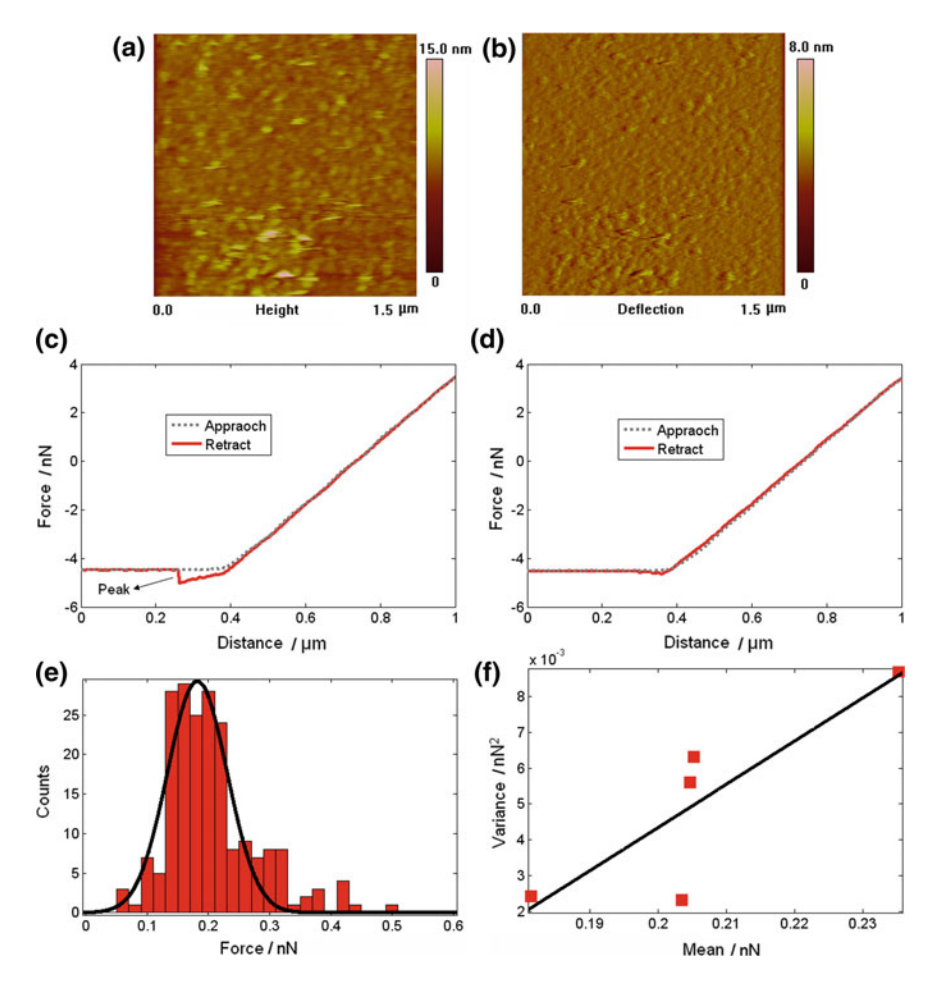


Fig. 4.6 Measurement of the rupture force between purified CD20 proteins and rituximab [44]. **a** AFM contact mode height image and **b** corresponding deflection image of CD20 proteins on mica. **c** A typical force curve with specific unbinding peak. **d** A typical force curve after adding free Rituximab to block the CD20s on mica. **e** Histogram of the rupture forces. **f** Poisson analysis was used to calculate the individual CD20-rituximab rupture force

lysine residues and therefore are cross-linked onto the mica. Figure 4.6a and b show the AFM contact mode images obtained for the purified CD20s. The scan size was 1.5 µm. Figure 4.6a is the height image and Fig. 4.6b is the corresponding deflection image. We can see that many CD20 particles are distributed over the mica surface. The prerequisite of imaging proteins in fluids is attaching them to a flat support [45]. Mica is the most commonly used support because of its atomically flat surface and ease of preparation [46]. However, mica is hydrophilic and protein is hydrophobic, and thus proteins cannot naturally adhere to mica surface [47]. Various methods have been used to attach proteins to mica surfaces, mainly including physical adsorption and covalent attachment [48]. Henderson et al. [47] imaged individual ROMK1 proteins by coating the mica with cetylpyridinium chloride and Kada et al. [49] used AFM to visualize individual ryanodine receptors adsorbed onto mica surfaces in the presence of Ca²⁺. Wang et al. [50] imaged IgG₄ proteins by treating the mica with APTES and glutaraldehyde. However, there is a big gap between imaging single proteins attached on mica and imaging single proteins on living cell surface. In fact, due to the soft, fragile, corrugated and dynamic nature of the cell surface, visualizing individual receptors on living mammalian cells is still a daunting challenge [51].

A typical force curve with specific unbinding peak obtained on CD20-coated mica with rituximab-conjugated probe is shown in Fig. 4.6c. The dotted line indicates the approach curve and the solid line indicates the retract curve. An abrupt peak is visible in the retract curve. When performing tip functionalization for detecting molecular interactions, the bonds between AFM tip and PEG linker molecule, the bonds between rituximab and the PEG linker molecule, and the bonds between the CD20 and the substrate should be much stronger than the bonds between CD20 and rituximab. Researches have shown that the bonds between the NHS end of the PEG linker and the AFM tip are much stronger than protein-protein interactions [24]. Additionally, the bonds between the MAL end of the PEG linker and the antibody, and the bonds between proteins and the aldehyde group on the functionalized mica are also much stronger than protein-protein bonds [40]. Therefore, during the process of stretching the CD20-rituximab pair, the CD20-rituximab complex ruptured first. In order to examine the specificity of the molecular interactions, free rituximabs were added to block the CD20s. After blocking, force curves were recorded again and a typical force curve is shown in Fig. 4.6d. We can see that no peaks were visible on the retract curve, confirming that the peak in Fig. 4.6c corresponded to the specific binding between CD20s on the mica and the rituximabs on the AFM tip. After calculating the rupture forces from the force curves, a histogram of the rupture forces was constructed (Fig. 4.6e). Gaussian fitting of the histogram indicated that the rupture force was $182 \pm 69 \text{ pN}$.

Several CD20-Rituximab complexes might form during the measurements. Therefore, Poisson analysis [52] was used to calculate individual CD20-rituximab rupture forces using the following formula:

$$\frac{\sigma^2}{\mu} = F \tag{1}$$

where σ^2 and μ represent the variance and mean for one measurement, and F is the binding force. If several measurements at the same loading rate are performed, the variance can be plotted against the mean. The individual CD20-rituximab rupture force is then equal to the slope of the fitted line. Five measurements on CD20-coated mica were performed. The mean and variance were calculated for the five measurements. The mean values were 0.2053, 0.1814, 0.2035, 0.2353, and 0.2047, and the variance values were 0.0063, 0.0024, 0.0023, 0.0087, and 0.0056. The fitting function used was $f(x) = p_1 \times x + p_2$, and the results indicated that $p_1 = 0.1205$ and $p_2 = -0.01977$. The slope of the fitting line indicated that the individual rupture force was 121 pN (Fig. 4.6f).

4.4.2 Native CD20s on Lymphoma Cell

Fluorescence labeling experiments were firstly used to examine the distributions of CD20s on lymphoma Raji cell [53]. The Raji cell suspension was dropped onto the glass slide which was coated by poly-L-lysine. The glass slide was then placed in a Petri dish containing PBS. Next, rituximab solution was added into the Petri dish and incubated for 1 h. After incubation, the cell sample was washed by PBS to remove unreacted rituximab. Fresh PBS and FITC-labeled goat anti-human IgG was then added into the Petri dish and incubated for 1 h. After incubation, the cell sample was washed by PBS and observed. The fluorescence results are shown in Fig. 4.7. We can see that the fluorescence of living cells was mainly around the cells, whereas the whole cells exhibited bright fluorescence after being fixed by glutaraldehyde. The fluorescence results confirmed the existence of CD20s on Raji cell.

Figure 4.8 shows the results of probing CD20-rituximab interactions on Raji cells by AFM with rituximab-functionalized tip. Raji cells were cultured at 37 °C (5% CO₂) in RPMI-1640 medium containing 10% fetal bovine serum for 24 h. Harvested Raji cells were dropped onto the poly-L-lysine-coated glass slide and then fixed by glutaraldehyde. The sample was then placed in a Petri dish containing PBS for AFM experiments. Figure 4.8a shows the contact mode height image of a Raji cell. The scan size was 40 μm. To visualize the topography of the local cell surface, the scan size was reduced to 3 μm. Figure 4.8b shows the height image of the local area. From AFM images, it can be seen that the Raji surface is corrugated and rough. A typical force curve with specific unbinding peak recorded on Raji cells with rituximab-conjugated tip is shown in Fig. 4.8c. After adding free rituximabs to block CD20s on Raji cells, force curves were obtained again. A typical force curve obtained after blocking is shown in Fig. 4.8d. We can see that there were no specific unbinding peaks in the retract curve, which confirmed the specific CD20-rituximab binding interactions. Figure 4.8e shows the histogram of the

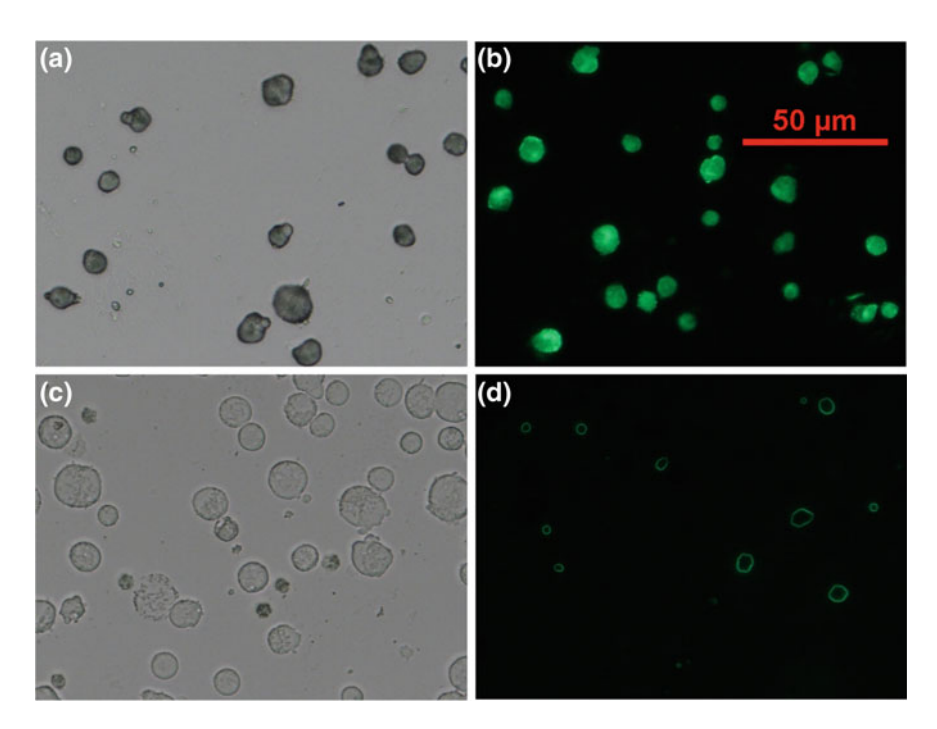


Fig. 4.7 Detecting CD20s on lymphoma Raji cells by fluorescence labeling [53]. Optical bright field image (**a**) and fluorescence image (**b**) of chemically fixed Raji cells. Optical bright field image (**c**) and fluorescence image (**d**) of living Raji cells

CD20-rituximab rupture forces. Gaussian fitting indicated that the rupture force was 162 ± 71 pN. Single CD20-rituximab unbinding force was calculated by Poisson analysis. For five individual measurements, the mean values of forces were 0.1787, 0.2859, 0.2033, 0.1690, and 0.2493, and the variance values of forces were 0.0060, 0.0153, 0.0043, 0.0017, and 0.0059. The slope of the fitted line on the plot of variance against the mean indicated that the individual rupture force was 89 pN (Fig. 4.8f).

We can see that the CD20-rituximab rupture forces for the purified CD20 proteins were a little larger than that of CD20 proteins on Raji cells. This may due to the differences between purified CD20s and native CD20s. The purified CD20s were extracted from prokaryotic cells and thus cannot completely correspond to natural human CD20s. For mammalian proteins, a mammalian expression system is likely to give the best results in terms of protein structure and function [54]. Besides, the conformational structures of CD20s attached onto the mica may be different to that of native CD20s on cell membrane. Gu et al. [55] have shown that the binding force between CD20 and anti-CD20 is closely associated with the structures of linker peptide. Hence the structural differences may account for the different rupture forces measured for the purified CD20s on mica and native CD20s on Raji cells.

4.5 Summary 61

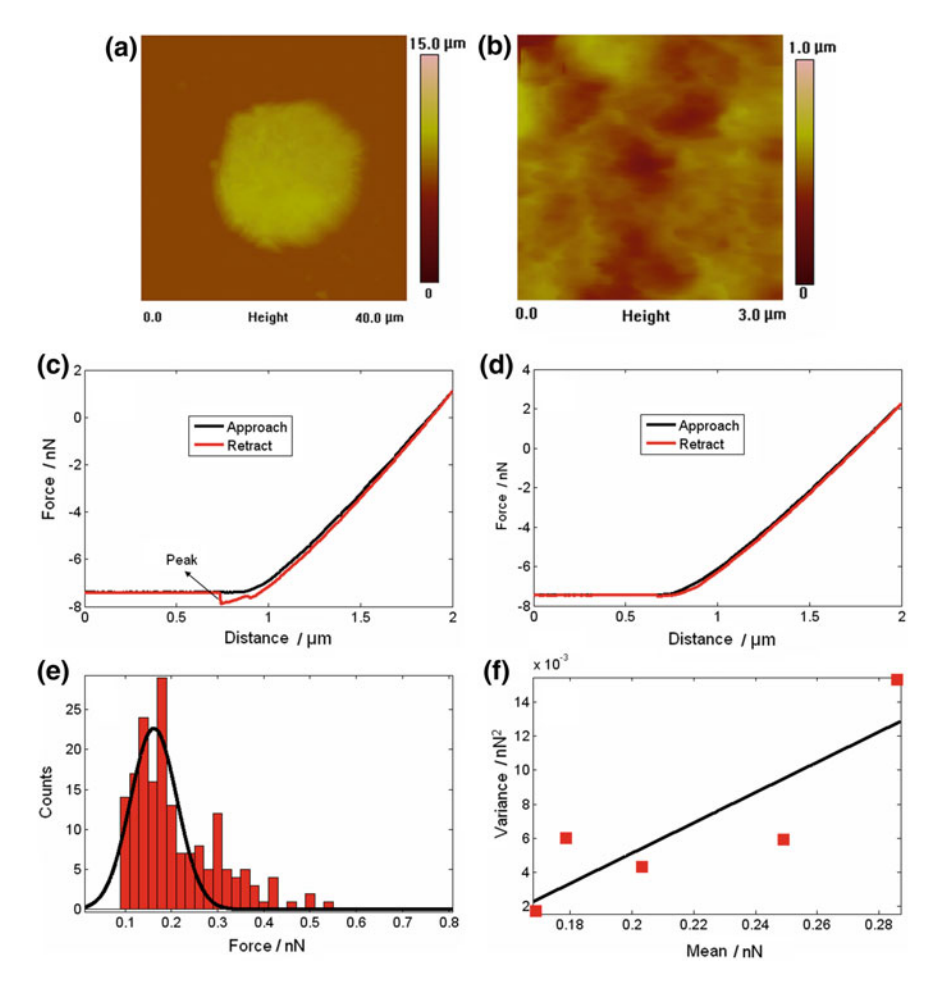


Fig. 4.8 Measurement of the rupture force between CD20s on Raji cells and rituximab [44]. **a** AFM contact mode height image of Raji cells. **b** AFM contact mode height image of the local area of the Raji cell. **c** A typical force curve with specific unbinding peak. **d** A typical force curve after adding free rituximab to block CD20s on Raji cells. **e** Histogram of the rupture forces. **f** Poisson analysis was used to calculate the individual rupture forces

4.5 Summary

- (1) Rituximabs were linked onto AFM tip via NHS-PEG-MAL spacer molecule and the functionalization was verified by SEM and fluorescence experiments.
- (2) CD20-rituximab interaction forces were measured on purified CD20s on mia and native CD20s on lymphoma cell. Single CD20-rituximab interaction force was calculated by Poisson analysis, showing that the rupture forces between rituximab and purified CD20s were larger than that between rituximab and native CD20s on Raji cell.

References

- 1. Li M, Liu L, Xi N et al (2014) Progress in measuring biophysical properties of membrane proteins with AFM single-molecule force spectroscopy. Chin Sci Bull 59:2717–2725
- Bippes CA, Muller DJ (2011) High-resolution atomic force microscopy and spectroscopy of native membrane proteins. Rep Prog Phys 74:086601
- Fotiadis D (2012) Atomic force microscopy for the study of membrane proteins. Curr Opin Biotechnol 23:510–515
- 4. Yildirim MA, Goh KI, Cusick ME et al (2007) Drug-target network. Nat Biotechnol 25: 1119–1126
- Baker M (2010) Making membrane proteins for structure: a trillion tiny tweaks. Nat Methods 7:429–433
- Pieper U, Schlessinger A, Kloppmann E et al (2013) Coordinating the impact of structural genomics on the human α-helical transmembrane proteome. Nat Struct Mol Biol 20:135–138
- Hopf TA, Colwell LJ, Sheridan R et al (2012) Three-dimensional structures of membrane proteins from genomic sequencing. Cell 149:1607–1621
- 8. Robertson JWF, Kasianowicz JJ, Banerjee S (2012) Analytical approaches for studying transporters, channels and porins. Chem Rev 112:6227–6249
- 9. Zhang X, Ren W, Decaen P et al (2012) Crystal structure of an orthologue of the NaChBac voltage-gated sodium channel. Nature 486:130–134
- Ma D, Lu P, Yan C et al (2012) Structure and mechanism of a glutamate-GABA antiporter. Nature 483:632–636
- 11. Bill RM, Henderson PJF, Iwata S et al (2011) Overcoming barriers to membrane protein structure determination. Nat Biotechnol 29:335–340
- 12. Moraes I, Evans G, Sanchez-Weatherby J et al (2014) Membrane protein structure determination-the next generation. Biochim Biophys Acta 1838:78–87
- 13. Doerr A (2009) Membrane protein structures. Nat Methods 6:35
- Oddershede LB (2012) Force probing of individual molecules inside the living cell is now a reality. Nat Chem Biol 8:879–886
- Phillips R, Ursell T, Wiggins P et al (2009) Emerging roles for lipids in shaping membrane-protein function. Nature 459:379–385
- 16. Coskun U, Simons K (2011) Cell membranes: the lipid perspective. Structure 19:1543-1548
- 17. Groves JT, Kuriyan J (2010) Molecular mechanisms in signal transduction at the membrane. Nat Struct Mol Biol 17:659–665
- Fu R, Wang X, Li C et al (2011) In situ structural characterization of a recombinant protein in native Escherichia coli membranes with solid-state magic-angle-spinning NMR. J Am Chem Soc 133:12370–12373
- Ando T, Uchihashi T, Kodera N (2013) High-speed AFM and applications to biomolecular systems. Ann Rev Biophys 42:393–414
- 20. Li M, Dang D, Liu L et al (2017) Imaging and force recognition of single molecular behaviors using atomic force microscopy. Sensors 17:200
- 21. Casuso I, Khao J, Chami M et al (2012) Characterization of the motion of membrane proteins using high-speed atomic force microscopy. Nat Nanotechnol 7:525–529
- 22. Muller DJ, Helenius J, Alsteens D et al (2009) Force probing surfaces of living cells to molecular resolution. Nat Chem Biol 5:383–390
- Florin EL, Moy VT, Gaub HE (1994) Adhesion forces between individual ligand-receptor pairs. Science 264:415–417
- Hinterdorfer P, Baumgartner W, Gruber HJ et al (1996) Detection and localization of individual antibody-antigen recognition events by atomic force microscopy. Proc Natl Acad Sci USA 93:3477–3481
- 25. Allen S, Chen X, Davies J et al (1997) Detection of antigen-antibody binding events with the atomic force microscope. Biochemistry 36:7457–7463

References 63

 Gaumgartner W, Hinterdorfer P, Ness W et al (2000) Cadherin interaction probed by atomic force microscopy. Proc Natl Acad Sci USA 97:4005–4010

- Zhang X, Bogorin DF, Moy VT (2004) Molecular basis of the dynamic strength of the sialyl Lewis X-selectin interaction. ChemPhysChem 5:175–182
- 28. Puntheeranurak T, Wildling L, Gruber HJ et al (2006) Ligands on the string: single-molecule AFM studies on the interaction of antibodies and substrates with the Na⁺-glucose co-transporter SGLT1 in living cells. J Cell Sci 119:2960–2967
- Yu J, Wang Q, Shi X et al (2007) Single-molecule force spectroscopy study of interaction between transforming growth factor β1 and its receptor in living cells. J Phys Chem B 111:13619–13625
- Shi X, Xu L, Yu J et al (2009) Study of inhibition effect of Herceptin on interaction between Heregulin and ErbB receptors HER3/HER2 by single-molecule force spectroscopy. Exp Cell Res 315:2847–2855
- Carvalho FA, Connell S, Miltenberger-Miltenyi G et al (2010) Atomic force microscopy-based molecular recognition of a fibrinogen receptor on human erythrocytes. ACS Nano 4:4609–4620
- Zhang J, Wu G, Song C et al (2012) Single molecular recognition force spectroscopy study of a luteinizing hormone-releasing hormone analogue as a carcinoma target drug. J Phys Chem B 116:13331–13337
- Li Y, Qiao H, Yan W et al (2013) Molecular recognition force spectroscopy study of the dynamic interaction between aptamer GBI-10 and extracellular matrix protein tenascin-C on human glioblastoma cell. J Mol Recogn 26:46–50
- Li M, Liu L, Xi N et al (2015) Biological applications of a nanomanipulator based on AFM: in situ visualization and quantification of cellular behaviors at the single-molecule level. IEEE Nanotechnol Mag 9:25–35
- 35. Hinterdorfer P, Dufrene YF (2006) Detection and localization of single molecular recognition events using atomic force microscopy. Nat Methods 3:347–355
- 36. Dupres V, Menozzi FD, Locht C et al (2005) Nanoscale mapping and functional analysis of individual adhesions on living bacteria. Nat Methods 2:515–520
- 37. Carvalho FA, Santos NC (2012) Atomic force microscopy-based force spectroscopy-biological and biomedical applications. IUBMB Life 64:465–472
- 38. Grandbois M, Beyer M, Rief M et al (1999) How strong is a covalent bond. Science 283:1727-1730
- Fuhrmann A, Ros R (2010) Single-molecule force spectroscopy: a method for quantitative analysis of ligand-receptor interactions. Nanomedicine 5:657–666
- Ebner A, Wildling L, Kamruzzahan ASM et al (2007) A new, simple method for linking of antibodies to atomic force microscopy tips. Bioconjug Chem 18:1176–1184
- Stroh C, Wang H, Bash R et al (2004) Single-molecule recognition imaging microscopy. Proc Nat Acad Sci USA 101:12503–12507
- 42. Li M, Xiao X, Liu L et al (2013) Nanoscale mapping and organization analysis of target proteins on cancer cells from B-cell lymphoma patients. Exp Cell Res 319:2812–2821
- 43. Li M, Xiao X, Liu L et al (2013) Imaging and measuring the molecular force of lymphoma pathological cells using atomic force microscopy. Scanning 35:40–46
- Li M, Liu L, Xi N et al (2011) Detecting CD20-rituximab interaction forces using AFM single-molecule force spectroscopy. Chin Sci Bull 56:3829–3835
- Kada G, Kienberger F, Hinterdorfer P (2008) Atomic force microscopy in bionanotechnology. Nano Today 3:12–19
- 46. Muller DJ, Engel A, Amrein M (1997) Preparation techniques for the observation of native biological systems with the atomic force microscope. Biosens Bioelectron 12:867–877
- Henderson RM, Schneider S, Li Q et al (1996) Imaging ROMK1 inwardly rectifying ATP-sensitive K + channel protein using atomic force microscopy. Proc Natl Acad Sci USA 93:8756–8760
- 48. Kirat KE, Burton I, Dupres V et al (2005) Sample preparation procedures for biological atomic force microscopy. J Microsc 218:199–207

- Kada G, Blayney L, Jeyakumar LH et al (2001) Recognition force microscopy/spectroscopy of ion channels: applications to the skeletal muscle Ca²⁺ release channel (RYR1). Ultramicroscopy 86:129–137
- Wang H, Obenauer-Kutner L, Lin M et al (2008) Imaging glycosylation. J Am Chem Soc 130:8154

 –8155
- 51. Muller DJ, Dufrene YF (2011) Force nanoscopy of living cells. Curr Biol 21:R212-R216
- 52. Stevens F, Lo YS, Harris JM et al (1999) Computer modeling of atomic force microscopy force measurements: comparisons of Poisson, histogram, and continuum methods. Langmuir 15:207–213
- 53. Li M, Liu L, Xi N et al (2010) Detecting CD20-rituximab specific interactions on lymphoma cells using atomic force microscopy. Sci China Life Sci 53:1189–1195
- 54. Werten PJL, Remigy HW, Groot BL et al (2002) Progress in the analysis of membrane protein structure and functions. FEBS Lett 529:65–72
- 55. Gu X, Jia X, Feng J et al (2010) Molecular modeling and affinity determination of scFv antibody; proper linker peptide enhances its activity. Ann Biomed Eng 38:537–549

Chapter 5 Mapping Membrane Proteins on Cell Surface by AFM

Cells sense and respond to the stimuli from the external environments via the various cell surface signaling molecules (e.g., receptor, transporter, ion channel, adhesin). To fulfill their versatile functions, these molecules have heterogeneous properties (e.g., structural, biophysical and biochemical properties) that can change dynamically as required by the cell [1]. Hence understanding the dynamics of molecular activities on the cell surface is important for us to uncover the underlying mechanisms that guide the cellular behaviors [2]. Traditional methods (e.g., X-ray crystallography, electron microscopy) use detergents to isolate the membrane proteins from cell membrane [3]. The purified membrane proteins are detached from cell membrane, while cell membrane plays an important role in modulating the physiological functions of membrane protein [4]. Hence, directly investigating the biophysical and biochemical properties of membrane proteins on cell surface can help us to better understand the molecular behaviors involved in the real situations taking place on cells. To achieve this goal, methods that can recognize the specific membrane proteins are required. The advent of AFM provides a powerful tool for investigating the behaviors of native membrane proteins. In this chapter, AFM was used to rapidly recognize the specific membrane proteins on cell surface and correlate molecular binding events with cellular topography. Quantitative information of molecular distributions on cell surface was also obtained.

5.1 Current Status of Mapping Membrane Proteins on Cell Surface by AFM

The spatial distributions of specific membrane proteins can be mapped by AFM force volume method [5]. For this method, arrays of (e.g., 16×16) force curves are recorded in the local areas (e.g., 1×1 µm) on cell surface with functionalized tip. Each force curve corresponds the molecular interactions of a particular point on the cell surface. If no receptor-ligand specific binding occurs in this point, then there is

no specific unbinding peak in the force curve. In this case, the unbinding force is zero. If receptor-ligand specific binding occurs in this point, then specific unbinding peak appears in the force curve. In this case, the unbinding force is equal to the magnitude of the specific peak. After normalizing these force values into 0–255, the gray maps are constructed. Force volume method has been used to investigate the nanoscale distributions of specific membrane proteins on microbial cells [5–7] and mammalian cells [8–10]. The disadvantage of force volume method is that it is time-consuming (recording a map often requires more than ten minutes) with low efficiency.

In 2005, Ebner et al. [11] presented a method to simultaneously obtain the topography image and recognition image on cell surface with functionalized tip, and this technique is called simultaneous topography and recognition (TREC) imaging. When a ligand on the AFM tip binds to a receptor on the cell surface, the vibrating cantilever cannot return to its original position due to the pulling between AFM tip and the receptor-ligand pair, which causes the changes of the upper half of the cantilever's oscillation signal but the lower half of the oscillation signal is not influenced. By separating the oscillation signal into the upper part and the lower part with a special electronic circuit, the recognition image and topography image can be simultaneously obtained [12, 13]. TREC has achieved great success in mapping the proteins attached on mica [14, 15] and has been applied to map the membrane proteins on cell surface [16, 17]. TREC has been integrated to commercial AFM. However, TREC requires a relative low Q factor of the AFM probe (~1 in liquids [18]) and thus has limited detection precision. Besides, force curves are not recorded in TREC imaging, and thus quantitative force information about molecular interactions is lacking.

5.2 Peak Force Tapping AFM

In recent years, a new AFM imaging mode, which is called peak force tapping (PFT) [19, 20], appears as a powerful method to simultaneously obtain multiple parameters (e.g., topography, elasticity, adhesion, deformation and energy dissipation) of biological samples. In the PFT mode, the vibrating tip indents the samples to record an array of force curves for each sampling points on the specimens. By real-time analyzing the different parts of the force curves (Fig. 5.1a), multiple parameters that reflect the physical properties of the samples are obtained. The Young's modulus and adhesion force are obtained from the retract curve. The deformation is obtained from the approach curve. The energy dissipation is equal to the area between the approach curve and the retract curve. We know that conventional tapping mode reduces the influence of lateral force on the sample, but the vibrating frequency of cantilever in conventional tapping mode is near the resonant frequency of the cantilever, which results in the relative large tapping force on the sample and may cause damage to fragile samples (e.g., living cells). In PFT, the vibrating frequency of the cantilever is much less than its resonant frequency (e.g., the vibrating frequency of cantilever in PFT in water is less than 2 kHz [1], while the resonant frequency of the cantilever in water is often larger than 10 kHz [21]). Hence, compared with normal tapping mode, PFT

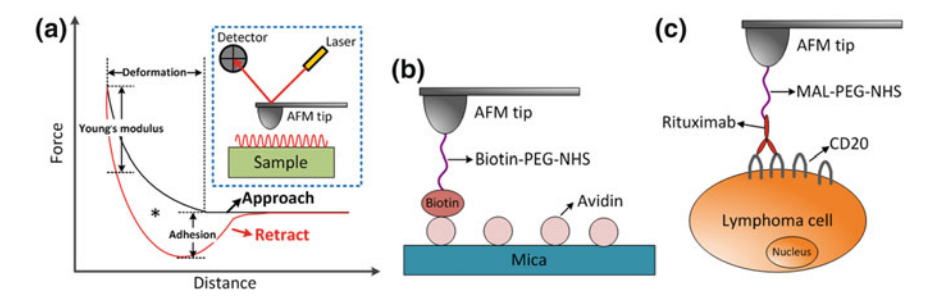


Fig. 5.1 Principle of recognizing proteins using PFT imaging with functionalized tips [2]. **a** Schematic diagram of a force curve which includes an approach curve and a retract curve. PFT imaging extracts different properties of samples by analyzing the different parts of the force curve. The Young's modulus and adhesion force are obtained from the retract curve. The deformation is obtained from the approach curve. The energy dissipation is equal to the area between the approach curve and the retract curve (denoted by the asterisk). The inset is the schematic diagram of PFT imaging. The tip intermittently contacts the sample to obtain an array of force curves for each sampling point. **b** Probing the avidins adsorbed on mica by linking biotins to the AFM tip. **c** Probing the CD20s on the surface of lymphoma cell by linking rituximabs to the AFM tip

further decreases the tapping force between AFM tip and sample, which is of active significance for probing living biological samples. By PFT imaging, the structural information of single native membrane proteins can be correlated to the mechanical properties [22], chemical properties [23], and electrostatic properties [24] of the proteins, providing novel insights into the behaviors of single molecules.

Since its advent, researchers have applied PFT imaging to investigate the physicochemical properties of different biological samples, e.g., membrane proteins (bacteriorhodopsin on the purple membrane of bacterial [22], erythrocyte membrane [25]) and living cells (keratinocyte [19], yeast [7], *E. coli* bacteria [26]). However, these researches were commonly performed with the use of ordinary tips [19, 22, 25] that cannot identify the specific membrane proteins on the cell surface. In recent studies, researchers [7, 26] have applied PFT imaging to investigate the specific molecular interactions on bacterial cells using functionalized tips. Nevertheless, studies that demonstrate the accuracy and reliability of the specific molecular interactions detected by PFT with functionalized tips are still needed. Besides, to our knowledge, studies that applying PFT imaging to investigate the specific membrane proteins on human cancerous cells have not been reported.

5.3 Mapping Protein Distributions by PFT

PFT mode was used to map the specific proteins attached on mica and membrane proteins on lymphoma cell surface with functionalized tips, as shown in Fig. 5.1b, c. Avidins coated on mica were sensed by biotin-tethered tip, whereas CD20s on lymphoma cell surface were sensed by rituximab-tethered tip.

5.3.1 Avidins on Mica

Avidins were attached onto mica surface according to the protocol in the reference [27]. Avidin powder (Solarbio Company, Beijing, China) was dissolved in 0.1 M phosphate buffered saline (PBS) to a stock concentration of 1 mg/mL. Then the stock solution was diluted with 100 mM NaCl to a final concentration of 1 μg/mL. Next, a freshly cleaved mica was immersed in this solution for 20 min and subsequently rinsed by PBS for three times. The avidin-coated mica was glued to a glass slide which was placed in a Petri dish containing PBS for AFM experiments. Biotins were linked to the surface of AFM tips by two steps: (1) Coat the AFM tip with a layer of NH₂ via APTES and *N*,*N*-diisopropylethylamin using a vapor deposition method under argon gas in a glass desiccators for 2 h; (2) Immerse the NH₂-modified tip in the mixture of biotin-PEG-NHS (JenKem Company, Beijing, China), triethylamine and chloroform for 2–3 h. The procedure of linking rituximabs to the surface of AFM tips was the same described in Chap. 4.

PFT imaging was performed using a Bioscope Catalyst AFM (Bruker, Santa Barbara, CA, USA) which was set on an inverted microscope (Ti, Nikon, Japan). The experiments were carried out in PBS at room temperature. Before imaging, the spring constant of the cantilever was calibrated. Under the guidance of optical microscopy, the functionalized tips were moved to the sample (avidin-coated mica, Raji cell) to perform imaging. Images were recorded at 256×256 pixels and the imaging rate was 0.5-1 Hz. Since mica surface is flat and cell surface is rough, the peak force amplitude was 100 nm for avidin-coated mica and 1000 nm for Raji cell. In order to verify the specific molecular interactions of the recognition spots from the obtained adhesion images, control experiments were performed, including obtaining force curve on recognition spots, imaging with ordinary tips, obtaining adhesion images after adding free antibodies to block the CD20s, and imaging on normal cells.

Figure 5.2 shows the results of locating the individual avidins on mica surface via PFT imaging using biotin-tethered tips. Avidin-biotin is an idea system for single molecule recognition studies, because avidin can simply adsorb to mica and biotin-PEG linker is commercially available [11]. Hence we used the avidin-biotin system to test the reliability of applying PFT imaging to detect the specific molecular interactions. Figure 5.2a is a typical topography image and Fig. 5.2e is the corresponding adhesion image. We can see that the avidin particles are clearly identified in the topography image. The recognition spots are also discernible in the adhesion image (denoted by the green arrows in Fig. 5.2e). The recognition spots are notably consistent with the topography of avidins. In order to examine the reproducibility of the recognition results, two serial images of a same area on avidin-coated mica were obtained. Figure 5.2b, f are the first scan images and Fig. 5.2c, g are the second scan images of the same area. Due to the thermal drift, the images obtained during the second scan shifted slightly to the right. The recognition spots are denoted by the ellipses in Fig. 5.2f. We can see that the

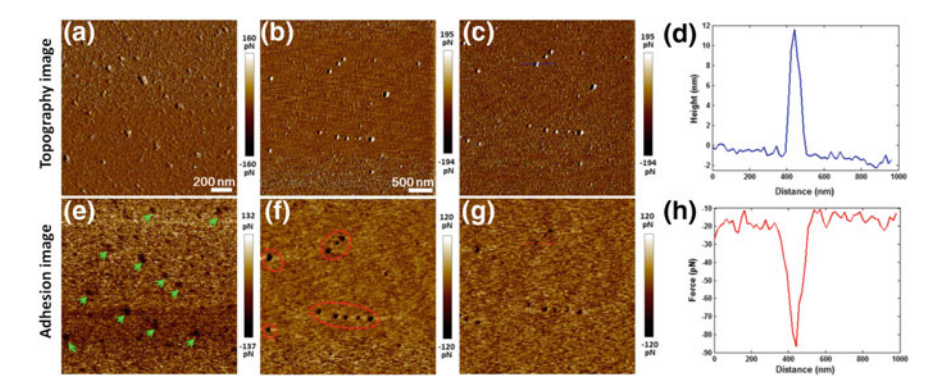


Fig. 5.2 Simultaneously obtaining the topography and adhesion image of avidins on mica by PFT imaging with biotin-tethered tips [2]. \mathbf{a} , \mathbf{e} are the topography image (\mathbf{a}) and the corresponding adhesion image (\mathbf{e}). \mathbf{b} , \mathbf{f} and \mathbf{c} , \mathbf{g} are the two scans of the same area on mica. Topography images (\mathbf{b} , \mathbf{c}) and the corresponding adhesion images (\mathbf{f} , \mathbf{g}). \mathbf{d} Section curve of topography image along the blue line in (\mathbf{c}). \mathbf{h} Section curve of adhesion image along the red line in (\mathbf{g})

recognition spots from the two scans are almost the same, indicating that the specific molecular recognitions were robust when scanning the proteins with biochemical sensitive tips at PFT mode. Figure 5.2d, h are the section curves obtained from topography image (Fig. 5.2c) and adhesion image (Fig. 5.2g) respectively. We can clearly see the abrupt peaks in the section curves. The peak in Fig. 5.2d is caused by the topography of avidins while the peak in Fig. 5.2h is caused by the specific interactions between avidins and biotins.

In order to examine whether the recognition spots were caused by the avidin-biotin specific interactions, force curves were obtained on the avidins. Figure 5.3c is a typical force curve obtained on the avidins in Fig. 5.3a, b (denoted by the white arrow). The inset in Fig. 5.3c is the enlarged view of the retract curve in the range of 900–950 nm. From the inset, we can clearly see that the retract curve has a specific unbinding peak which is caused by the stretching of PEG spacer. For contrast, the force curve obtained at the bare area on mica has no unbinding peaks (Fig. 5.3d). The results indicated that the recognition spots in the adhesion images were caused by the specific molecular interactions. We also performed PFT imaging on avidin-coated mica using nonfunctionalized tips (the tip surface did not have biotins) and the results are shown in Fig. 5.3e-h. The avidins are discernible in the topography image (Fig. 5.3e, f). However, from the corresponding adhesion images (Fig. 5.3g, h), we cannot see the recognition spots. This is because that no avidin-biotin interactions occur when using ordinary tips. The results (Fig. 5.3) confirmed that the recognition spots in the adhesion images (Fig. 5.2) corresponded to the avidins on mica, indicating that PFT imaging can specifically and reliably recognize the purified proteins attached on mica using functionalized tips.

The advantage of adsorbing proteins to mica is the high signal-to-noise ratio due to the atomically flat surface of mica, which facilitates us to exactly quantify the

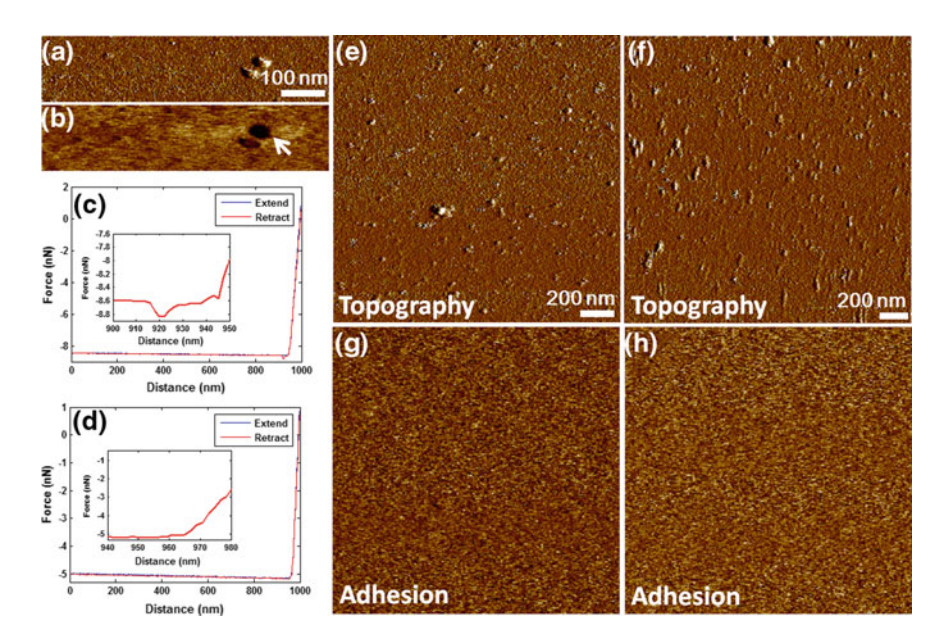


Fig. 5.3 Avidin-biotin specificity verification [2]. **a**, **b** are the topography image (**a**) and corresponding adhesion image (**b**). **c** A typical force curve with specific unbinding peak obtained on avidins [denoted by the arrow in (**b**)]. **d** A typical force curve obtained on the bare area of mica. The insets in (**c**, **d**) are the enlarged views of the retract curves. Topography images **e**, **f** and corresponding adhesion images **g**, **h** obtained using nonfunctionalized tips

protein-protein interactions [28]. In fact, since cell surface is highly complex (e.g., rough, soft, and dynamic), current AFM force spectroscopy experiments were commonly performed on purified proteins which were immobilized on substrate (e.g., mica) [29]. Traditional biochemical methods (e.g., surface plasmon resonance and radioimmunoassay [2]) for analyzing the affinity constants of proteins require a lot of purified proteins which are isolated from large number of cells, and thus is costly and time-consuming. By contrast, only a small amount of proteins are needed for PFT imaging and hence is with economical significance for assessing the molecular interactions. Compared with TREC mode, PFT mode can use probes with higher Q factors (the Q factor of PFT is larger than 5 while the Q factor of TREC is about 1 [20, 30]), meaning that PFT mode has better detection sensitivity. In addition, the driving frequency of TREC mode is near the resonance frequency of the probe [30], while the driving frequency of PFT is much less than the resonance frequency of the probe [13]. Hence the tapping force between AFM tip and sample of PFT mode is less than that of TREC. What's more, besides topography and adhesion, PFT mode can simultaneously acquire other parameters, such as mechanics [31] and electronics [24]. Consequently, PFT provides a powerful tool in life sciences for investigating cellular and molecular behaviors.

5.3.2 CD20s on Lymphoma Cell Surface

Raji cells were cultured in RPMI-1640 containing 10% fetal bovine serum at 37 °C (5% CO₂). After 24 h of culture, Raji cells were harvested at 1000 rpm for 5 min. Harvested Raji cells were dropped to a poly-L-lysine-coated glass slide and then fixed by 4% paraformaldehyde for 30 min. After being rinsed by PBS, the glass slide was placed in a Petri dish containing PBS. Normal human cells were prepared from the peripheral blood of healthy volunteers. The preparation process of normal cell sample was the same as the Raji cell sample.

Figure 5.4 shows the results of locating CD20s on human lymphoma Raji cells at PFT mode with the use of rituximab-tethered tips. Rituximab, an antibody against CD20s (CD20 is highly expressed on B-cell lymphomas), is approved by USFDA in 1997 to treat B-cell lymphomas [32]. The binding of rituximab to CD20 on lymphoma cell can result in the death of lymphoma cell. Figure 5.4a is a topography image of a local area on a Raji cell and Fig. 5.4e is the corresponding adhesion image. The topography image shows the rough cell surface. From the adhesion image, we can see that recognition spots (denoted by the green arrows) form nanodomains on the cell surface. In order to test the reproducibility of the recognition results, two serial scans of the same local area on a Raji cell (denoted by the square in Fig. 5.4b) were performed. Figure 5.4c, g are the first scan images and Fig. 5.4d, h are the second scan images. We can see the recognition spots in the adhesion images (denoted by the red ellipses in Fig. 5.4g) and these recognition spots are almost the same for the two scans, indicating that the recognition results were reproducible. In order to test whether the recognition spots were from the specific molecular interactions, force curves were obtained on the recognition spots.

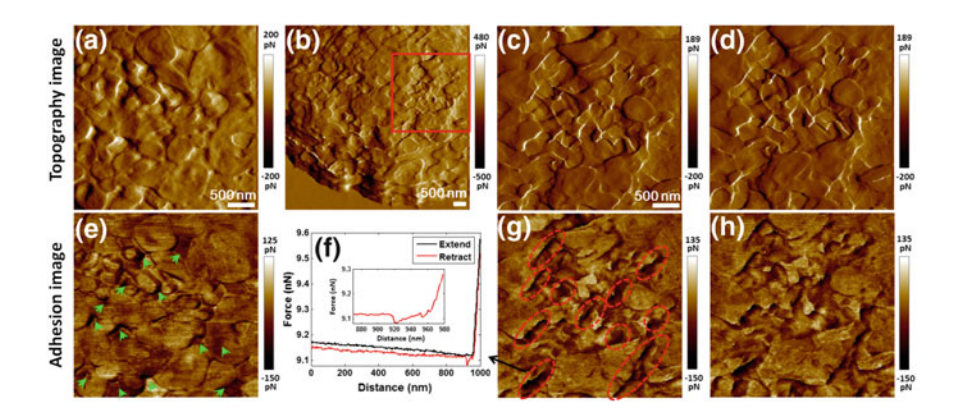


Fig. 5.4 Simultaneously obtaining the topography and adhesion images of CD20s [2]. **a**, **e** are the topography image (**a**) and the corresponding adhesion image (**e**). **b** Topography image of large scan. **f** A typical force curve obtained on the recognition area [denoted by the square in (**g**)]. The inset in **f** was the enlarged view of the retract curve in the range of 870–980 nm. **c**, **g** and **d**, **h** are the two scans of the same area on lymphoma cell. Topography images (**c**, **d**) and corresponding adhesion images (**g**, **h**)

Figure 5.4f is a typical force curve obtained on a recognition area (denoted by the black arrow in Fig. 5.4g). We can clearly see a specific unbinding peak in the retract curve (Fig. 5.4f), which confirms that the recognition spots were caused by specific molecular interactions.

In order to exactly demonstrate that the recognition spots were caused by CD20-rituximab interactions, we performed serial scanning at a same local area on a Raji cell after the addition of free rituximabs and the results are shown in Fig. 5.5. Figure 5.5a is the topography image obtained before the addition of rituximabs and Fig. 5.5e is the corresponding adhesion image. Some distinct recognition spots are denoted by red arrows. After the addition of rituximab, serial images were obtained on the same area. Figure 5.5b, c, d are topography images obtained at 30, 60, and 120 min respectively after the addition of rituximab and Fig. 5.5f, g, h are the corresponding adhesion images. We cannot see significant differences between the serial topography images. While from the adhesion images, we can see that the color of recognition spots became obviously weaker as time progressed. About 120 min after the addition of rituximab, the recognition spots basically vanished. However, there are still some recognition spots (denoted by the yellow arrows in Fig. 5.5h) in the adhesion image and this may because that the rituximabs were not enough to block all of the CD20s on the cell surface. The results confirmed that the recognition spots were caused by CD20-rituximab interactions.

For control, we also performed PFT imaging on normal blood cells which were prepared from healthy volunteers by rituximab-tethered tip, and the results are shown in Fig. 5.6. From the topography images (Fig. 5.6a, b), we can see the rough cell surface. From the adhesion image (Fig. 5.6c, d), however, we cannot see the

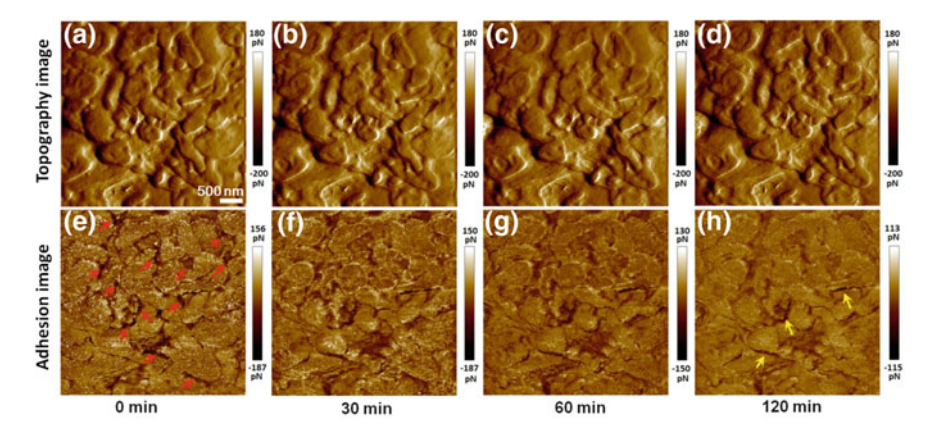


Fig. 5.5 CD20-rituximab specificity verification [2]. \mathbf{a} , \mathbf{e} are the topography image (\mathbf{a}) and the corresponding adhesion image (\mathbf{e}) obtained on a local area on a Raji cell. Recognition spots are denoted by red arrows. Then rituximab solution was added and serial images were obtained for the same area. (\mathbf{b} , \mathbf{f}), (\mathbf{c} , \mathbf{g}), (\mathbf{d} , \mathbf{h}) were obtained 30, 60, and 120 min after the addition of rituximab respectively

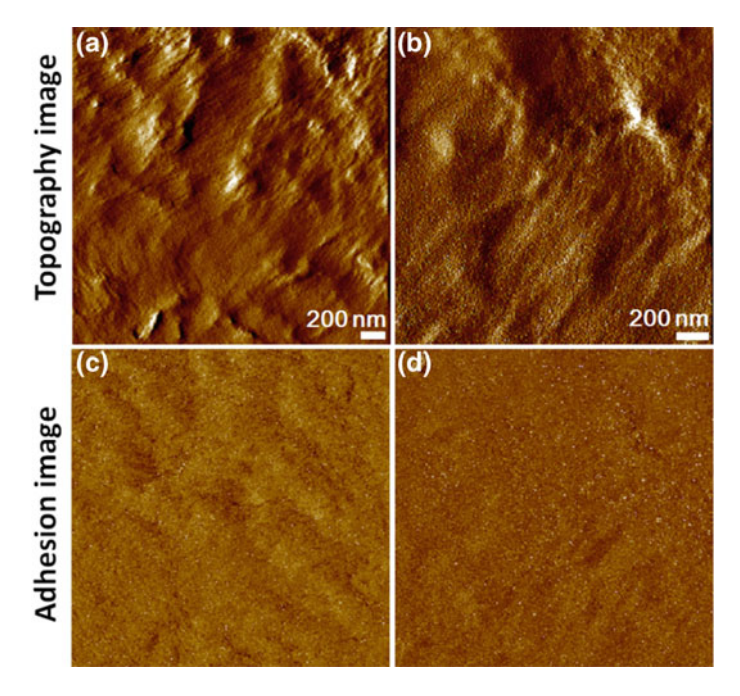


Fig. 5.6 Obtaining the topography and adhesion images on normal cells from the peripheral blood of healthy volunteers using rituximab-tethered tips [2]. **a**, **b** are topography images and **c**, **d** are the corresponding adhesion images

recognition spots. CD20s are also expressed on the surface normal B lymphocytes. But in the peripheral blood, B lymphocytes account for less than 1% (99% are erythrocytes). Hence it is reasonable that the detected cells in Fig. 5.6 were not B lymphocytes and thus there were no recognition spots. In previous studies, researchers have applied PFT imaging to correlate cellular topography with protein recognition information on microbial cells [7, 26]. Here, CD20s were visually recognized by PFT imaging using antibody-tethered tips and correlated with cellular topography, demonstrating the ability of AFM in visualizing specific membrane proteins on mammalian cells.

The above experiments were performed on chemically fixed cells. Imaging living Raji cells with PFT mode was also explored, but we found that it was difficult to image living Raji cells. For imaging the local areas of cells, the real-time force curves exhibited abnormal shapes (Fig. 5.7) which were quite different from the standard force curves obtained on living cells (Fig. 3.5). PFT has been used to image living microbial cells [6, 26] and living mammalian adherent cells (e.g., keratinocytes [19], MDCK cells [33]), but to our knowledge so far imaging living mammalian suspended cells with PFT has not been reported. This may due to the soft and suspended characteristics of the cells. Imaging living mammalian suspended cells is an issue needing to be addressed for the applications of PFT mode.

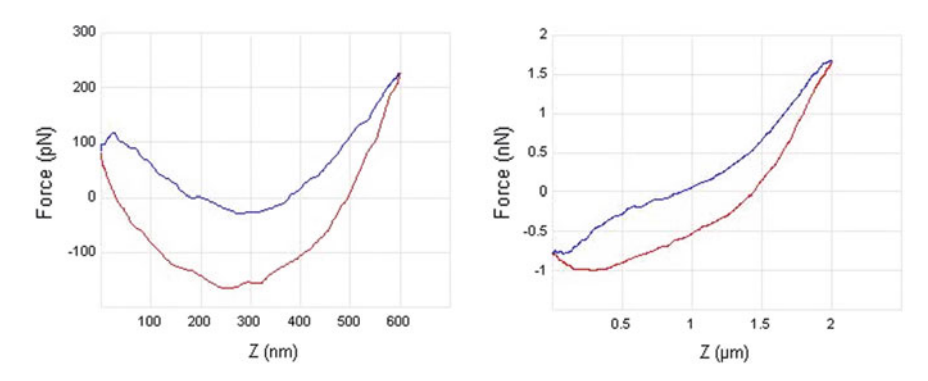


Fig. 5.7 Typical real-time PFT force curves on living Raji cells. The blue line corresponds to the extend curve. The red line corresponds to the retract curve

Figure 5.8 shows the quantitative analysis of the cluster sizes of CD20s on Raji cells. From the recognition images, we can quantitatively analyze the distributions of CD20s on Raji cells. The cluster analysis was performed using the open source Fiji software according to the reference [18]. The adhesion images were first converted into binary images. Then the relation between pixel distance and spatial distance was calibrated. The binary images were treated by Particle Analysis to get the sizes of each recognition areas. Figure 5.8a is an overlay of topography image and recognition image, correlating the CD20 distribution with cellular topography. Figure 5.8b, c are the original adhesion images of two recognition areas. Figure 5.8d is another overly image. We can see that the recognition spots distributed irregularly on the cell surface and the sizes of recognition spots were variable. CD20 is usually expressed at high levels on B lymphoma cells [34], allowing dense accumulation of the anti-CD20 antibodies (e.g., rituximab) on cell membrane. The high levels of CD20s on the cell membrane caused that we could clearly see many CD20 spots in the recognition images. Besides, studies have shown that CD20s on the cell membrane are not expressed in monomeric form but organized into heterogeneous supramolecular complexes which associate various molecules, including CD20 dimers or tetramers, C-terminal src kinase-binding protein, CD40, the MHC II protein and B-cell antigen receptor [35, 36]. The heterogeneity of CD20-related cluster areas caused that the recognition spots had different sizes. By analyzing the size of each recognition spots in the recognition image, we can obtain the histogram of cluster sizes of recognition spots. Figure 5.8e is the cluster size histogram of recognition spots in Fig. 5.8a, f is the cluster size histogram of recognition spots in Fig. 5.8d. From Fig. 5.8e, f we can see that CD20 organizations are mainly distributed in the range of 100–4000 nm². PFT imaging can directly show the correlation between protein distribution and cell topography, which is inaccessible by traditional methods (such as fluorescence labeling [37]), thus providing a novel way to investigate the nanoscale behaviors of biomolecules on the cell surface.

5.4 Summary 75

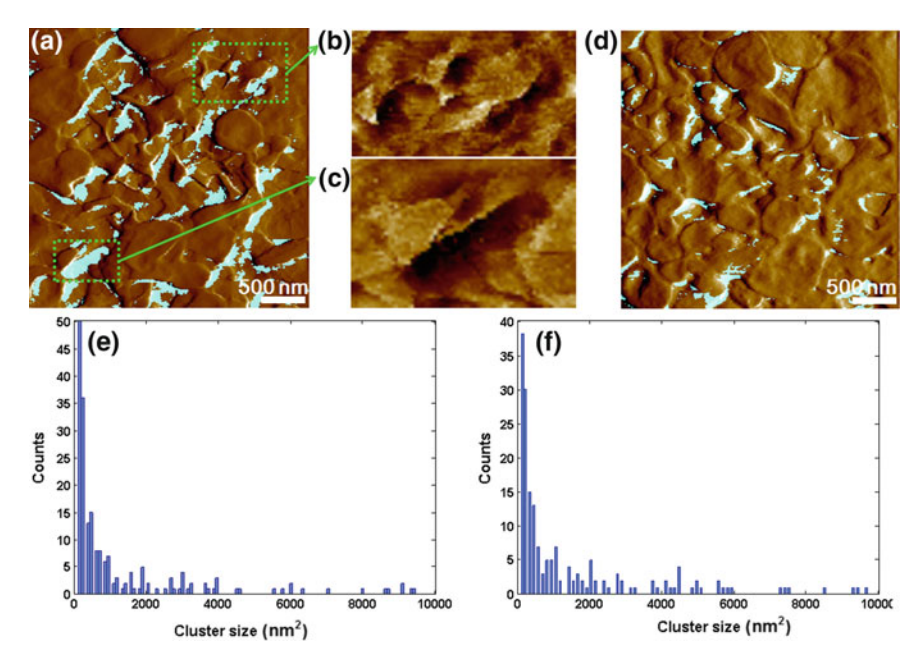


Fig. 5.8 Location of the CD20s on the lymphoma Raji cell surface [2]. **a** Overlay of recognition image (in cyan) of CD20 and the corresponding topography image. **b**, **c** Adhesion images of the examples of typical recognition spots in (**a**). **d** Another overly of recognition image and topography image. **e** The distribution of recognition spot size in (**a**). **f** The distribution of recognition spot size in (**d**)

5.4 Summary

A challenging issue in current cell and molecular biology is to understand how the various biomolecules on the cell surface interact with each other to fulfill the physiological functions [38]. With the use of functionalized tip, purified avidins on mica and native CD20s on lymphoma cell surface were recognized and correlated with topography information at AFM PFT mode. Specific molecular interaction events were remarkably visible from the adhesion images. The reproducibility of molecular recognition results was confirmed by serial scanning, while the specificity of the molecular recognition results was confirmed by control and blocking experiments, demonstrating the capability of PFT mode in mapping membrane proteins on the surface of mammalian cells, which will be of active significance for investigating molecular interactions in their native states.

References

- Pfreundschuh M, Martinez-Martin D, Mulvihill E et al (2014) Multiparametric high-resolution imaging of native proteins by force-distance curve-based AFM. Nat Protoc 9:1113–1130
- Li M, Xiao X, Liu L et al (2016) Rapid recognition and functional analysis of membrane proteins on human cancer cells using atomic force microscopy. J Immunol Methods 436: 41–49
- 3. Robertson JW, Kasianowicz JJ, Banerjee S (2012) Analytical approaches for studying transporters, channels and porins. Chem Rev 112:6227–6249
- Phillips R, Ursell T, Wiggins P et al (2009) Emerging roles for lipids in shaping membrane-protein function. Nature 459:379–385
- Dupres V, Menozzi FD, Locht C et al (2005) Nanoscale mapping and functional analysis of individual adhesions on living bacteria. Nat Methods 2:515–520
- Alsteens D, Garcia MC, Lipke PN et al (2010) Force-induced formation and propagation of adhesion nanodomains in living fungal cells. Proc Natl Acad Sci USA 107:20744–20749
- Alsteens D, Dupres V, Yunus S et al (2012) High-resolution imaging of chemical and biological sites on living cells using peak force tapping atomic force microscopy. Langmuir 28:16738–16744
- Hu M, Chen J, Wang J et al (2009) AFM- and NSOM-based force spectroscopy and distribution analysis of CD69 molecules on human CD4⁺ T cell membrane. J Mol Recogn 22:516–520
- Soumetz FC, Saenz JF, Pastorino L et al (2010) Investigating of integrain expression on the surface of osteoblast-like cells by atomic force microscopy. Ultramicroscopy 110:330–338
- Lama G, Papi M, Angelucci C et al (2013) Leuprorelin acetate long-lasting effects on GnRH receptors of prostate cancer cells: an atomic force microscopy study of agonist/receptor interaction. PLoS ONE 8:e52530
- Ebner A, Kienberger F, Kada G et al (2005) Localization of single avidin-biotin interactions using simultaneous topography and molecular recognition imaging. ChemPhysChem 6: 897–900
- 12. Senapati S, Lindsay S (2016) Recent progress in molecular recognition imaging using atomic force microscopy. Acc Chem Res 49:503–510
- 13. Li M, Dang D, Liu L et al (2017) Imaging and force recognition of single molecular behaviors using atomic force microscopy. Sensors 17:200
- Wang H, Obenauer-Kutner L, Lin M et al (2008) Imaging glycosylation. J Am Chem Soc 130:8154–8155
- 15. Preiner J, Losilla NS, Ebner A et al (2009) Imaging and detection of single molecule recognition events on organic semiconductor surfaces. Nano Lett 9:571–575
- Chtcheglova LA, Atalar F, Ozbek U et al (2008) Localization of the ergtoxin-1 receptors on the voltage sensing domain of hERG K⁺ channel by AFM recognition imaging. Pflugers Arch Eur J Physiol 456:247–254
- 17. Duman M, Pfleger M, Zhu R et al (2010) Improved localization of cellular membrane receptors using combined fluorescence microscopy and simultaneous topography and recognition imaging. Nanotechnology 21:115504
- 18. Zhang J, Chtcheglova LA, Zhu R et al (2014) Nanoscale organization of human GnRH-R on human bladder cancer cells. Anal Chem 86:2458–2464
- Heu C, Berquand A, Elie-Caille C et al (2012) Glyphosate-induced stiffening of HaCaT keratinocytes, a peak force tapping study on living cells. J Struct Biol 178:1–7
- Dufrene YF, Martinez-Martin D, Medalsy I et al (2013) Multiparametric imaging of biological systems by force-distance curve-based AFM. Nat Methods 10:847–854
- Li M, Liu L, Xi N et al (2011) Imaging and measuring the rituximab-induced changes of mechanical properties in B-lymphoma cells using atomic force microscopy. Biochem Biophys Res Commun 404:689–694

References 77

22. Rico F, Su C, Scheuring S (2011) Mechanical mapping of single membrane proteins at submolecular resolution. Nano Lett 11:3983–3986

- Medalsy I, Hensen U, Muller DJ (2011) Imaging and quantifying chemical and physical properties of native proteins at molecular resolution by force-volume AFM. Angew Chem Int Ed 50:12103–12108
- Pfreundschuh M, Hensen U, Muller DJ (2013) Quantitative imaging of the electrostatic field and potential generated by a transmembrane protein pore at subnanometer resolution. Nano Lett 13:5585–5593
- Picas L, Rico F, Deforet M et al (2013) Structure and mechanical heterogeneity of the erythrocyte membrane reveals hallmarks of membrane stability. ACS Nano 7:1054–1063
- 26. Alsteens D, Trabelsi H, Soumillion P et al (2013) Multiparametric atomic force microscopy imaging of single bacteriophages extruding from living bacteria. Nat Commun 4:2926
- 27. Riener CK, Stroh CM, Ebner A et al (2003) Simple test system for single molecule recognition force microscopy. Anal Chim Acta 479:59–75
- Muller DJ, Engel A (2007) Atomic force microscopy and spectroscopy of native membrane proteins. Nat Protoc 2:2191–2197
- Dufrene YF, Evans E, Engel A et al (2011) Five challenges to bringing single-molecule force spectroscopy into living cells. Nat Methods 8:123–127
- 30. Ctroh CM, Ebner A, Geretschlager M et al (2004) Simultaneous topography and recognition imaging using force microscopy. Biophys J 87:1981–1990
- 31. Dukukin ME, Sokolov I (2012) Quantitative mapping of the elastic modulus of soft materials with HarmoniX and PeakForce QNM. Langmuir 28:16060–16071
- 32. Maloney DG (2012) Anti-CD20 antibody therapy for B-cell lymphomas. N Engl J Med 366:2008–2016
- 33. Schillers H, Medalsy I, Hu S et al (2016) Peakforce tapping resolves individual microvilli on living cells. J Mol Recogn 29:95–101
- 34. Glennie MJ, French RR, Cragg MS et al (2007) Mechanisms of killing by anti-CD20 monoclonal antibodies. Mol Immunol 44:3823–3837
- 35. Cartron G, Watier H, Golay J et al (2004) From the bench to the bedside: ways to improve rituximab efficacy. Blood 104:2635–2642
- 36. Polyak MJ, Li H, Shariat N et al (2008) CD20 homo-oligomers physically associate with the B cell antigen receptor. J Biol Chem 283:18545–18552
- 37. Huh YO, Keating MJ, Saffer HL et al (2001) Higher levels of surface CD20 expression on circulating lymphocytes compared with bone marrow and lymph nodes in B-cell chronic lymphocytic leukemia. Am J Clin Pathol 116:437–443
- 38. Muller DJ, Helenius J, Alsteens D et al (2009) Force probing surfaces of living cells to molecular resolution. Nat Chem Biol 5:383–390

Chapter 6 Applications of AFM Cellular and Molecular Biophysical Detection in Clinical Lymphoma Rituximab Treatment

In Chaps. 2–5, series methods based on AFM have been established to detect the biophysical properties (morphology, mechanics, molecular binding affinity, membrane protein distribution) of cells. In this chapter, these methods are applied to systematically investigate the three killing mechanisms in lymphoma rituximab treatment (as shown in Fig. 1.1) and the clinical significance of AFM single-cell and single-molecule biophysical detection is explored by performing tests on primary cells prepared from lymphoma patients.

6.1 Cellular Ultra-Microstructure and Mechanics Detection

6.1.1 PCD Mechanism

During PCD, the binding of rituximab to CD20 on lymphoma cell can result in the apoptosis of cell. AO/EB fluorescence staining was used to examine the PCD effects of rituximab on lymphoma Raji cells. Raji cells were resuspended and then plated in 24-well microtiter plates. After incubating at 37 °C (5%CO₂) for 24 h with rituximab, cells were harvested and dropped onto the glass slide. The AO/EB staining solution was then dropped onto the glass slide and incubated for 2 min. Next, the cell sample was observed by fluorescence microscope. For control, Raji cells which were cultured without rituximab were stained by AO/EB. Figure 6.1 shows the experimental results of AO/EB staining. Figure 6.1a is from the Raji cells cultured with rituximab and Fig. 6.1b is from the Raji cells cultured without rituximab. From Fig. 6.1a, we can see the distinct apoptosis of Raji cells, as the appearance of nuclear pyknosis and condensed chromatin at the periphery of the nuclear envelope. From the control group, the apoptosis was not observed. The results confirmed that the stimulation of rituximab can induce the apoptosis of Raji cells.

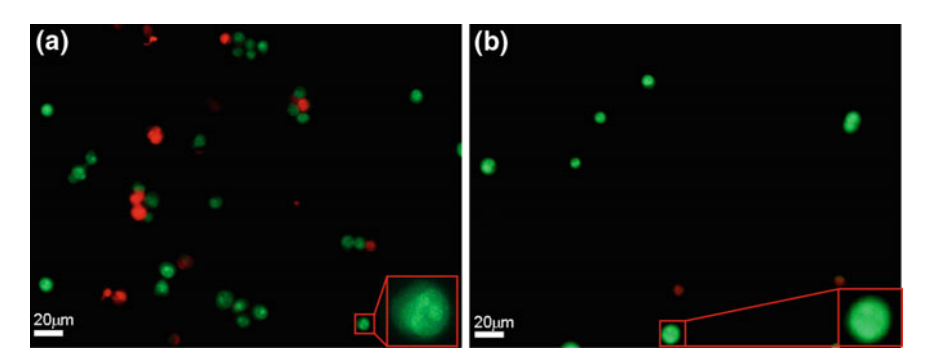


Fig. 6.1 AO/EB staining of Raji cells [1]. **a** Treated by 10 μg/ml rituximab for 24 h. **b** Control group (without rituximab)

Based on micropillar immobilization, the morphological and mechanical changes of Raji cells after the stimulation of rituximab were then observed by AFM. For AFM experiments, harvested living Raji cells were dropped onto the poly-Llysine-coated pillar array. AFM images and force curves were recorded on trapped living Raji cells. After the stimulation of rituximab, AFM images and force curves were recorded again on the same cells. Figure 6.2 shows the AFM images of the topography changes of a trapped B lymphoma cell before and after stimulation with 0.2 mg/mL rituximab. Figure 6.2a-c show the topography image, amplitude image, and three-dimensional topography image of the trapped cell before rituximab stimulation, respectively. The scan size was 40 µm. Because the substrate was coated with positively charged poly-L-lysine, the negatively charged cells readily attached onto it. In addition, pillars surrounding each cell helped it to resist the lateral forces exerted by the probe during scanning, thus avoiding displacement of the cell. Figure 6.2d, e are the topography image and amplitude image of a local area on the cell surface. The scan size was 3 µm. We can see that the topography is a little corrugated. Following incubation in rituximab, topography images and amplitude images of the same local area were re-acquired, as shown in Fig. 6.2f, g. We can see that the topography becomes more corrugated (denoted by the arrows in Fig. 6.2g).

Figure 6.3 shows the AFM images of the topography of a trapped B lymphoma cell before and after stimulation with 0.5 mg/mL rituximab. Figure 6.3a–c are the 40 μm topography image, amplitude image, and three-dimensional topography image of the trapped cell before stimulation, respectively. Figure 6.3d, e are the topography image and amplitude image of the local area of the cell surface before stimulation, and Fig. 6.3f, g are the topography image and amplitude image of the same local area after stimulation. We can see that the topography becomes notably more corrugated after stimulation and some tubercles appear (denoted by the arrows in Fig. 6.3g). Comparing these topography changes with those of the cell stimulated with 0.2 mg/mL rituximab, we can see that the 0.5 mg/mL rituximab-induced changes are more significant.

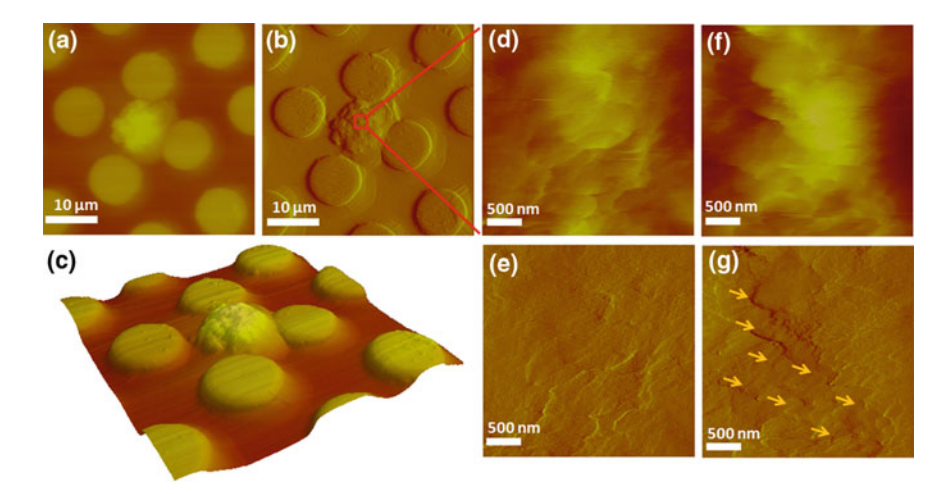


Fig. 6.2 AFM images of the topography changes of a trapped B lymphoma cell stimulated with 0.2 mg/mL rituximab [2]. **a** Topography image, **b** amplitude image, and **c** three-dimentional image of a cell. **d** Topography image and **e** amplitude image of a local area before rituximab stimulation. **f** Topography image and **g** amplitude image of the same local area after rituximab stimulation

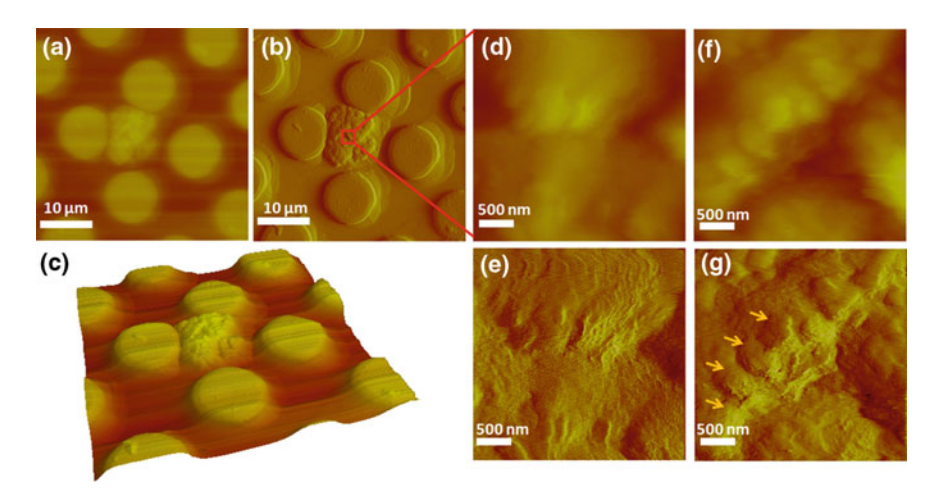


Fig. 6.3 AFM image of the topography changes of a trapped B lymphoma cell stimulated with 0.5 mg/mL rituximab [2]. **a** Topography image, **b** amplitude image, and **c** three-dimentional image of a cell. **d** Topography image and **e** amplitude image of a local area before rituximab stimulation. **f** Topography image and **g** amplitude image of the same local area after Rituximab stimulation

Figure 6.4 shows the Young's modulus changes of Raji cells after the stimulation of rituximab. After the stimulation of 0.2 mg/mL rituximab, the Young's modulus of lymphoma cell decreased from 196 to 183 kPa. After the stimulation of 0.5 mg/mL rituximab, the Young's modulus of lymphoma cell decreased from 234

to 175 kPa, showing that rituximab could induce the softening of lymphoma cells. For control, the Young's modulus of lymphoma cells stimulated by 0.5 mg/mL human IgG were measured and the results showed that the Young's modulus of lymphoma cells kept unchanged. Human IgG has no biological effects on lymphoma cells and hence the stimulation of human IgG does not cause the changes of cellular mechanical properties.

From Figs. 6.2, 6.3, 6.4, we can clearly see that the stimulation of rituximab resulted in the rougher cell surface and softer cell mechanics. In addition, these changes (cellular ultra-microstructures, Young's modulus) were dependent on the concentration of rituximab. The binding of rituximab to CD20s on lymphoma cell activates a series of molecular signal transduction (e.g., the downregulation of p38 MAPK, NF-kB, ERK1/2, and Bcl-2) [1-3], which finally leads to the apoptosis of the cell, as confirmed in Fig. 6.1. The activation of apoptosis can be accompanied by structural changes, which may result in the morphological and mechanical changes. Hu et al. [4] have used AFM to measure the Young's modulus of single resting, activated and apoptotic lymphocytes, showing that the apoptotic lymphocyte was significantly softer than the other two types. Cai et al. [5] investigated the changes of human pterygium fibroblasts after apoptosis, also showing that aoptosis cells were softer than normal cells. Here we can see that stimulation by rituximab leads to softer lymphoma cells, consistent with these results. At the higher rituximab concentration, more rituximabs bind to the CD20s, which may enhance the rituximab's effect to the cell and then results in more distinct changes to the morphology and Young's modulus. Collectively, the experimental results improve our understanding of rituximab's PCD mechanism at the single-cell level.

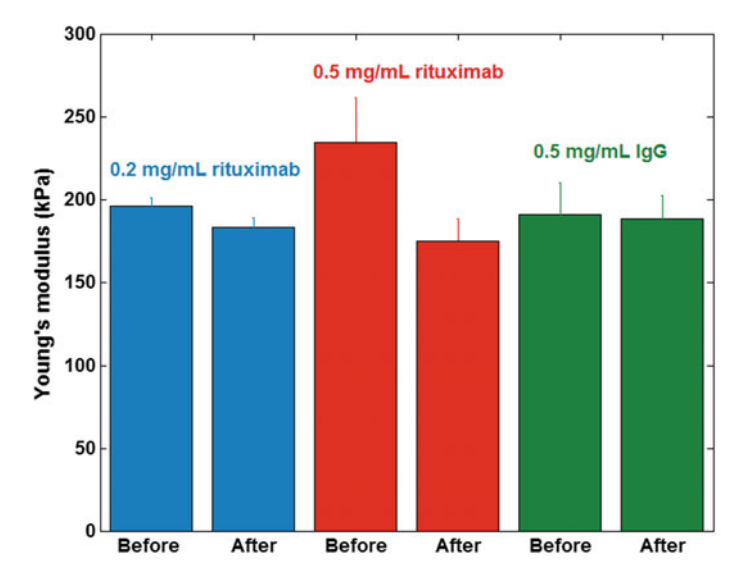


Fig. 6.4 Young's modulus changes of Raji cells after the stimulation of rituximab [3]

6.1.2 ADCC Mechanism

During macrophage-related ADCC mechanism, the F_{ab} portion of rituximab binds to CD20 of lymphoma cell and the Fc portion of rituximab binds to the Fc receptor of macrophage, which recruits macrophages to phagocytize the lymphoma cell [6]. Optical microscopy was used to observe the dynamics of rituximab-induced macrophage phagocytosis against lymphoma Raji cells, as shown in Fig. 6.5. Figure 6.5a, b are the optical images of Raji cells and macrophages after coincubation. Raji cells were coated by rituximabs and then incubated with RAW 264.7 cells (a macrophage cell line, purchased from the Cell Bank of the Chinese Academy of Sciences, Shanghai, China). We can discriminate cancerous cells (denoted by the black arrows) and macrophages (denoted by the red arrows) in the optical images according to the cell morphology. Macrophage is a type of adherent cell and the lamellipodium was clearly discernible. Lymphoma cell is a type of mammalian suspended cell and exhibited a round shape. When the co-incubation time was 10 min, the phagocytosis phenomenon was not clear (Fig. 6.5a). When the co-incubation time increased to 3 h, we can distinctly observe the macrophage phagocytosis from the optical images (Fig. 6.5b). There were three Raji cells in Fig. 6.5b and we can see one Raji cell (denoted by the II black arrow) was engulfed by the macrophage.

Fluorescence was used to exactly recognize Raji cells and macrophages. Carboxyfluorescein succinimidyl ester (CFSE) is a commonly used living cell fluorescence dye [7] and cells still have biological activities after CFSE staining. Hence we used CFSE for cell recognition. The working concentration of CFSE was following the supplier recommendations. CFSE staining was examined on Raji cells, and the results are shown in Fig. 6.5c, d. CFSE-stained Raji cells were

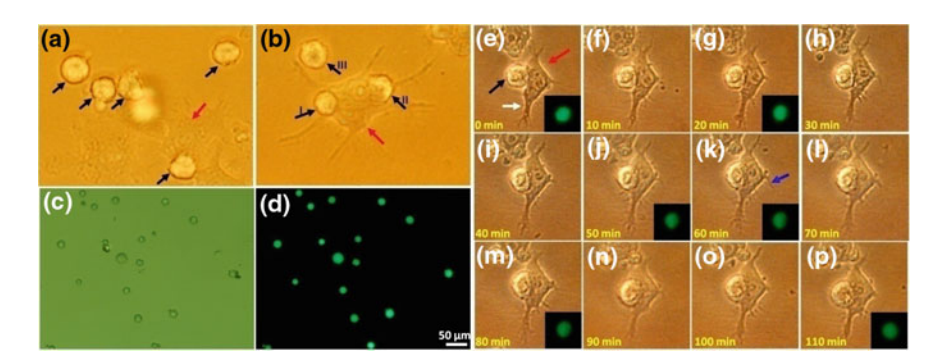


Fig. 6.5 Optical images of rituximab-mediated macrophage phagocytosis against lymphoma cells [19]. a 10 min and b 3 h after co-incubation of macrophages and Raji cells. The black arrows indicate cancer cells, and the red arrows indicate macrophages. c, d CFSE staining of Raji cells. c Optical bright field image and d corresponding fluorescent image. e-p Serial optical images of the dynamic process of macrophage phagocytosis against Raji cells. The insets are the corresponding fluorescent images of the Raji cell. Black arrow denotes cancer cell and red arrow denotes macrophage

dropped onto the glass slide (coated by a layer of poly-L-lysine for adsorbing cells to the glass slide) and fluorescence images were recorded. Figure 6.5c is the optical bright field images of Raji cells and Fig. 6.5d is the corresponding fluorescence images. We can see that all of the Raji cells exhibited uniform green fluorescence, confirming the efficiency of CFSE in staining Raji cells.

Then we used the established staining procedure to specifically recognize Raji cells in the process of macrophage phagocytosis. After coating the CFSE-stained Raji cells with rituximabs, Raji cells were incubated with macrophages. Both optical bright field image and fluorescence image were captured. Figure 6.5e-p shows the dynamic changes of macrophage phagocytosis against Raji cells in 2 h. The images were recorded every 10 min. The insets were the corresponding fluorescence images of cancerous cell. At the beginning (0 min), the boundary between cancerous cell and macrophage was apparent and the fluorescence intensity of the cancerous cell was uniform. Then the macrophage began to deform and engulf the cancerous cell. After 60 min, we can clearly see that a small proportion of the cancerous cell had been swallowed into the macrophage (Fig. 6.5k). We can see that the fluorescence intensity in Fig. 6.5k was non-uniform. This is because that the macrophage coated some part of the cancerous cell and this influenced the fluorescence intensity of the cancerous cell. After 90 min, an interesting phenomenon occurred. The macrophage did not continue to swallow but released the cancerous cell out (Fig. 6.5n-p). The fluorescence intensity in Fig. 6.5p was uniform again and this is because that the cancerous cell had been released from the macrophage. During the phagocytosis process, we can see the remarkable reorganization of cell lamellipodia (denoted by the white arrows in Fig. 6.5e) and filopodia (denoted by the blue arrow in Fig. 6.5k). This is because that phagocytosis is a complex process that is driven by a finely controlled rearrangement of the actin cytoskeleton [8]. The rearrangement of actin cytoskeleton caused the deformation and morphological changes of the macrophages. From Fig. 6.5e-p, we can see that the macrophage engulfed the cancerous cell at the first 90 min, but finally released the cancerous cell. Studies have shown that after 30-60 min co-incubation at 37 °C (5%CO₂), the antibody-dependent Fc receptor-mediated macrophage phagocytosis against cancerous cells could be successfully observed [9, 10]. The experiments here were done under room temperature at atmospheric environment, which may influence the physiological activities of the macrophages. In order to provide better conditions for cellular activities, temperature-controlled stage can be useful.

We then used AFM to image the nanoscale cellular morphological changes during the macrophage phagocytosis, and the results are shown in Fig. 6.6. After co-incubating the cancerous cells and macrophages for 3 h, the cells were chemically fixed and then imaged by AFM under the guidance of fluorescence microscopy. Figure 6.6a—e shows the cellular morphologies at the initial contact step between cancerous cell and macrophage. From the overlay of optical image and fluorescence image (Fig. 6.6a), we can clearly discern the cancerous cell by the fluorescence. Figure 6.6b, c are the AFM height image and corresponding deflection image of the two cells respectively. Figure 6.6d, e are the AFM height image

and corresponding deflection image of the contact area (denoted by the red square in Fig. 6.6c) respectively. From the optical image, we can not see the detailed situation about the contact area between the two cells. While the AFM images clearly showed that the cancerous cell docked on the macrophage and the engulfing of macrophage did not occur. Figure 6.6f-j shows the cellular morphologies at the beginning of engulfing. Figure 6.6f is the overlay image. The cancerous cell was identified by the fluorescence. Figure 6.6g, h are the AFM height image and corresponding deflection image respectively. Figure 6.6i, j are the local area AFM images (denoted by the red square in Fig. 6.6h) respectively. In this case, we can distinctly see that the macrophage was opening its mouth to engulf the cancerous cell (denoted by the white arrow in Fig. 6.6i). Figure 6.6k-p shows the cellular morphologies at the step during which macrophage had engulfed some proportions of the cancerous cell. From the optical image (Fig. 6.6k), we did not know whether the cancerous cell had been engulfed by the macrophage. While from the AFM images (Fig. 6.6o, p), we can clearly see that some proportions of the cancerous cell had been engulfed by macrophage. The results of Fig. 6.6 showed that AFM can reveal detailed situations at the nanoscale which were not be accessible by optical microscopy, thus providing novel knowledge which can help us to better understand the cell behaviors.

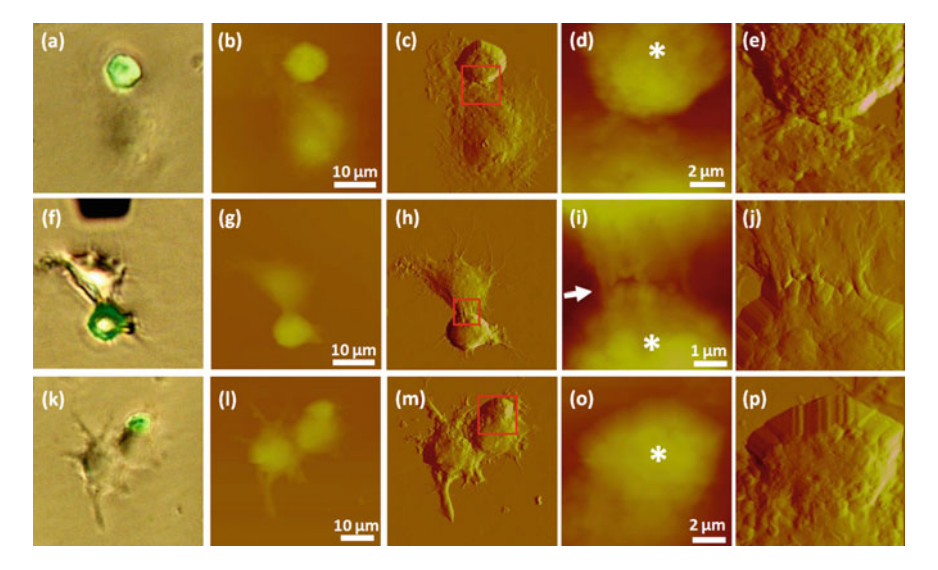


Fig. 6.6 AFM images reveal the changes in cellular ultra-microstructures during the process of rituximab-mediated macrophage phagocytosis against cancerous cells [19]. **a**, **f**, **k** Overlay images of optical images and fluorescent images. **a**–**e** Initial contact stage between a cancerous cell and macrophage. **f**–**j** Beginning of engulfing. **k**–**p** Some proportion of the cancerous cell has been engulfed by macrophage. **b**, **g**, **l** AFM height images and **c**, **h**, **m** corresponding deflection images on a large-size scan area. **d**, **i**, **o** AFM height images and **e**, **j**, **p** corresponding deflection images on a small-size scan area denoted by the red squares

Figure 6.7 shows that one macrophage could engulf several cancerous cells. Figure 6.7a-e shows the phagocytosis where one macrophage engulfed three cancerous cells. Figure 6.7a is the overlay of optical image and fluorescence image. From the overlay image, we can discern that three cancerous cells contacted with the macrophage according to the fluorescence. Figure 6.7b, c are the AFM height image and corresponding deflection image respectively. Figure 6.7d is the AFM local scanning height image of the cancerous cell denoted by the red square in Fig. 6.7c. From the local scanning AFM images, we can see that the boundary between the cancerous cell and macrophage was not clear and some proportions of cancerous cell had been coated by macrophage. Figure 6.7e is the AFM local scanning height image of the cancerous cell denoted by the blue square in Fig. 6.7c. The boundary between the cancerous cell and macrophage was apparent and the cancerous cell had not been engulfed. Figure 6.7f-j shows the phagocytosis where one macrophage engulfed six cancerous cells. From the overlay image (Fig. 6.7f), we can see that the macrophage also exhibited fluorescence, and we could see five cancerous cells were around the macrophage. While from the AFM deflection image (Fig. 6.7h), we can clearly see that besides the five cancerous cells around the macrophage, there was also one cancerous cell (denoted by the white arrow) which had been swallowed by the macrophage. It was this cancerous cell that make the macrophage exhibit fluorescence. Figure 6.7i, j are the AFM local scanning images of two cancerous cells (denoted by the red and blue squares in Fig. 6.7h) and the macrophage begun to engulf these two cancerous cells. Researchers have used AFM to investigate cell-cell interactions (e.g., fungus-macrophage [7], bacteria-phage [11]) and virus-cell interactions [12]. Here the results (Figs. 6.6 and 6.7) obtained by AFM improve our understanding of the macrophage phagocytosis against cancerous cells.

The results in Figs. 6.6 and 6.7 were obtained on chemically fixed cells. We then tried to image the macrophage phagocytosis on living cells by AFM. Under the guidance of optical microscopy, AFM tip was moved to a macrophage which had

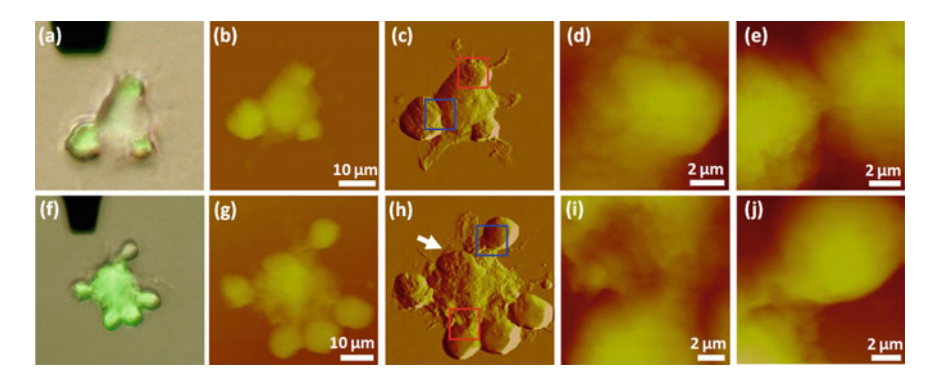


Fig. 6.7 AFM images of macrophages enfulfing several cancerous cells simultaneously [19]. \mathbf{a} - \mathbf{e} One macrophage enfulfing three cancerous cells. \mathbf{d} corresponds to the red square area in \mathbf{c} and \mathbf{e} corresponds to the blue square area in \mathbf{c} . \mathbf{f} - \mathbf{j} One macrophage enfulfing six cancerous cells. \mathbf{i} corresponds to the red square area in \mathbf{h} and \mathbf{j} corresponds to the blue square area in \mathbf{h}

adsorbed a cancerous cell (Fig. 6.8a). The cancerous cell in Fig. 6.8a was denoted by the black arrow. Then AFM scanning was performed on the two cells, but we found that it is hard to obtain AFM images of living cancerous cells. The optical image after the scanning was shown in Fig. 6.8b. We can see that the position of the cancerous cell changed from one side of the macrophage to another side after the scanning. Though cancerous cells bind to macrophage via antibodies, the conjugations were not strong enough to withstand the force exerted by the scanning tip and hence the cancerous cells were pushed by the scanning tip. In order to investigate the detailed topography of living macrophages, we then used AFM to image living macrophages and the results are shown in Fig. 6.8c-f. Figure 6.8c, d are the AFM height image and deflection image of the macrophage respectively. The scan size was 60 µm. Lamellipodium and filopodium were evident in the AFM images (denoted by the white arrows). Then local area scanning was performed on the central region of the cell (denoted by the red square), and the AFM images were shown in Fig. 6.8e, f. We can clearly see the corrugated morphology of the macrophage surface. Macrophage is a adherent cell and can spread on the substrate, which make it easy to acquire AFM images of living macrophages. In the living organisms, there are various types of cells. Each type of cell has its unique geometries (e.g., shapes, sizes) and the cell geometry is closely related to cellular physiological functions [13]. The shape of motile cells is determined by many dynamic processes which involve many interacting elements (e.g., cytoskeleton,

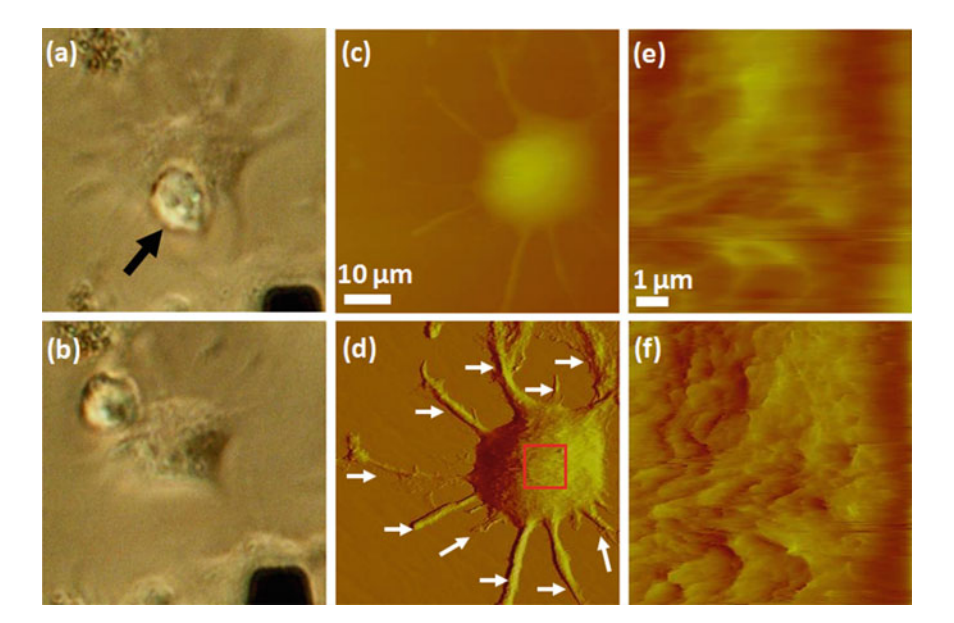


Fig. 6.8 AFM images of living macrophages [19]. Optical images of a macrophage with a cancerous cell \mathbf{a} before and \mathbf{b} after AFM scanning. \mathbf{c} AFM height image and \mathbf{d} corresponding deflection image of a living macrophage. \mathbf{e} AFM height image and \mathbf{f} corresponding deflection image of the local area (denoted by the red square in \mathbf{d}) on the macrophage

cell membrane, cell-substrate adhesions) [14]. From the AFM images of living macrophages, we can see the apparent morphological features of macrophages, e.g., the long lamellipodium, the corrugated surface morphology. We know that macrophages move in the tissues to kill the malignant cells and this special morphology may be beneficial and suited for the phagocytosis function of macrophage.

We then used AFM to obtain force curves on macrophages with and without cancerous cells to investigate whether phagocytosis influence cellular mechanical properties. The process of calculating the cellular Young's modulus from a force curve was shown in Fig. 6.9. Figure 6.9a is a typical force curve obtained on macrophages which trapped cancerous cells. Figure 6.9b is a typical force curve obtained on macrophages which did not adsorb cancerous cells. From the optical image in Fig. 6.9a, we can clearly see that a cancerous cell contacted with the macrophage. While from the optical image in Fig. 6.9b, the macrophage did not adsorb cancerous cells. According to the contact point (denoted by the arrows in Fig. 6.9a, b), the approach curve was converted to indentation curve. By applying Hertz model, the Young's modulus of cells was then computed from the indentation curve. Each indentation curve contained many discrete data points and each point could be used to compute a Young's modulus. Hence, we can often obtain hundreds of Young's modulus for each indentation curve. The histograms of Young's modulus values were plotted, as shown in Fig. 6.9c, d. After putting the Gaussian fitting mean value into the Hertz model formula, we can obtain the fitting indentation curves, and the contrast of experimental indentation curve and fitting indentation curve was shown in Fig. 6.9e, f. We can see that the experimental indentation curve was consistent with the fitting indentation curve.

Figure 6.10a shows the Young's modulus changes of macrophages after phagocytosis. For each situation (with cancerous cell and without cancerous cell), five macrophages were measured. When macrophages adsorbed cancerous cells, the Young's modulus of macrophages was in the range of 2–5 kPa. When macrophages did not adsorb cancerous cells, the Young's modulus of macrophages was in the range of 1-3 kPa. We can see that after the binding of cancerous cells, the macrophages became stiffer. When co-incubating the rituximab-coated cancerous cells and macrophages, cancerous cells could come into contact with adherent macrophages simply by landing on or near them under the influence of gravity [15]. After the contact of cancerous cells with macrophages, the Fc domains of rituximab on the cancerous cells then bound to the Fc receptors on the surface of macrophages and this would activate the macrophage phagocytosis. The ability of eukaryotic cells to establish their asymmetrical shapes, to transport intracellular constituents and to drive their motility depends on the cytoskeleton, an interconnected network of filamentous polymers and regulatory proteins [16]. Actin cytoskeleton determines the mechanical properties of a cell [17]. When the macrophage phagocytosis is activated, a rapid accumulation of F-actin and associated proteins in the periphagosomal region occurs [18, 19]. This phenomenon can be clearly seen in Fig. 6.8a, b. In Fig. 6.8a, we can distinctly see the internalization of the cancerous cell to the macrophage. When the cancerous cell was pushed by the scanning tip, we can see a distinct concave on the macrophage (Fig. 6.8b). Hence, actin

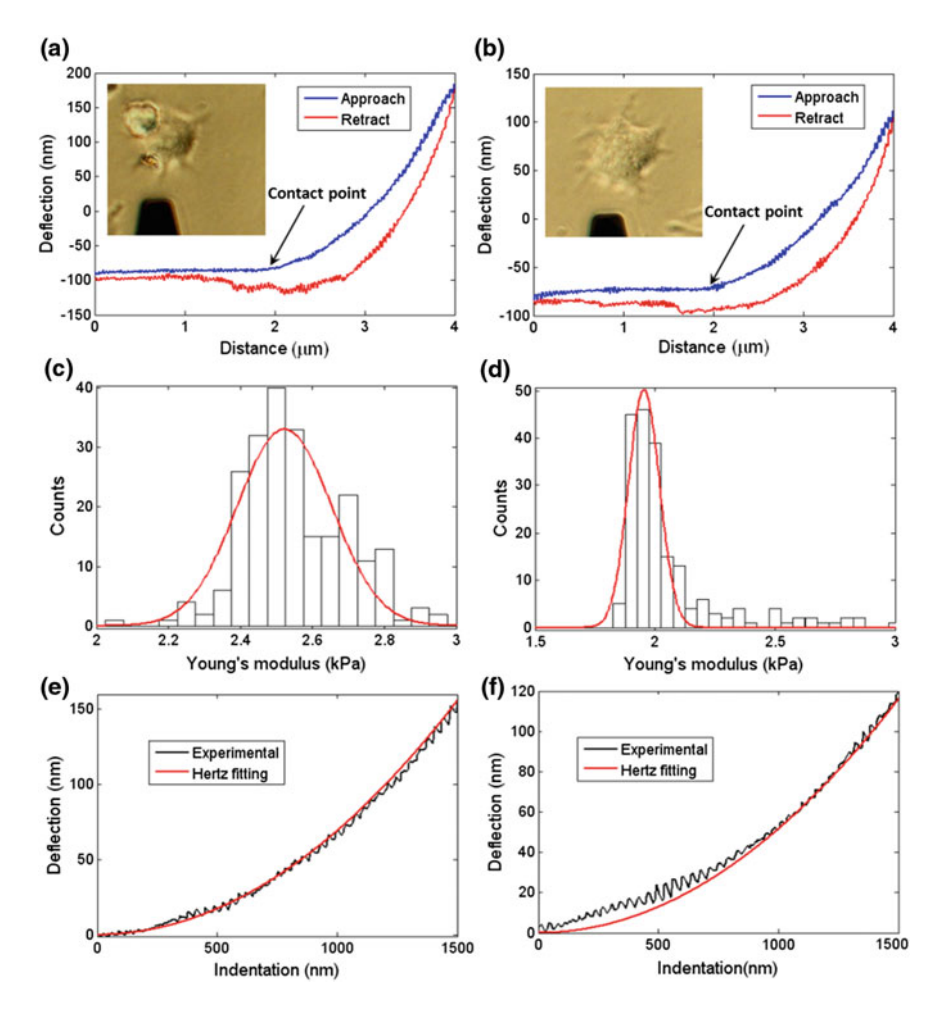


Fig. 6.9 Measuring the cellular Young's modulus of macrophages by obtaining force curves for macrophages with or without cancerous cells [19]. **a**, **c**, **e** Macrophage with a cancerous cell. **b**, **d**, **f** Macrophage without a cancerous cell. **a**, **b** Typical force curves. **c**, **d** Histogram of the Young's modulus values. **e**, **f** Fitting the experimental indentation curve (converted from approach curve) with Hertz model

cytoskeleton reorganized during the macrophage phagocytosis and this reorganization may lead to the changes of cellular mechanical properties. In order to examine whether the introduction of Raji cells cause the stiffening of macrophages, we measured the Young's modulus of Raji cells. Because Raji cell is a type of suspended cell, we attached them onto the glass slide via poly-L-lysine. Five Raji cells were selected for obtaining force curves. From Fig. 6.10a we can see that the Young's modulus of Raji cells were 1–3 kPa, comparable to the Young's modulus of macrophages (without Raji cells). While the Young's modulus of macrophages

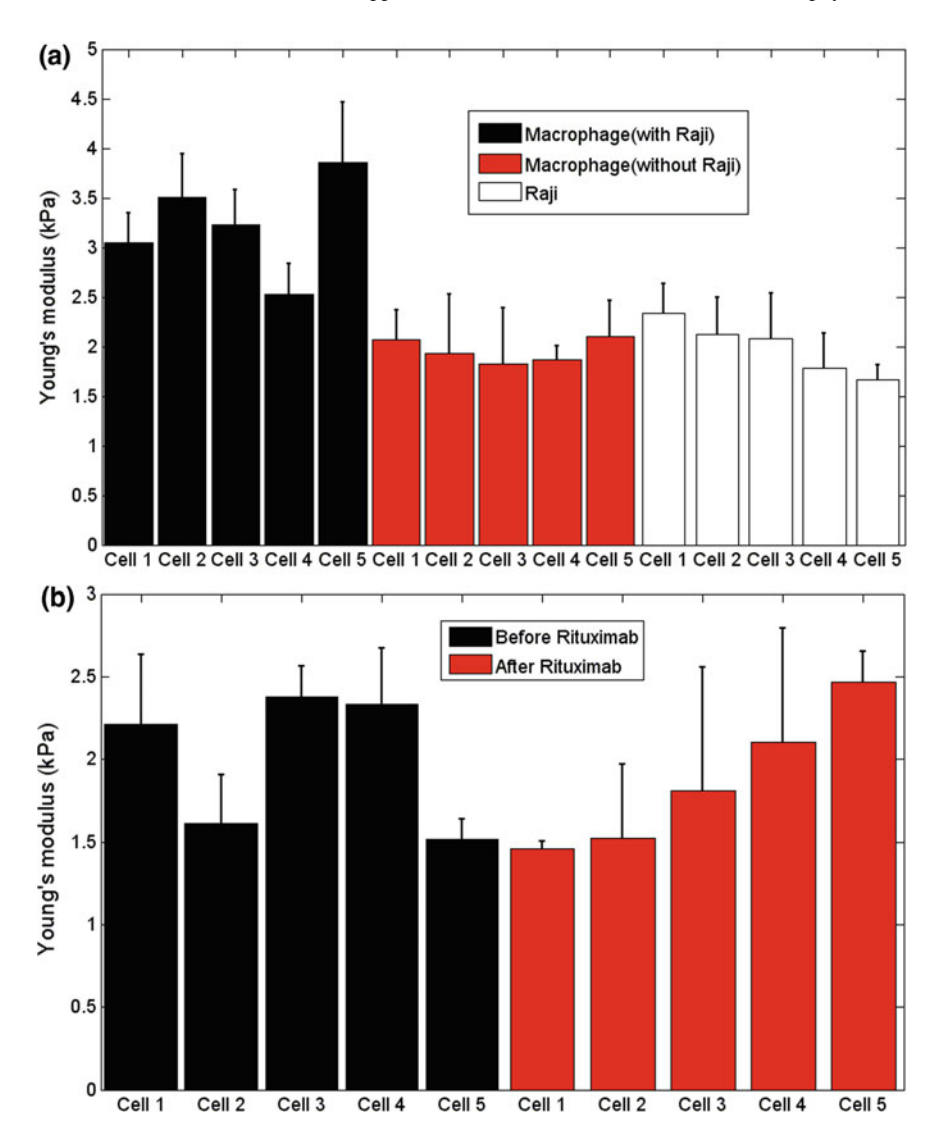


Fig. 6.10 Measuring the mechanical properties of macrophages during phagocytosis [19]. **a** Young's modulus of macrophages (with and without cancerous cells) and cancer cell. **b** Young's modulus of macrophages before and after the stimulation of rituximab

became 2–5 kPa after engulfing the cancerous cells, significantly larger than the Young's modulus of Raji cells. Hence, we can conclude that the stiffening of macrophages were caused by the activation of phagocytosis activities of macrophages, not the introduction of cancerous cells.

For control experiments, we investigated whether the single stimulation of rituximab can influence the cellular mechanical properties and the results were

shown in Fig. 6.10b. Force curves were first obtained on five living macrophages. Then rituximab solution was added and incubated for 3 h at 37 °C (5% CO₂). After the incubation, force curves were obtained on the five macrophages. From Fig. 6.10b, we can see that before the stimulation of rituximab, the Young's modulus of macrophages was in the range of 1-3 kPa, consistent with the measured Young's modulus in Fig. 6.10a. After the stimulation of rituximab, the Young's modulus of macrophages was still in the range of 1-3 kPa. This indicated that the stimulation of rituximab did not influence the mechanical properties of macrophages. In the antibody-dependent Fc receptor-mediated macrophage phagocytosis against cancerous cells, the cancerous cells were linked to the macrophages via antibodies and the actin cytoskeleton rapidly reorganized to assist engulfing the cancerous cells. The reorganization of actin cytoskeleton then caused the changes of the cellular mechanical properties. But when only the Fc domains of rituximab bind to the Fc receptors of the macrophage (the Fab domains of rituximab are free), there was no actin cytoskeleton reorganization and the cellular mechanical properties kept unchanged after the single stimulation of rituximab.

In summary, AFM was used to visualize and quantify the nanoscale cellular properties (ultra-microstructure, mechanical properties) during rituximab-induced macrophage phagocytosis against lymphoma cells, showing the dynamic changes of cell mechanics during the process of phagocytosis. The experimental results improve our understanding rituximab's ADCC mechanism.

6.1.3 CDC Mechanism

Besides PCD and ADCC, the binding of rituximab to the CD20 of lymphoma cell also activate the pathway of complement dependent cytotoxicity (CDC) mechanism, which finally leads to the lysis of the cell. Fluorescence microscopy was firstly used to observe the rituximab-induced CDC mechanism on lymphoma cell, and the results are shown in Fig. 6.11. Propidium iodide (PI) dye is a commonly used agent for discriminating dead and viable cells [20]. PI molecules can infiltrate into the cells which have damaged plasma membranes, but can not infiltrate into the cells which have intact plasma membranes. Hence we used PI dye to detect the cell lysis in this study. Raji cells were cultured with human serum and rituximab for 2 h at 37 °C (5%CO₂). After the incubation, cells were harvested and stained by PI for fluorescence observation. Figure 6.11a, b are the bright field image and corresponding fluorescence image of Raji cells cultured with human serum and rituximab. We can see that there are many cells which exhibit fluorescence. Human serum contains complement for CDC. When Raji cells were incubated with human serum and rituximab, ritximab bound to the CD20 antigen on the surface of Raji cells and then the Fc domains of rituximab could bind the complement to trigger the CDC effect whose final product was the MAC in the cell membrane. MAC creates 10 nm pores in the cell membrane that facilitate free passage of water and solutes into and out of the cell [21]. PI molecules can thus

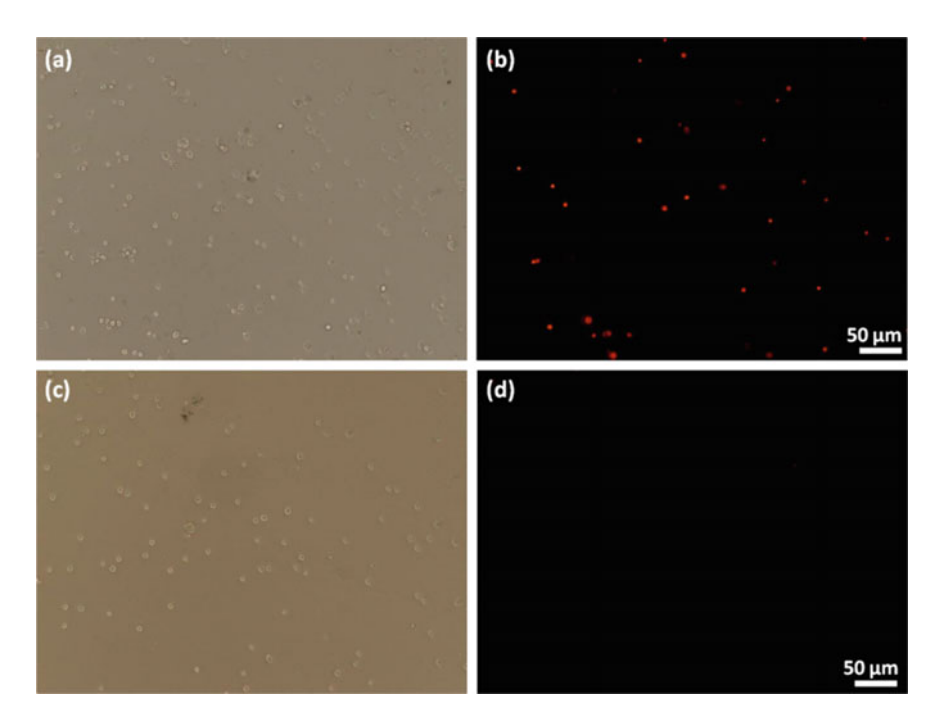


Fig. 6.11 Observing rituximab-mediated complement dependent cytotoxicity by fluorescence microscopy [24]. a, b PI staining of Raji cells after 2 h of incubation with human serum and rituximab. c, d PI staining of Raji cells after 2 h of incubation with human serum. a, c Optical bright field images and b, d corresponding fluorescence images

infiltrate into the cells via the MAC pores to stain the cell nucleus and thus cells exhibited bright fluorescence. Figure 6.11c, d are the bright field image and corresponding fluorescence image of Raji cells cultured with human serum (a control group), and we can see that cells do not exhibit fluorescence. Other two control groups were also performed, including Raji cells cultured with 1640 medium, and Raji cells cultured with rituximab, and the cells from the control groups also do not exhibit fluorescence (data not shown). The activation of CDC on Raji cells requires the existence of rituximab and complement. While in the cases of the three control groups, this requirement was not met and thus CDC effect was not activated. Hence cells cultured in the control groups were viable and did not exhibit fluorescence. Rituximab can directly induce the apoptosis of Raji cells after binding to the CD20 antigen, but this requires more than 24 h [22–24]. Here, cells were cultured only for 2 h and thus the apoptosis directly induced by rituximab was not observed.

Figure 6.12 shows the dynamic changes of fine structures on the cell surface during the process of rituximab-induced CDC mechanism. The AFM images distinctly reveal the morphological features of cells for the different stages of CDC mechanism. Cells were cultured with human serum and rituximab for 2 h. After incubation, cells were dropped onto the glass slide and fixed by 4%

paraformaldehyde for 30 min. AFM images were recorded at contact mode in PBS. The scan rate was 0.5 Hz. Figure 6.12a-c are AFM images of Raji cells which corresponded to the initial stage of CDC mechanism where micropores began forming on the cell surface. Firstly large-size scanning was performed to visualize whole cells and then small-size scanning was performed to visualize fine structures. From the AFM images, we can clearly see that some pores occurred on the cell surface (denoted by the arrows in Fig. 6.12b). From the AFM images, we can measure the diameter of holes by applying the AFM offline software (Nanoscope Analysis, Bruker, Santa Barbara, CA, USA). The size of holes was summarized in Table 6.1. From Table 6.1a, we can see that the size of the holes at the initial stage was about 150-500 nm. At this stage, we did not see the outflow of cytoplasm. Figure 6.12d-f corresponded to the stage where pores on the cell surface became larger and cytoplasm began escaping from the cell. At this stage, many more pores formed (denoted by the arrows in Fig. 6.12e). From Table 6.1b, we can see that the size of the pores at this stage was about 400-700 nm, significantly larger than that at the initial stage. Besides, we can distinctly see that some portion of cytoplasm had escaped from the cell (denoted by the red arrow in Fig. 6.12d), Figure 6.12g-i corresponded to the CDC stage where cytoplasm had totally escaped outside the cell and only cell membrane debris left. At this stage, the holes continued to became larger. From Table 6.1c, we can see that the size of holes were in the range of 600– 2000 nm. Besides, at this stage, because of the outflow of cytoplasm, the cells collapsed and we can only see the cell membrane debris. AFM images of Raji cells from control groups were also obtained, as shown in Fig. 6.12j-o. Figure 6.12j, k are AFM images of the Raji cells cultured in 1640 medium, Fig. 6.12l, m are AFM images of the Raji cells cultured in 1640 medium containing 50% human serum, and Fig. 6.12n, o are AFM images of Raji cells cultured in 1640 medium containing rituximab. From the AFM imgaes from control groups, we can see that the cell surface was intact without micropore forming on cell surface, confirming that the morphological changes in Fig. 6.12a-i of Raji cells were caused by the rituximab-induced CDC mechanism.

During the rituximab-induced CDC mechanism, membrane attack complex (MAC) is formed on cell surface. There are three complement activation pathways: classical pathway, lectin pathway and alternative pathway [25]. All of the three pathways have the same terminal product, MAC, which can cause the cell lysis. The binding of rituximab to the CD20 antigen on the surface of Raji cells can induce the formation of MAC via classical pathway. MAC is composed of complement proteins C5b, C6, C7, C8, and C9 [26]. Electron microscopy images of MACs isolated from erythrocytes have indicated that MAC exhibits a hollow cylinder structure [27]. From the optical images (Fig. 6.11), we can not see the detailed situations on the cell surface during the process of CDC due to the essential 200 nm resolution limit. AFM imaging (Fig. 6.12) can resolve the changes of ultra-microstructures (e.g., micropores, cytoplasm) of single cells during the process of CDC. The sizes of pores on the cell membrane observed here (150–2000 nm) were evidently larger than the size of MAC (~10 nm). When the MAC assembled in the cell membrane, the initial size of MAC pore was about 10 nm. Then due to the shear effect of the

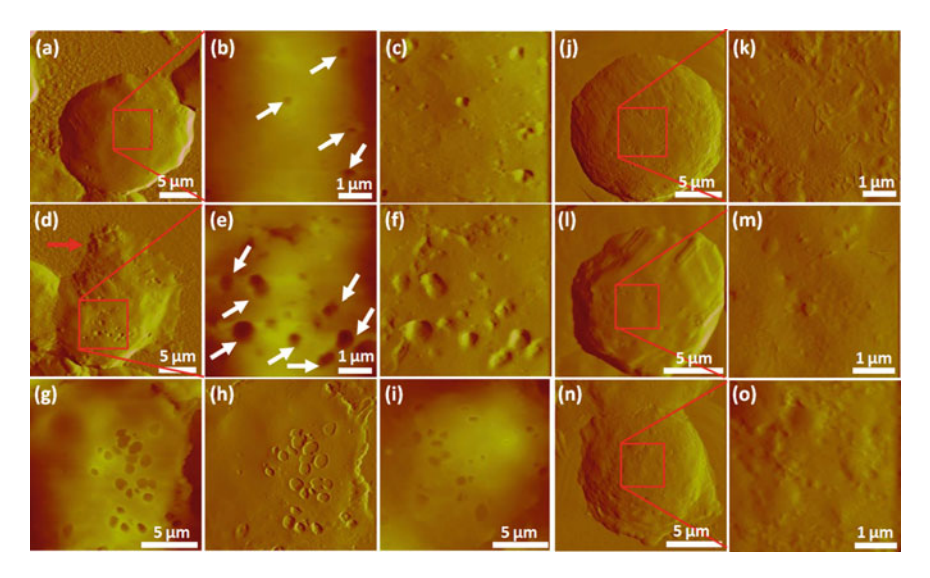


Fig. 6.12 AFM imaging of Raji cells during CDC effect [24]. a-i AFM images of Raji cells during the process of rituximab-induced CDC. a-c correspond to the initial stage of CDC where holes began forming on the cell surface. a AFM deflection image of whole cell. b AFM height image and c corresponding deflection image of the local area on cell surface. d-f correspond to the stage of CDC where cytoplasm escaped. d AFM deflection image of whole cell. e AFM height image and f corresponding deflection image of the local area on cell surface. g-i correspond to the stage of CDC where cells had collapsed. g AFM height image and h corresponding deflection image of a cell. i AFM height image of another cell. j-o AFM images of Raji cells from three control groups. j, k are cultured in 1640 medium. l, m are cultured in 1640 medium containing 50% human serum. n, o are cultured in 1640 medium containing rituximab. j, l, n are AFM deflection images of whole cells and k, m, o are AFM deflection images of local areas

flushing fluid (water molecules can freely enter into the cell membrane through the MAC pores), the pores can reasonably became larger. In fact, researchers have observed large sizes of pore-like structures (30–60 nm) [26]. Hence the pores on the cell surface observed here should be closely related to the CDC pores.

Figure 6.13 shows the process of moving AFM tip to the Raji cells which had CDC effect under the guidance of fluorescence. Raji cells were cultured with human serum and rituximab for 2 h. After the incubation, cells were PI-stained and then dropped onto the glass slides. The glass slides were then placed in a Petri dish in PBS. From the bright field image (Fig. 6.13a), we can see that there were three cells. From the fluorescence image (Fig. 6.13b), we can see that one cell exhibited fluorescence. The fluorescence confirmed that the cell was with CDC effect. Then the tip was moved to the fluorescence-shining cell to measure its mechanical properties. Figure 6.13d–f are the images after moving the AFM tip onto the fluorescent cell. The inset in Fig. 6.13f is the upright optical image of the AFM cantilever, confirming that the fluorescent cell was beneath the AFM tip.

			3	U	. ,
Hole	Hole diameter	Hole	Hole diameter	Hole	Hole diameter
ID	(nm)	ID	(nm)	ID	(nm)
(a) Pore formation					
1	219	6	416	11	185
2	206	7	332	12	280
3	311	8	269	13	241
4	391	9	241	14	427
5	228	10	490	15	253
(b) Cytoplasm escape					
1	697	6	626	11	314
2	490	7	458	12	449
3	521	8	484	13	324
4	443	9	554	14	494
5	546	10	477	15	443
(c) Membrane debris					
1	1140	6	741	11	978
2	1150	7	1090	12	812
3	871	8	1660	13	1600
4	1330	9	671	14	932
5	1040	10	1380	15	1400

Table 6.1 Sizes of holes on the surface of Raji cells at different stages of CDC effect [24]

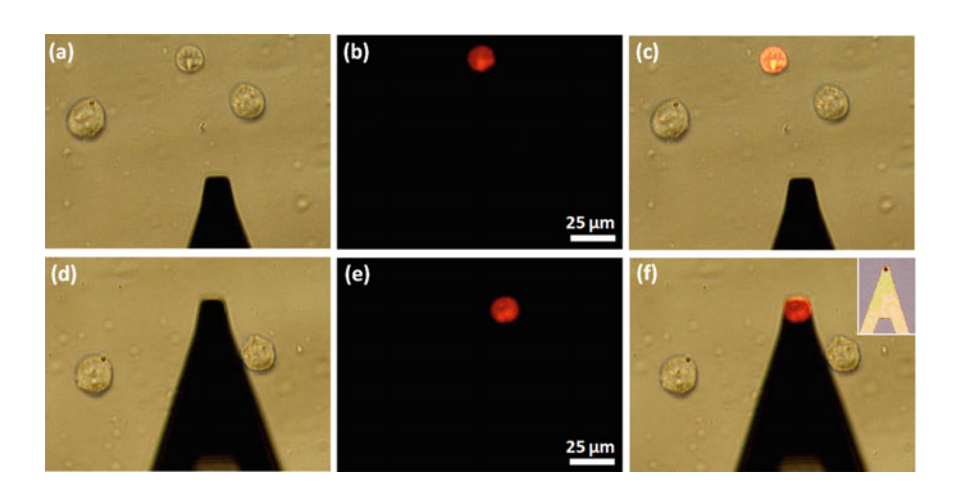


Fig. 6.13 AFM tip was moved to the Raji cell with CDC effect under the guidance of PI fluorescence [24]. **a** Bright field image, **b** fluorescence image and **c** overlay image before moving AFM tip to the cell. **d** Bright field image, **e** fluorescence image and **f** overlay image after moving AFM tip to the cell. The inset in **f** is the upright optical image of AFM cantilever

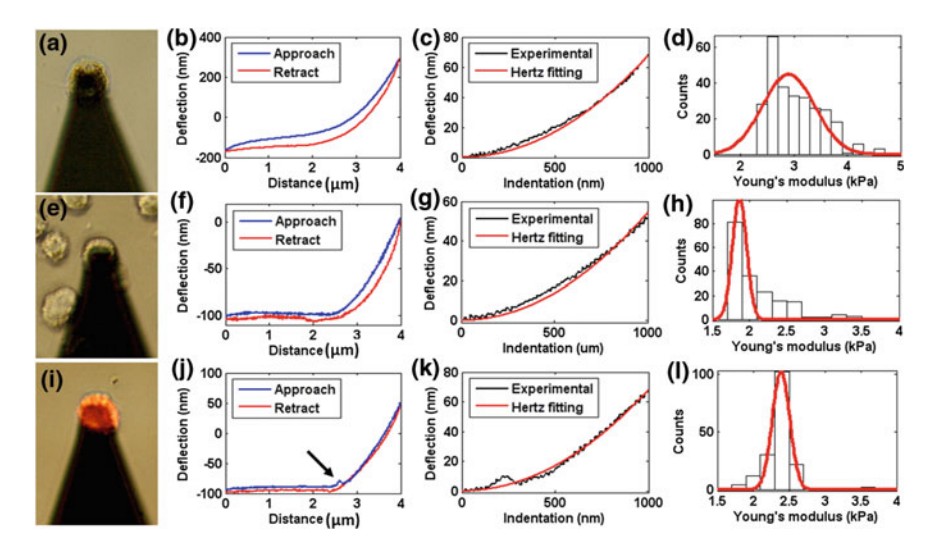


Fig. 6.14 Measuring the mechanical properties of Raji cells for three situations (before treatment, without CDC after treatment, with CDC after treatment) [24]. a-d corresponded to the Raji cells before treatment. e-h corresponded to the Raji cells after treatment (without CDC). i-l corresponded to the Raji cells after treatment (with CDC). a, e, i are optical images. b, f, j are typical force curves. c, g, k are Hertz fittings of experimental indentation curves. d, h, l are histograms of Young's modulus values

Figure 6.14 shows measuring the Young's modulus of cells by recording force curves on Raji cells for three situations (before treatment, without CDC after treatment, with CDC after treatment). Figure 6.14a-d correspond to the Raji cells cultured in 1640 medium. At this case, due to the lack of CDC effect, Raji cells did not exhibit fluorescence. Under the guidance of optical microscopy, AFM tip was moved to the cells (Fig. 6.14a) to obtain force curves. Figure 6.14b is a representative force curve. After converting the approach curve into indentation curve according to the contact point, we can obtain many Young's modulus by applying Hertz model and the histogram of Young's modulus is shown in Fig. 6.14d. The Gaussian fitting shows that the mean value was 2.9 kPa. After putting the 2.9 kPa into the Hertz model equation, the Hertz fitting indentation curve was obtained, as shown in Fig. 6.14c. We can see that the experimental indentation curve was consistent with the Hertz fitting indentation curve. From the results of Fig. 6.11, we can see that some cells exhibited fluorescence after the incubation with human serum and rituximab and some cells did not exhibit fluorescence. For the cells which did not exhibit fluorescence, we measured their mechanical properties, as shown in Fig. 6.14e-h. Under the guidance of optical microscopy, AFM tip was moved to the cells (Fig. 6.14e) to obtain force curves. Figure 6.14f-h are typical force curve, Hertz fitting, and histogram respectively. Figure 6.14i-l correspond to the Raji cells with CDC effect after incubation in 1640 medium containing 50% human serum and rituximab. Under the guidance of fluorescence (Fig. 6.14i), AFM tip was moved to the target cells to obtain force curves. Figure 6.14j is a typical force curve. From the force curve, we can see that there was an abrupt peak in the approach curve (denoted by the black arrow). This peak meaned that the tip penetrated the cell membrane [28, 29]. For the cells with CDC effect, MAC pores formed and these pores can become larger as the CDC progressed, as observed in Fig. 6.12. Due to the existence of these pores on the cell membrane, the tip can easily penetrate the cell membrane from these pores. This caused the abrupt peaks in the approach curves.

Figure 6.15 shows the Young's modulus changes of Raji cells for three situations (before treatment, without CDC after treatment, with CDC after treatment). From Fig. 6.15, we can see that the Young's modulus of Raji cells before the treatment of human serum and rituximab was in the range of 1.5–3 kPa. After the treatment of human serum and rituximab, the Young's modulus of Raji cells without CDC effect was in the range of 0.5–2.5 kPa, and the Young's modulus of Raji cells with CDC effect was in the range of 2–9 kPa. The results in Fig. 6.15 clearly showed that the Young's modulus of Raji cells during the process of CDC effect decreased firstly and then increased remarkably. The cells without CDC effect after the treatment of human serum and rituximab were softer than the Raji cells without treatment. This may be caused by the direct apoptotic effect of rituximab. In Fig. 6.4, the results have shown that the treatment of rituximab could cause the Raji cells become softer. The binding of rituximab to the CD20 antigen on the surface of Raji cells can activate the apoptotic signaling pathway, which could thus induce

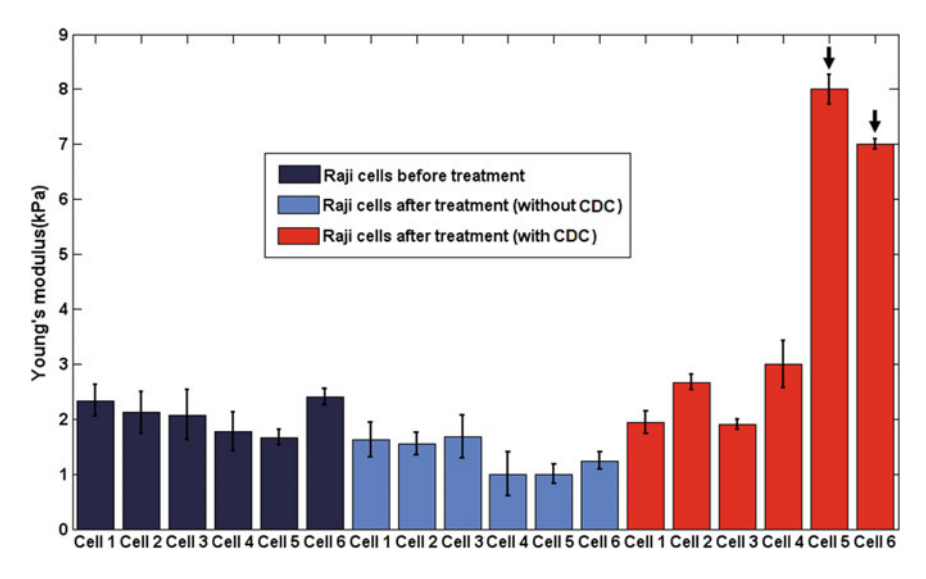


Fig. 6.15 The Young's modulus changes of Raji cells during the process of CDC [24]

various changes of cells, such as the changes of mechanical properties. Hence when culturing Raji cells in 1640 medium containing human serum and rituximab, the apoptotic effect of rituximab can thus cause the decrease of Young's modulus of Raji cells. It should be noted that the direct apoptotic effect of rituximab on cells can be detected by fluorescence after more than 24 h [20]. Here the stimulation time was only 2 h, meaning that cell membrane was still intact and cells did not exhibit fluorescence. For the cells with CDC effect after the treatment, the Young's modulus was significantly larger than the cells without CDC effect. This may be related to the CDC effect on Raji cells. The CDC effect can generate MAC pores on the cell membrane and this finally caused the cell lysis. This biological process can reasonably cause the changes of mechanical properties. Lam et al. [30] have investigated the changes of mechanical properties of leukemia cells after the treatment of anti-cancer chemotherapy drugs and the results indicated that dead cells (PI positive) caused by chemotherapy drugs were prominently stiffer than live cells. Here we can see that we obtained similar results: the cells with CDC effect (PI positive) became stiffer than live cells (PI negative). The mechanical properties of cells were dependent on the cytoskeletons [31]. Hence the CDC effect may cause the changes of cytoskeleton. The changes of cytoskeleton may then lead to the increase of cell Young's modulus. It is noticed that some cells (denoted by the black arrow in Fig. 6.15) exhibited a much larger Young's modulus, about four times larger than the live cells. This may because the tip probed the cell nucleus. The obtained force curves showed that the tip can easily penetrate the membrane of cells with CDC effect (denoted by the black arrow in Fig. 6.14j). Researchers have shown that the stiffness of cellular nucleus (chondrocytes, endothelial cells) was 3-10 times stiffer than cytoplasmic stiffness [32]. Hence, the measured Young's modulus significantly increased when probing the cell nucleus. The dynamic changes of Young's modulus of single Raji cell during CDC were also monitored, as shown in Fig. 6.16. Successive force curves were obtained on the same cells in 150 min. For cell 1, the cellular Young's modulus began to decrease 30 min after the addition of rituximab and human serum and finally increased to 10.3 kPa at the time of 150 min. For cell 2, we can also see that the cellular Young's modulus finally increased after the addition of rituximab and human serum. Especially, the Young's modulus of cell 1 and cell 2 at the time of 150 min (denoted by the black arrows in Fig. 6.16) was much larger than the Young's modulus before stimulation. This may because that the tip penetrated the cell membrane and probed the cell nuclei. All together, the results in Figs. 6.15 and 6.16 confirmed that Raji cells firstly softend and then stiffened during the rituximab-induced CDC mechanism.

In summary, the changes of cellular ultra-microstructures and cellular mechanical properties during the process of rituximab-induced CDC mechanism were visualized and measured, showing the unique morphological and mechanical changes at different stages of CDC. The experimental results improve our understanding of the CDC mechanism.

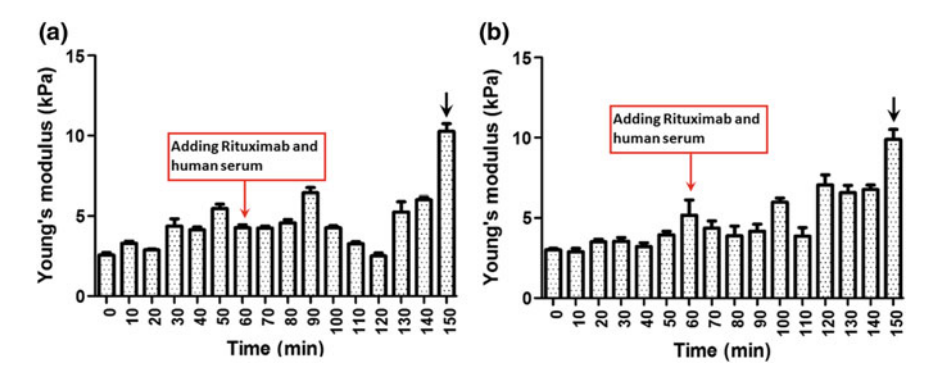


Fig. 6.16 Real-time Young's modulus changes of Raji cells during CDC [24]. a Cell 1. b Cell 2

6.2 Probing Target Proteins on Primary Cells from Clinical Lymphoma Patients

Most of current AFM single-cell assays are done on cell lines cultured in vitro. We know that the growth environment of cells cultured in vitro was quite different from the environment of cells in vivo [33]. For cells cultured in vitro, they lose the neurohumoral regulation and cell-cell influence and this huge difference of growth environment may cause the changes of the cellular structures and functions [34]. Hence the experimental results obtained from cells cultured in vitro can not completely reflect the real situations in vivo. From the view of clinical significance, investigating the behavior directly on primary cells from clinical patients will provide novel insights into the interactions between drugs and cells, which is of important significance for disease diagnosis and drug development. We know that the prerequisite of personalized medicine is having accurate diagnostic tests that identify patients who can benefit from the therapies [35], which requires us to exactly characterize the pathological properties of the patients. Directly probing the behaviors of primary cells from clinical patients can thus be useful for achieving this goal.

6.2.1 Detecting CD20-Rituximab Interactions on Patient Cancerous Cells

In order to investigate the behaviors of cancerous B cells of lymphoma patients, the prerequisite is to recognize them from healthy cells. Recent studies have shown that receptor tyrosine kinase-like orphan receptor 1 (ROR1) [36] is exclusively expressed on the surface of B-cell chronic lymphocytic leukemia (CLL) and on some B-cell lymphomas (including mantle cell lymphoma, marginal zone

lymphoma, follicular lymphoma), whereas normal B cells, other normal blood cells, and normal adult tissues do not express ROR1 [37–41]. Hence ROR1 is a suitable marker for distinguishing cancerous B cells from healthy cells. In this section, the methods of detecting CD20-rituximab interactions based on ROR1 fluorescence recognition were established on Raji cells. Then the established methods were used to probe the CD20-rituximab interactions on the primary cancerous cells from the bone marrow of clinical lymphoma patients.

(1) Detecting CD20-rituximab interactions based on ROR1 fluorescence recognition

Lymphoma Raji cells were used for testing the ROR1 fluorescence staining. The procedure of fluorescence labeling experiments was following. (1) Drop Raji cells onto the poly-L-lysine-coated glass slide and fix for 30 min with 4% paraformaldehyde. After washing the sample three times (each time 10 min) with PBS, donkey blocking serum was added and then incubate for 30 min at room temperature. ② Add 40 µL goat-anti-human-ROR1 antibody solution (R&D company, USA) and incubate for 3 h at room temperature. For control experiment, ROR1 antibody was not added. ③ Wash the sample three times with PBS, and then add 20 µL FITC-conjugated donkey-anti-goat IgG (KangChen company, Shanghai, China) and incubate for 30 min. (4) Wash the sample three times with PBS, and place the sample on the stage of the fluorescence microscope (Ti, Nikon company, Japan). ⑤ Add 20 μL rituximab and incubate for 3 h. ⑥ After washing the sample three times with PBS, add 20 µL rhodamine-conjugated goat-anti-human IgG (Solarbio company, Beijing, China) and incubate for 30 min. (7) Wash the sample three times with PBS and observe the fluorescence. The labeling experiment procedure of validating the tip functionalization was the same as **6**–**7**.

Figure 6.17 shows the ROR1 fluorescence labeling experimental results of Raji cells. Figure 6.17a is the optical image of control group and Fig. 6.17b is the corresponding fluorescence image. Figure 6.17c is the optical image of ROR1 group and Fig. 6.17d is the corresponding fluorescence image. We can see that Raji cells from the control group (without ROR1 antibodies) do not exhibit fluorescence (Fig. 6.17b), while cells exhibit bright green fluorescence when labeled with ROR1 antibodies (Fig. 6.17d). These experiments confirm that Raji cells express ROR1. Our goal is to measure the CD20-rituximab binding force based on the ROR1 fluorescence recognition. In order to examine whether the ROR1 fluorescence labeling influence the CD20s on the cell surface, CD20 fluorescence labeling experiments were performed on ROR1-labeled cells and the results are shown in Fig. 6.17e, f. The fluorescence color of ROR1 labeling experiments was green (FITC). In order to discriminate this color, we chose a red fluorescent dye (rhodamine) for CD20 labeling experiments. Figure 6.17e is the ROR1 fluorescence image and Fig. 6.17f is the corresponding CD20 fluorescence image. The optical image was not shown. We can see that after ROR1 labeling, the cells still exhibit red fluorescence, which indicates that there are CD20s on the cell surface.

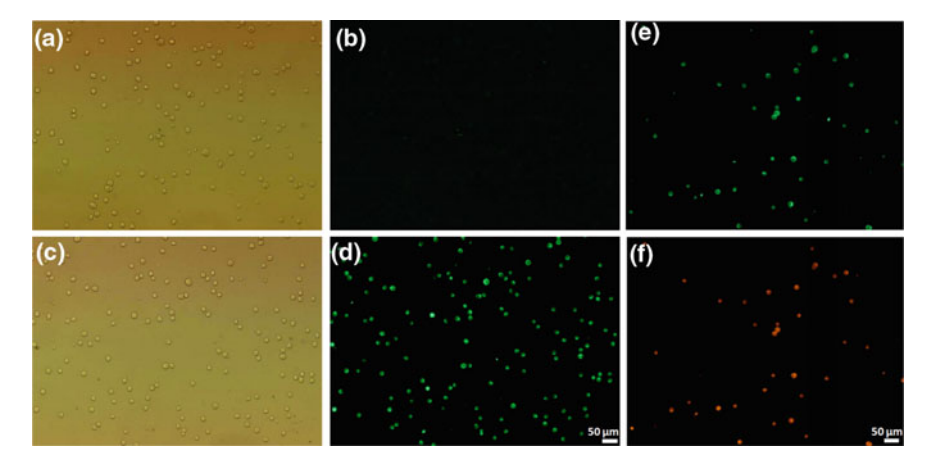


Fig. 6.17 Staining Raji cells with ROR1 and CD20 antibodies [34]. **a–d** ROR1 fluorescence labeling of Raji cells. Optical bright field image (**a**) and fluorescence image (**b**) of control group (without ROR1 antibody). Optical bright field image (**c**) and fluorescence image (**d**) of Raji cells with ROR1 antibody. **e**, **f** ROR1 and CD20 fluorescence labeling of Raji cells. **e** ROR1 fluorescence image. **f** CD20 fluorescence image

In order to examine whether CD20-rituximab interactions can be sensed on ROR1-labeled Raji cells, force curves were recorded with rituximab-tethered tip, as shown in Fig. 6.18. Figure 6.18a is a typical force curve obtained on the ROR1-labeled Raji cells with specific unbinding peak. We can see that there is a peak in the retract curve. The shape of the peak indicated that specific molecular binding occurred during the approach-retract process. To validate whether the binding was from CD20-rituximab, free rituximabs were added into the solution to block the CD20s on the cell surface. After blocking, force curves were obtained again. A typical force curve obtained after blocking was shown in Fig. 6.18b. We can see that there were no peaks in the retract portion of force curve, confirming that the peak in Fig. 6.18a corresponded to CD20-rituximab specific interactions. We tested the functionalized tip after force measurement experiments using fluorescence labeling, as shown in Fig. 6.19. Figure 6.19a is the fluorescence image of the functionalized probe. Figure 6.19b is the fluorescence image of the normal probe. We can see that the cantilever of the functionalized probe exhibited bright fluorescence while the cantilever of the normal probe was dim, confirming that there were rituximabs on the surface of AFM tip. Combining the experimental results of Figs. 6.18 and 6.19, we can conclude that CD20-rituximab binding force can be measured on ROR1-labeled cells by using AFM-based SMFS technique.

(2) Probing CD20s on primary cancerous cells from clinical lymphoma patients

The ROR1-based molecular detection methods established on Raji cells were then applied on primary cancerous cells prepared from the bone marrow of clinical

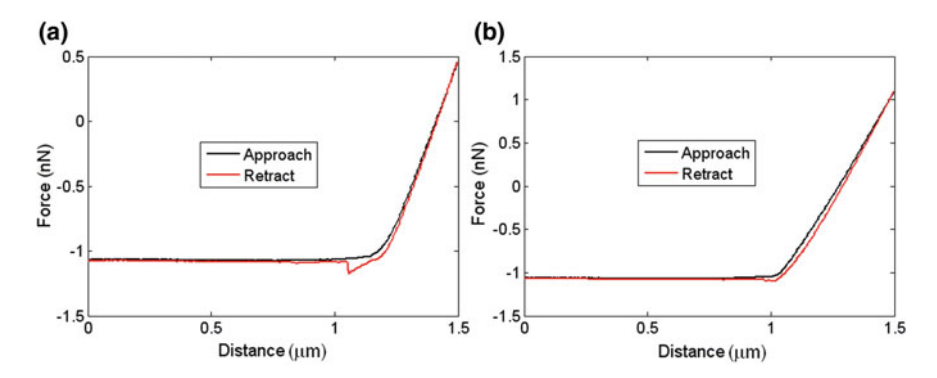


Fig. 6.18 Using rituximab-conjugated probe to obtain force curves on ROR1-labeled Raji cells [34]. **a** Typical force curve with specific CD20-rituximab binding. **b** Typical force curve after blocking (adding rituximab)

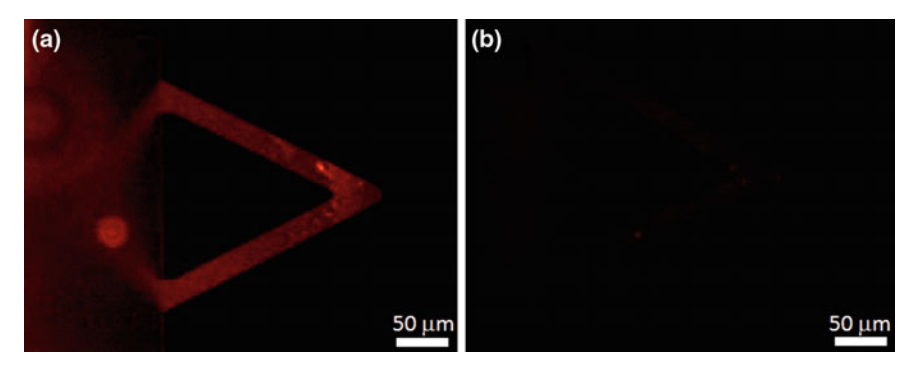


Fig. 6.19 Fluorescence image of functionalized probe and normal probe [34]. a Fluorescence image of a functionalized probe. b Fluorescence image of a normal probe

lymphoma patients. The clinical pathological samples were prepared by the medical personnel from Chinese Affiliated Hospital of Military Medical Academy of Sciences according to the standard procedures of bone marrow aspiration. A bone marrow biopsy was obtained from a B-cell NHL patient (marginal zone lymphoma) with bone marrow invasion, as shown in Fig. 6.20a. Then a drop of bone marrow was placed on a poly-L-lysine-coated glass slide and fixed for 30 min by 4% paraformaldehyde (Solarbio company, Beijing, China). Next, ROR1 labeling procedures were performed on the chemically fixed cell samples. For ROR1 labeling experiments, goat-anti-human-ROR1 antibody (R&D systems, Minneapolis, USA) and FITC-conjugated donkey-anti-goat IgG secondary antibody (KangChen company, Shanghai, China) were used. There were three main steps involved in the ROR1 labeling procedures. First donkey serum was used as the blocking reagent to avoid the non-specific staining. Then ROR1 antibody was added and incubated for 3 h at room temperature. Finally FITC-conjugated secondary antibody was added

and incubated for 30 min at room temperature. At the beginning of each step, the samples were washed 3 times (10 min each time) by using PBS. After the labeling, the samples were placed at the sample stage of a fluorescence microscope (Ti, Nikon, Japan) and the fluorescence images of the samples were obtained. For control experiments, the ROR1 labeling procedures were performed on the peripheral blood cells obtained from healthy volunteers.

Figure 6.20b—e shows the results of ROR1 fluorescence labeling experiments on primary cell samples prepared from a clinical lymphoma patient. First, ROR1 fluorescence labeling experiments were performed on the peripheral blood cells from healthy volunteers to test whether normal blood cells express ROR1. Figure 6.20b is the optical image of the peripheral blood cells and Fig. 6.20c is the corresponding ROR1 fluorescence image. We can see that there are many cells in the optical image, and all of them do not exhibit fluorescence, confirming that normal blood cells do not express ROR1. Next, ROR1 fluorescence labeling experiments were performed on the bone marrow cells from a B-cell NHL patient (marginal zone lymphoma) with bone marrow invasion. Researches have indicated that there were ROR1s on the surface of marginal zone lymphoma cells [39, 40]. Hence we select a case of marginal zone lymphoma for experiments. Figure 6.20d is the optical image of the bone marrow cells and Fig. 6.20e is the corresponding ROR1 fluorescence image. We can clearly see that four cells exhibit bright fluorescence and the other cells do not exhibit fluorescence. The patient was with bone marrow invasion. This means that cancerous cells had invaded into the bone marrow of the patient and thus there were cancerous cells in the sucked bone marrow cell samples. However, in the bone marrow cells, cancerous cells were the minority and the healthy cells were the majority. Hence we can see only a few cells

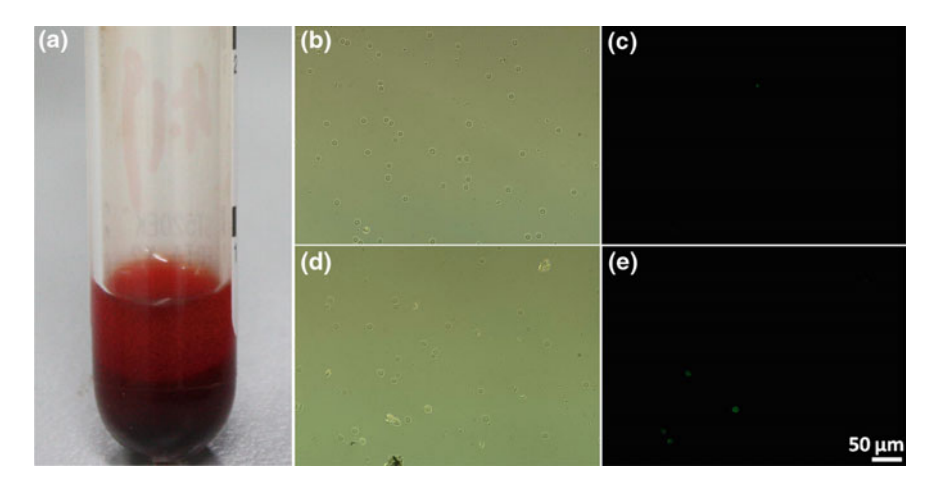


Fig. 6.20 ROR1 fluorescence labeling of biopsy cells prepared from clinical lymphoma patients [36]. **a** Bone marrow liquid extracted from the patients. **b**, **d** Optical bright field images and **c**, **e** corresponding fluorescence images. **b**, **c** are the blood cells extracted from the peripheral blood of a healthy volunteer. **d**, **e** are the bone marrow cells extracted from a lymphoma patient

exhibited bright fluorescence after the ROR1 fluorescence labeling procedure. Collectively, the ROR1 fluorescence experimental results confirmed that ROR1 expressed on marginal zone lymphoma cells, but did not express on normal blood cells.

Figure 6.21 shows the schematic diagram of detecting the CD20-rituximab interactions on cancerous B cells from B-cell NHL patients based on ROR1 fluorescence recognition. B-cell NHL results from the process of canceration by which healthy B cells transformed into cancerous B cells. B-cell NHL commonly involves the bone marrow invasion. The bone marrow samples obtained from B-cell NHL patients with bone marrow invasion contain cancerous B cells, healthy B cells, and other healthy cells. Both cancerous B cells and healthy B cells express CD20. Rituximab can bind to the CD20s of both cancerous B cells and healthy B cells, which leads to cell lysis. We are interested in the binding of rituximab to the CD20s of cancerous B cells, since this binding has direct impact on the rituximab's therapeutic outcomes. In order to investigate the CD20-rituximab interactions on cancerous B cells, we need to recognize cancerous B cells first. In some B-cell lymphomas, only cancerous B cells express ROR1, and the other cells (including healthy B cells) do not express ROR1 [37-41]. Hence we used ROR1 as a specific marker to recognize cancerous B cells from healthy cells of bone marrow cell samples. When the bone marrow cell samples were treated by ROR1 fluorescence labeling procedure, cancerous B cells exhibited bright fluorescence and the other cells were dark. Then under the guidance of fluorescence, the AFM functionalized tip carrying rituximab molecules through NHS-PEG-MAL linkers was moved onto the cancerous B cells to detect the CD20s on the cell surface.

AFM imaging and measurements were performed in PBS at room temperature using a Bioscope Catalyst AFM (Bruker, Santa Barbara, CA, USA) which was set

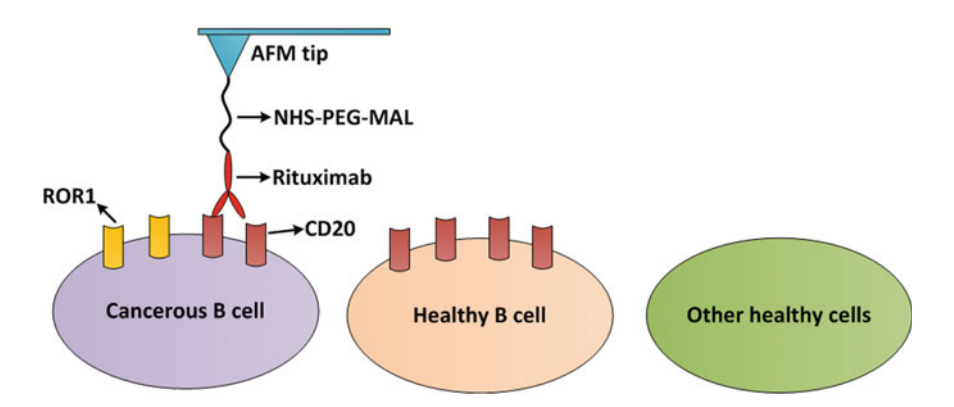


Fig. 6.21 Principle of detecting the CD20-rituximab interactions on cancerous B cells [36]. Rituximab is linked onto the AFM tip via the NHS-PEG-MAL molecule. Cancerous B cells express ROR1. Healthy B cells and other healthy cells do not express ROR1. Under ROR1 fluorescence recognition, AFM tip carrying rituximab molecules is moved to the cancerous B cell to detect the CD20-rituximab interactions on the cell surface

on an inverted fluorescence microscope (Ti, Nikon, Japan). The normal spring constant of the cantilever was 0.01 N/m and its exact spring constant was calibrated by thermal noise method. The deflection sensitivity of the cantilever was calibrated by obtaining force curves on the bare area of the glass slide. Under the guidance of fluorescence, the AFM functionalized tips were moved to the cancerous cells which exhibited bright green light. First the morphology of the cancerous cells were obtained by AFM imaging at contact mode. The scan force was 400 pN. The scan line and sampling point was 256. The scan rate was 1 Hz. Then arrays of force curves (16 \times 16) were obtained by zooming into local areas (500 \times 500 nm²) on the cell surface. Five functionalized tips were used to obtaining the force curves on eight cancerous cells. All the force curves were obtained at the same loading rate $(0.08 \times 10^6 \text{ pN/s})$. The sampling point of the force curves was 512. Also the functionalize tips were moved to healthy cells (red blood cells) to image the cellular morphology and obtain force curves. For specific CD20-rituximab recognition verification, arrays of force curves were first obtained on cancerous cells. After adding free rituximabs to block the CD20s on the cell surface, arrays of force curves were obtained again on the cancerous cells. For an array of force curves (16×16), each force curve corresponds to a binding force. The binding forces were computed by analyzing the force curves with Matlab 7.6 (MathWorks, Natick, MA, USA). After normalizing the binding forces into gray colors (0-255), the force map was constructed by using imaging processing software.

Figure 6.22 shows moving AFM probe to cancerous cells under the guidance of ROR1 fluorescence labeling. Figure 6.22a is the optical image and Fig. 6.22b is the corresponding ROR1 fluorescence image. Figure 6.22c is the merged image of optical image and fluorescence image. The merged image was obtained by merging the optical image and fluorescence image using a commercial image processing software Photoshop (Adobe, San Jose, CA, USA). Figure 6.22d is the higher resolution image of the merged image denoted by the square in Fig. 6.22c. From the fluorescence image, we can easily discern the cancerous cells (exhibiting green fluorescence). A cancerous cell is indicated by the yellow square in Fig. 6.22d. The blue square indicate three healthy cells. We can see that the three healthy cells do not exhibit fluorescence. Then the AFM images of the cancerous cell and healthy cells in Fig. 6.22d were recorded, as shown in Fig. 6.23. Figure 6.23a is the AFM height image and Fig. 6.23b is the corresponding deflection image of the cancerous cell. The image size was 15 µm. Figure 6.23c is the section curve of the cancerous cell, showing that the diameter of the cancerous cell is about 11 µm and the height is about 3.5 µm. Figure 6.23d is the AFM height image and Fig. 6.23e is the corresponding deflection image of the three healthy cells. In these three cells, we can clearly see that cell 1 is a red blood cell. Red blood cells have a special shape of oval biconcave disk, and thus we can easily discern them by this special shape. From the section curve of cell 1 (denoted by the red line in Fig. 6.23f), we can see a concave in the section curve and this is consistent with the special shape of red blood cells. The section curves of the three healthy cells (Fig. 6.23f) show that the diameter of healthy cells is similar to the diameter of the cancerous cell, but the the height (0.5–0.8 µm) of the healthy cells is significantly smaller than the height of

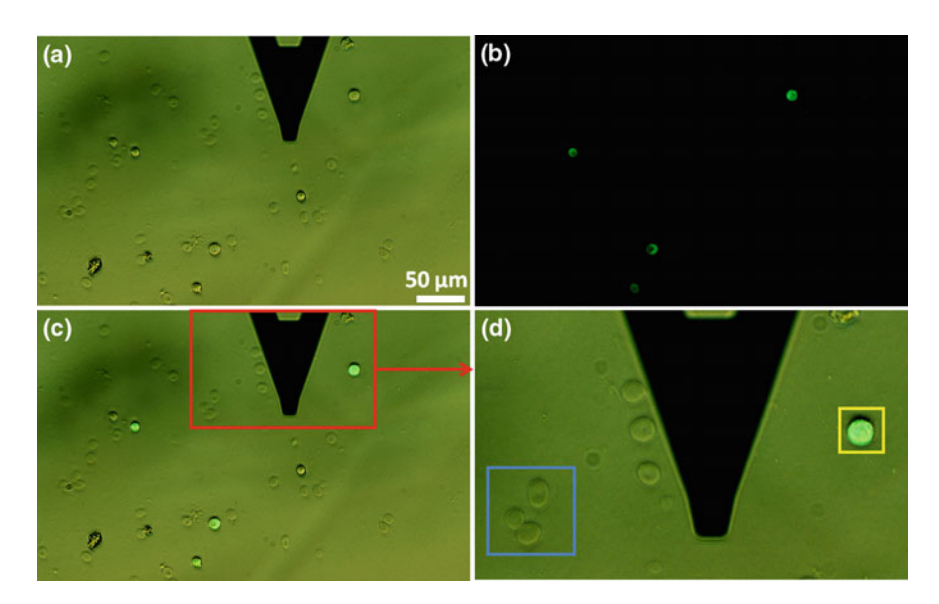


Fig. 6.22 AFM functionalized tip was moved onto the cancerous cell with the assistance of ROR1 fluorescence [36]. **a** Optical image, **b** corresponding ROR1 fluorescence image, and **c** merged image. **d** Merged image with higher resolution (denoted by the square in **c**). The red square indicates a cancerous cell and the blue square indicates three healthy cells

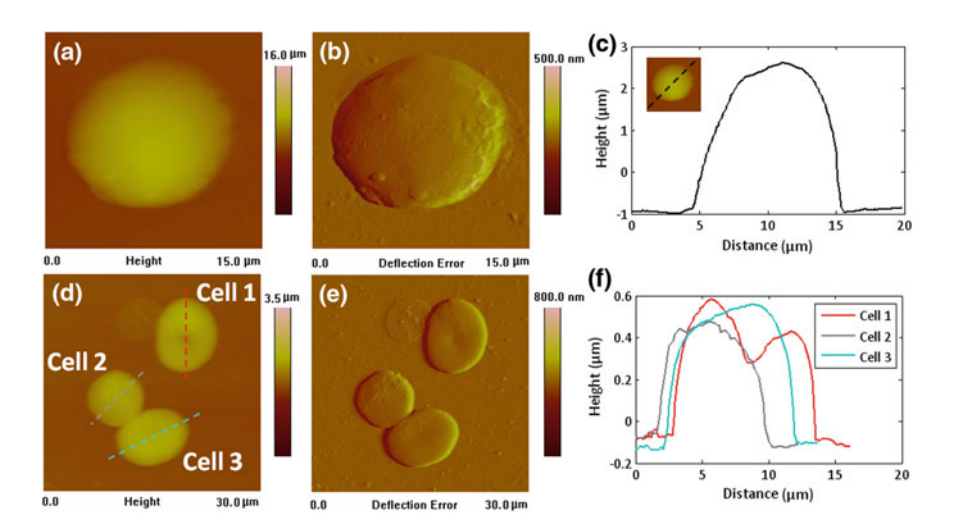


Fig. 6.23 AFM images of a cancerous cell **a-c** and three healthy cells (**d-f**) [36]. **a**, **d** AFM height images and **b**, **e** corresponding deflection images. **c**, **f** Section curves

cancerous cell. We know cancerous cells are quite different from normal cells. The transformation of normal cells into cancerous cells reflects the genetic alterations. Cancerous cells acquire many capabilities after the transformation, such as evading apoptosis, sustained angiogenesis, limitless replicative potential, tissue invasion and metastasis, insensitivity to anti-growth signals, and self-sufficiency in growth signals [42]. Hence the huge differences between cancerous cells and normal cells may cause the different cellular sizes.

Figure 6.24 shows probing the CD20-rituximab interactions on cancerous cells and healthy cells with rituximab-tethered tips. Figure 6.24a is a typical force curve obtained on cancerous cells with specific unbinding peak. The unbinding peak reflected the stretching of the flexible PEG spacer molecules [43, 44]. The inset is the enlarged view of retract curve in the range of 3–3.9 µm. The rituximab density attached to the AFM tip was controlled to be low enough to ensure that only one CD20-rituximab complex formed during each approach-retract cycle. A typical force curve obtained on erythrocytes is shown in Fig. 6.24b. The inset is the enlarged view of retract curve in the range of 1.2–1.7 µm. We can see that the force curve was flat (without specific unbinding peaks) in the force curve, and this is because erythrocytes do not express CD20. After obtaining arrays of force curves in local areas on cell surfaces, the histograms of adhesion forces are obtained, as shown in Fig. 6.24c, d. If force curves (retract curves) had specific unbinding peaks, then the force curves indicated CD20-rituximab recognition and the binding forces were computed (equal to the magnitude of the specific unbinding peak). If force curves (retract curves) were flat, then the force curves indicated no CD20-rituximab recognition and the binding forces were 0 pN. From the histogram of cancerous cells, we can see that the frequency of 0 pN is 83%, and this means that the frequency of specific binding was 17%. While the binding frequency of erythrocytes is only 3%. The binding occurred on erythrocytes was due to the non-specific molecular interactions. The Gaussian fit of the force histograms indicated that the specific binding force (54 \pm 38 pN) on the cancerous cells was distinctly larger than the non-specific binding force (21 \pm 19 pN) on erythrocytes.

In order to map the distribution of CD20s on the surface of cancerous cells, arrays of force curves (16×16) were obtained in the local areas ($500 \times 500 \text{ nm}^2$) of the cancerous cell. Each force curve corresponds to an adhesion force. After converting these forces into the gray colors (0–255), then a force map was constructed. The map reflects the distribution of CD20 on the cell surface. For the force map of cancerous cells (Fig. 6.24e), there were many bright or gray pixels. While there were few gray pixels in the force map of erythrocytes (Fig. 6.24f) and these pixels were dim. In order to statistically characterize the distribution of CD20s on the surface of cancerous cells, we obtained force curves on eight cancerous cells with five functionalized tips. For each cell, we obtained several distribution maps on different areas on the cell surface. The representative maps are shown in Fig. 6.25. From the distribution maps, we can see that the CD20 distribution on the cell surface was non-uniform. In some areas on the cell surface, there were CD20 clusters, whereas in some areas, there were discrete CD20s. We know that cell membranes are heterogeneous in composition, and the structures responsible for

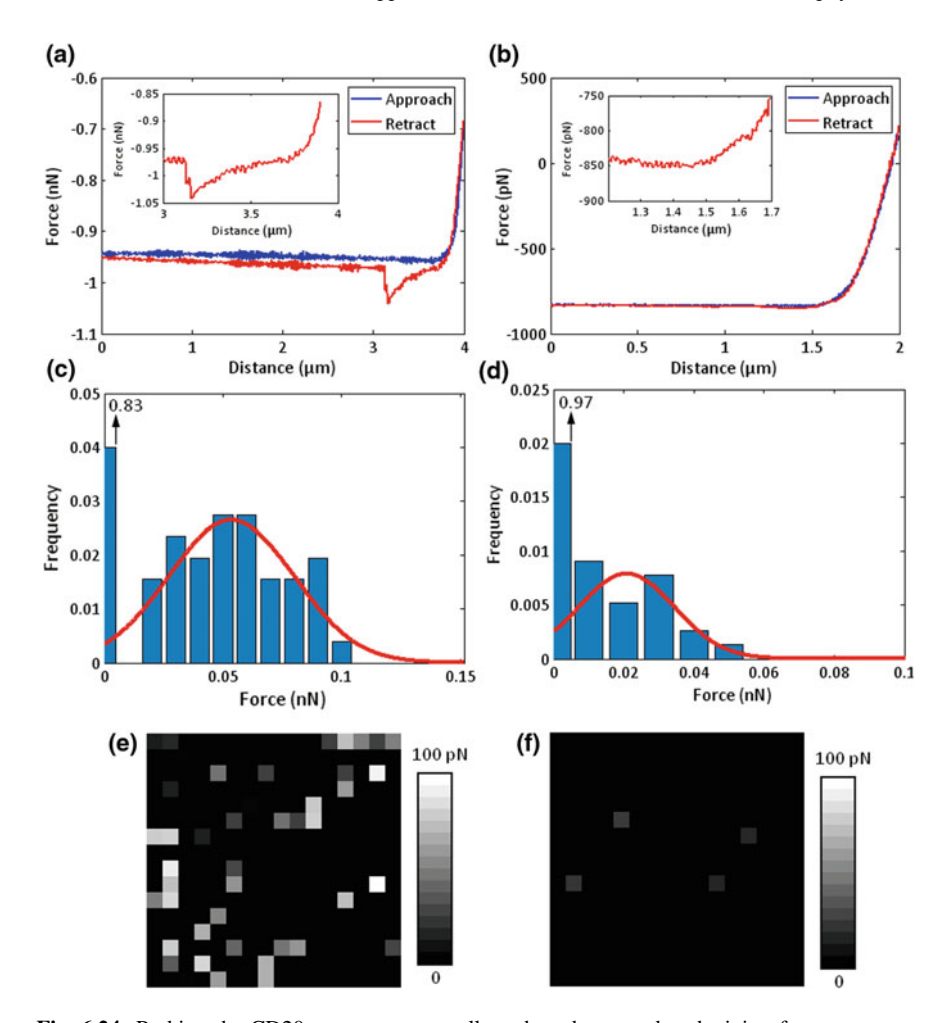


Fig. 6.24 Probing the CD20s on cancerous cells and erythrocytes by obtaining force curves on cell surface [36]. **a** A typical force curve (with specific unbinding peak) obtained on cancerous cells. **b** A typical force curve obtained on erythrocytes. The inset in **a** is the zooming in retract curve in the range of 3–3.9 μ m. The inset in **b** was the zooming in retract curve in the range of 1.2–1.7 μ m. **c**, **d** Force histogram on cancerous cells (**c**) and erythrocytes (**d**). **e**, **f** CD20 distribution map on cancerous cells (**e**) and on erythrocytes (**f**). Force maps are constructed by recording 16 × 16 force curves in 500 × 500 nm² areas on the cell surface

this heterogeneity are lipid rafts [45]. Lipid rafts are fluctuating nanoscale assemblies of sphingolipid, cholesterol, and proteins that can be stabilized to coalesce, forming platforms that function in membrane signaling and trafficking [46]. Besides, cell membrane are dynamic (proteins are free to move with the lipid bilayer), and this means that the distribution of membrane proteins on the cell surface changes dynamically. Researchers have directly observed the motion of single membrane proteins by using high-speed AFM [47]. Additionally, cell

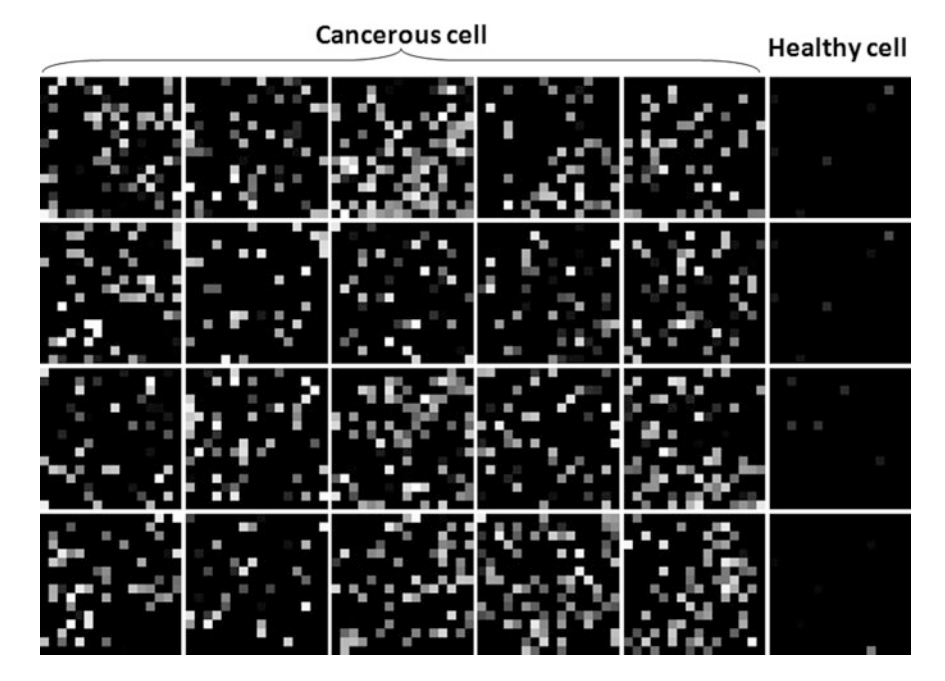


Fig. 6.25 The maps of CD20 distribution on the local surface (500×500 nm) of cancerous cells and erythrocytes [36]. Data obtained using five functionalized tips on eight cancerous cells and four erythrocytes. The gray scale bar is the same as the gray scale bar in Fig. 6.24e, f

membranes have variable membrane curvatures in different positions on the cell surface and this curvature are dynamically remodeled during physiological processes [48]. All these features of cell membranes may cause the results that the distributions of CD20s on the cancerous cell surface are non-uniform. For contrast, on the force maps of erythrocytes, there were few gray pixels and these pixels were dim.

In order to demonstrate that the maps reflect the CD20 distributions on the cell surface, verification experiments were performed, as shown in Fig. 6.26. Figure 6.26a is the merged image of optical image and fluorescence image of the clinical bone marrow cell sample and we can see two cancerous cells in the image. Under the guidance of fluorescence, AFM functionalized tips were move to the cancerous cells to image the cell morphology and obtain force curves on the cell surface. From the distribution maps (Fig. 6.26b–d), we can see that there are many gray pixels which is consistent with the results in Fig. 6.25. After blocking, arrays of force curves were obtained again on the cancerous cells, and the distribution maps are shown in Fig. 6.26e–g. We can see that after blocking, the gray pixels dramatically decreased, which is because that the CD20s on the cancerous cells had been blocked, confirming that the force maps reflect the distribution of CD20s on the cancerous cells.

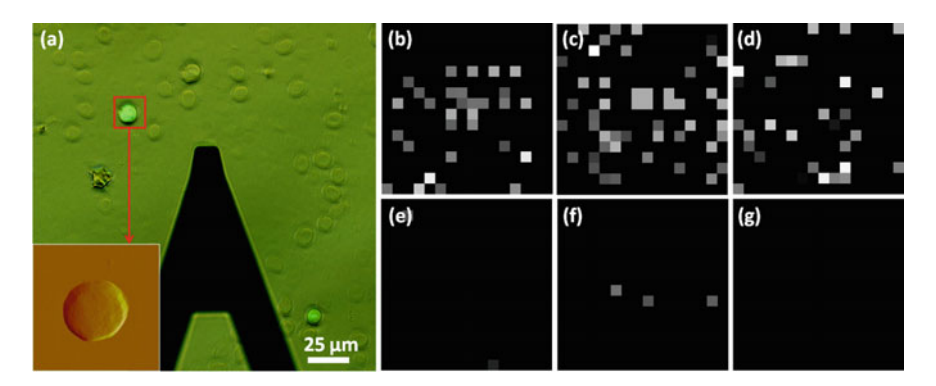


Fig. 6.26 Verification of specific CD20-rituximab interactions [36]. a Merged optical image and fluorescence image of the clinical bone marrow cell sample. The inset is the AFM image of the cancerous cell. **b**, **c**, **d** CD20 distribution maps on the cancerous cells. **e**, **f**, **g** CD20 distribution maps on the cancerous cells after blocking. The gray scale bar is the same as in Fig. 6.24e, f

Current studies about applying AFM to investigate molecular interactions are commonly performed on cell lines cultured in vitro [49], which are quite different from the cells in vivo. Detecting molecular interactions on primary cells can better reflect the real situations in vivo. Here, the methods of detecting the CD20s on primary cancerous B cells prepared from the bone marrow of clinical lymphoma patients were established based on specific ROR1 fluorescence labeling, demonstrating the capability of AFM in sensing specific membrane proteins on human primary cells.

6.2.2 Detecting FcR-Rituximab Interactions on Patient Effector Cells

The rituximab's ADCC mechanism involves two types of molecular interactions, including CD20-rituximab interactions on cancerous cells and FcR-rituximab interactions on effector cells. Hence, in order to better investigate the relationships between molecular interactions and rituximab's therapeutic outcomes, we need to study these two types of molecular interactions. In this section, FcR-rituximab interactions were probed on macrophages and patient NK cells.

(1) Probing FcR-Rituximab interactions on macrophages

FcRs, widely expressed throughout the haematopoietic system, belongs to the large immunoglobulin superfamily and are type I transmembrane glycoproteins [50]. FcRs are key players in both the afferent and efferent phase of the immune responses [51]. Binding of FcRs to the Fc portion of the antibody triggers effector functions that are important in the antibody-based immunotherapy of cancer [52]. RAW264.7 cell is a mouse macrophage cell line that has been used extensively for

studying FcR-mediated phagocytosis [53]. Here we used RAW 264.7 cells for the force spectroscopy experiments. Before AFM experiments, we examined the expression of FcR on macrophages by immunofluorescence labeling. For FcR fluorescence labeling, rituximab solution was added into the Petri dishes and incubated for 3 h at room temperature. After washing the Petri dishes with PBS for three times (each time 10 min), goat-anti-human IgG (conjugated with red-fluorescent dye) was added and incubated 30 min. After washing the Petri dishes with PBS for three times (each time 10 min), the Petri dishes were placed on AFM stage for fluorescence observation. Figure 6.27a, b are optical bright field image and corresponding FcR fluorescence image of macrophages. From the fluorescence image, we can clearly see that macrophages exhibited red fluorescence, confirming that there were FcRs on the macrophages. Under the guidance of optical microscopy (Fig. 6.27c), AFM probe was moved to macrophages to perform force spectroscopy experiments.

In previous sections, the results have shown that rituximab-tethered tips can sense the CD20 s on lymphoma cell. Here, we used the rituximab-tethered tips to sense the FcR on macrophages. Rituximabs were treated by SATP to form SH groups and then the SH groups can covalently bind to the MAL end of the NHS-PEG-MAL linker. From the manual of the supplier of SATP (Instructions SATP, Thermo Scientific, Rockford, USA), we know that SATP contains a sulfhydryl and the SATP can react with the primary amines on the protein (rituximab) to form an amide bond. Also from the manual of antibody labeling of the supplier (Antibody labeling overview, Thermo Scientific, Rockford, USA), we know that the primary amines are abundant and distributed over the entire antibody (both of the Fab and Fc region of the antibody contain primary amines). Hence, in the process of tip functionalization, it is reasonable that some SATP molecules may react with the primary amines on the Fab region of rituximab and some SATP molecules may react with the primary amines on the Fc region of rituximab. Because many rituximabs are linked to the AFM tips during the functionalization, it is probably that the tips can contain both of these two types of modified rituximabs. In fact, the following results show that rituximab-tethered tips can probe the FcR on macrophages.

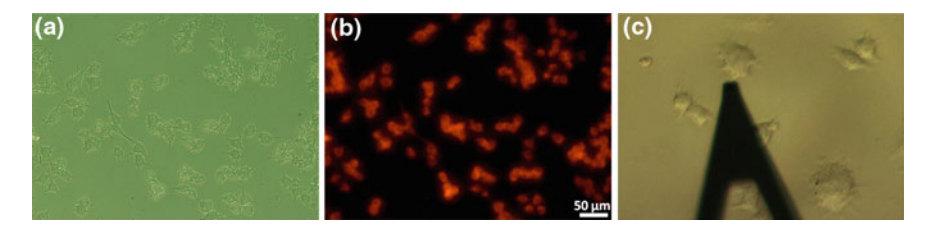


Fig. 6.27 Optical observations of FcRs on macrophages [63]. Optical bright field image (**a**) and the corresponding FcR fluorescence images (**b**) of macrophages. Under the guidance of optical microscopy (**c**), the AFM probe was moved to the macrophages

Figure 6.28 shows the results of measuring the FcR-rituximab binding forces on macrophages using rituximab-tethered tips. Figure 6.28a shows a typical force curve obtained on macrophages with specific molecular unbinding peak. The magnitude of the peak indicates the binding force (denoted by the double-headed blue arrow). When obtaining force curves on the substrate (Fig. 6.28b), the force curves are straight, and there are no specific peaks in the retract curve. After the blocking experiments (adding free rituximabs to bind the FcRs on macrophages). no specific molecular peak appeared in the retract curve (Fig. 6.28c). For each situation (on macrophages, substrate and blocked macrophages), after obtaining 500 force curves, the binding frequency is computed, as shown in Fig. 6.28c. We can see that the binding frequency on macrophages was significantly larger than on substrate and blocked macrophages, confirming the specific FcR-rituximab interactions. Figure 6.28e, f shows the FcR-rituximab binding forces measured at five different loading rates. Figure 6.28e is the histogram of FcR-rituximab binding force measured at a certain loading rate (70,000 pN/s). The Gaussian fit indicates that the mean force was 58 pN. For biomolecules, ligand-receptor affinity is mainly determined by the rate of ligand-receptor complex dissociation [54]. According to the Bell-Evans model [55, 56], the ligand-receptor unbinding force was linearly related to the logarithm of the loading rate of the external pulling force. Recent researches indicate that not only the molecular bonds but also the mechanical properties of proteins and membranes are loading-rate dependent [57]. Figure 6.28f shows the relationship between FcR-rituximab binding force and the logarithm of loading rates. We can clearly see that the FcR-rituximab binding force is linearly

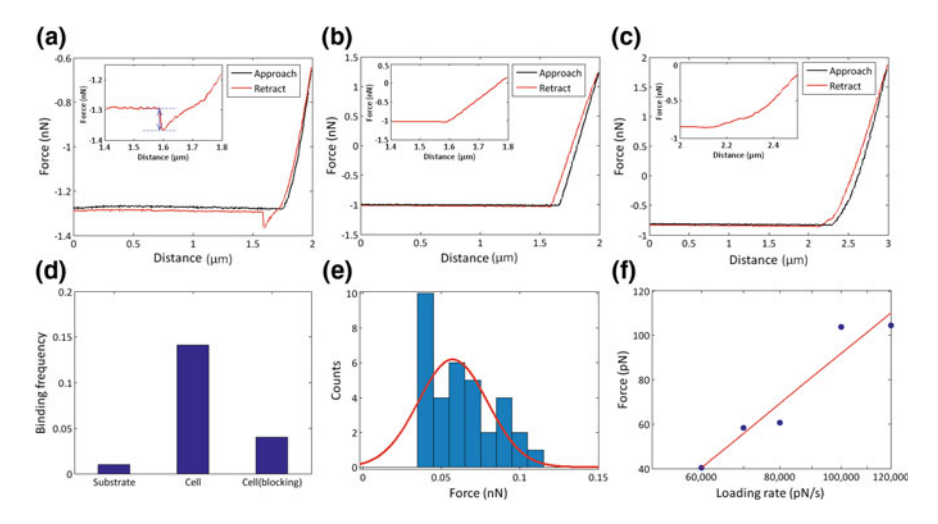


Fig. 6.28 Probing the FcR-rituximab interactions by obtaining force curves on macrophages with rituximab-conjugated tips [63]. Typical force curves obtained on macrophages (a), on substrate (b), and on macrophages after blocking (c). The insets in **a**–**c** are the enlarged views of retract curves. **d** Binding frequency. **e** Force histogram at a loading rate. **f** Forces are linearly related to the logarithm of the loading rates

related to the logarithm of the loading rate. In single-molecule dynamic force spectroscopy experiments, measuring the unbinding force at different loading rates is useful for assessing kinetic parameters of the unbinding process, including dissociation rate constant, association rate constant, and relative heights of energy barriers [58].

Figure 6.29 shows the distribution of FcRs on macrophages. We first obtained arrays (16×16) of force curves on different local areas ($500 \times 500 \text{ nm}^2$) of three macrophages. Figure 6.29a is a typical force curve with molecular specific unbinding peak. Figure 6.29b—d are the force maps. From the maps, the gray pixels indicated the FcR. We can see that the FcRs were dispersedly located on the cell surface and some FcRs aggregate. In order to verify that the maps reflect the distribution of FcR on the macrophage surface, we used the functionalized tips to obtain arrays of force curves on macrophages that had been blocked, and the results are shown in Fig. 6.29e—h. The majority of the force curves obtained on blocked macrophages did not have specific unbinding peaks, as show in Fig. 6.29e. From the maps (Fig. 6.29f—h), we can see that there were very few gray pixels. This is because that the FcRs on the cell surface had been blocked by the added rituximabs. This may

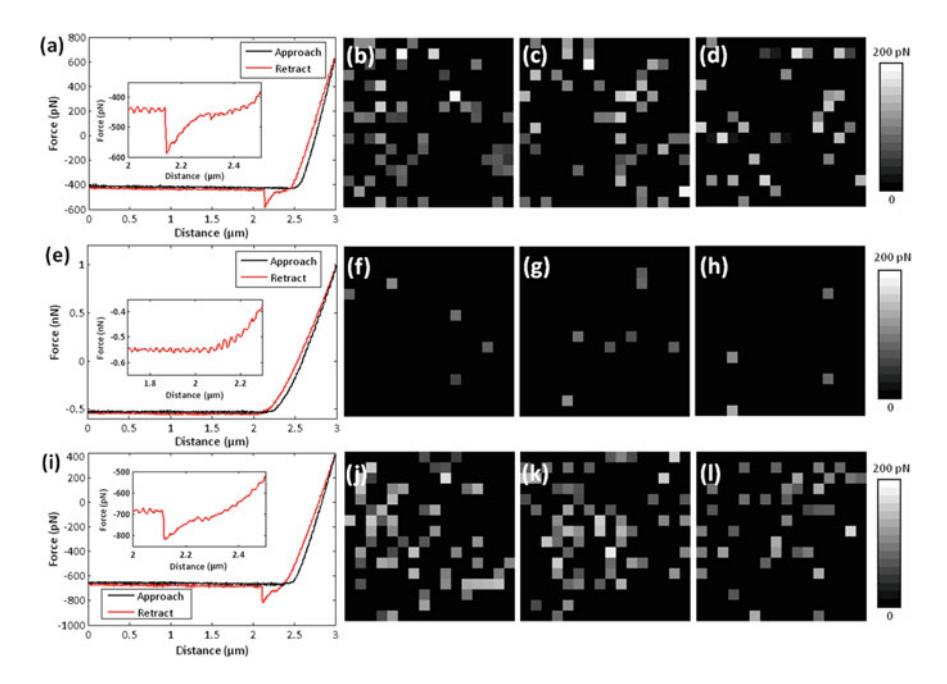


Fig. 6.29 Localizing the FcγRs on macrophages by obtaining arrays of force curves on a local area of the cell surface [63]. \mathbf{a} - \mathbf{d} are from macrophages. \mathbf{a} A typical force curve. \mathbf{b} - \mathbf{d} are force maps constructed by obtaining 16×16 force curves on 500×500 nm² area of the cell surface. \mathbf{e} - \mathbf{h} are from rituximab-blocked macrophages. \mathbf{e} A typical force curve. \mathbf{f} - \mathbf{h} Force maps. \mathbf{i} - \mathbf{l} are from macrophages (without blocking). \mathbf{i} A typical force curve. \mathbf{j} - \mathbf{l} Force maps. The insets in \mathbf{a} , \mathbf{e} and \mathbf{i} are enlarged views of retract curves

also because that the rituximab molecules on the AFM tip surface had lost activity. Hence in order to verify whether the rituximabs on the functionalized tips were still active, we used the same functionalized tips to obtain arrays of force curves on macrophages (without blocking) and the results are shown in Fig. 6.29i–l. Many force curves had specific unbinding peaks (Fig. 6.29i), and there were many gray pixels in the maps (Fig. 6.29j–l). This results demonstrate that the rituximabs on the functionalized tips were still active and the force maps correspond to the distribution of FcRs.

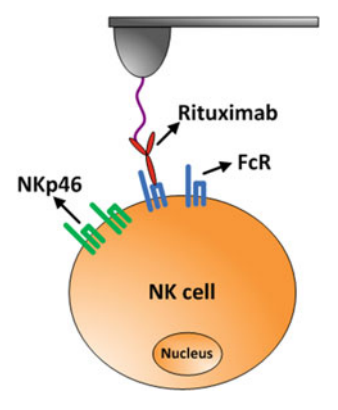
In summary, the method for probing the FcRs on effector cells was established on macrophage cell line. Based on the method, the binding force of FcR-rituximab was quantified and the distributions of FcR were mapped on macrophages. The experimental results facilitate investigating the two types of molecular interactions (CD20-rituximab, FcR-rituximab) involved in rituximab's ADCC mechanism.

(2) Probing FcR-rituximab interactions on primary NK cells from lymphoma patients

In this section, the FcR-rituximab interactions were measured on primary NK cells prepared from the bone marrow of lymphoma patients based on NKp46 fluorescence recognition, as shown in Fig. 6.30. The bone marrow biopsy samples prepared from the lymphoma patients with bone marrow invasion contain various types of cells, including tumor cells, NK cells, red blood cells, and other white blood cells. Hence, in order to investigate the molecular recognition interactions on NK cells, we need to firstly recognize the NK cells from the bone marrow cells. NKp46 is a specific cell surface marker exclusively expressed on the surface NK cells and not expressed on other cells [59]. Hence we can recognize the NK cells from the bone marrow of lymphoma patients through NKp46 fluorescence labeling. Then under the guidance of fluorescence, we can control the rituximab-tethered tip to probe the FcR-rituximab interactions on the surface of NK cells.

Figure 6.31 shows the NKp46 fluorescence labeling of peripheral blood cells and bone marrow cells prepared from lymphoma patients. For peripheral blood cells of lymphoma patients (Fig. 6.31a, b), the fluorescence images are dark and we do

Fig. 6.30 Measuring the molecular recognition interactions between FcR and rituximab on NK cells by AFM [64]



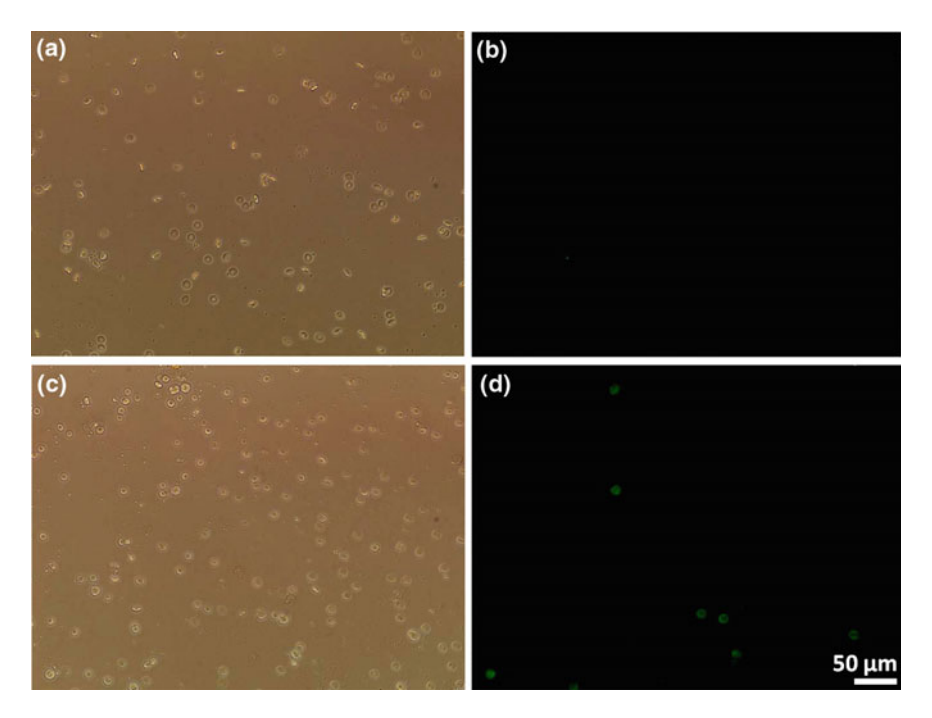


Fig. 6.31 NKp46 fluorescence labeling of peripheral blood cells and bone marrow cells from lymphoma patients [64]. **a, b** are peripheral blood cells from lymphoma patients. **a** Bright field images and **b** corresponding fluorescence images. **c, d** are bone marrow cells from lymphoma patients. **c** Bright field images and **d** corresponding fluorescence images

not see the cells that exhibit fluorescence. We know in the peripheral blood, the majority (approximately 99%) is the erythrocytes, and white blood cells make up less than 1%. Among the white blood cells, NK cells account for less than 10% [60]. Hence NK cells account for less than 0.1% in the peripheral blood cells. This very low level of NK cells in the peripheral blood cells makes it difficult to recognize the NK cells directly from the peripheral blood cells. For bone marrow cells of lymphoma patients (Fig. 6.31c, d), we can see that some cells exhibit green fluorescence. Because only NK cells express NKp46, we can conclude that these fluorescence-shining cells are the NK cells. NK cells originate, develop, and differentiate in the bone marrow [61, 62]. There are higher levels of NK cells in the bone marrow cells than in the peripheral blood cells, which facilitate the detection of NK cells directly on the bone marrow cells. In order to recognize the NK cells from peripheral blood cells, we may have to lyse the erythrocytes to eliminate the influence of erythrocytes [60] and then perform NKp46 fluorescence experiments.

Under the guidance of NKp46 fluorescence, the topography of NK cells was imaged by AFM, as shown in Fig. 6.32. Figure 6.32a, b are the bright field image and corresponding fluorescence image of the NKp46-labeled bone marrow cells. Figure 6.32c is the merged image of bright field image and fluorescence image.

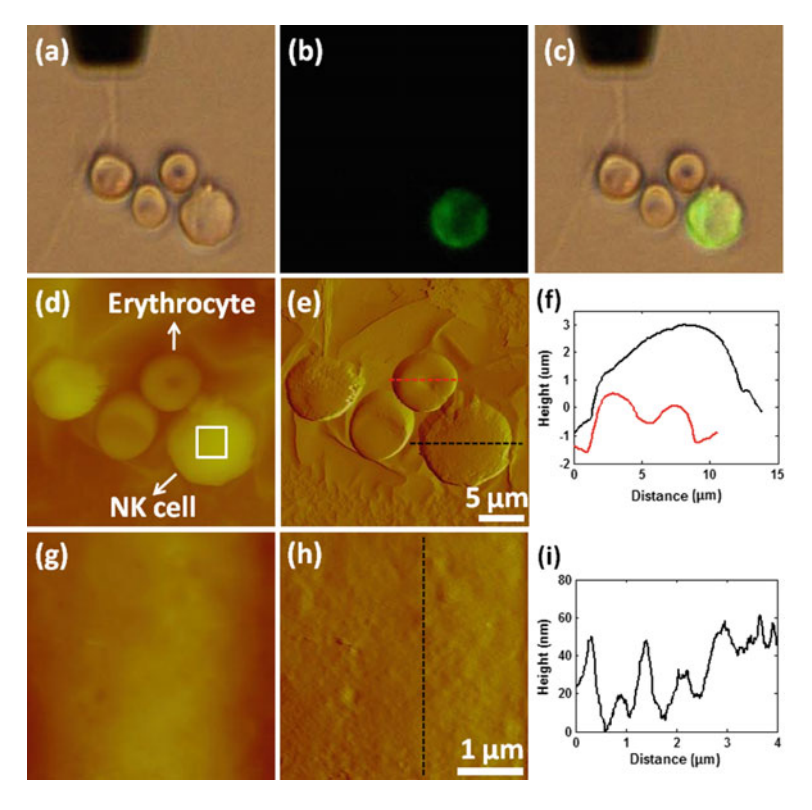


Fig. 6.32 AFM imaging of primary NK cells under the NKp46 fluorescence labeling [64]. **a** Bright field image, **b** fluorescence image, and **c** overlay image of the NKp46-labeled bone marrow cells. **d** AFM height image and **e** deflection image of the cells. **f** Section profiles. **g** AFM height image and **h** deflection image of the local area on the NK cells. **i** Section profile

There are four cells in the bright field image, among which only one cell exhibits fluorescence. The fluorescence indicated that it was a NK cell. Then the AFM probe was moved to the NK cell to obtain the AFM height image (Fig. 6.32d) and deflection image (Fig. 6.32e). The scan size was 30 μ m. From the AFM images, we can clearly see that one cell is an erythrocyte, because of the special biconcave shape of erythrocytes. The erythrocyte does not exhibit fluorescence in the fluorescence image (Fig. 6.32b); this is because erythrocytes do not express NKp46. Compared with erythrocytes, the AFM images showed that the NK cell exhibited a plump shape. Figure 6.32f is the section profiles taken along the dashed lines in Fig. 6.32e. The section curve of the erythrocyte had a hollow, which was consistent with the biconcave shape of erythrocytes. The section curves also showed that the diameter of the NK cell was about 11 μ m and the diameter of the erythrocyte was about 7.5 μ m. From the AFM images, we can discern the erythrocytes according to their special shape. Erythrocytes do not express FcR and thus can be used for negative control of molecular force measurements. Figure 6.32g, h

are the AFM height image and deflection image of the local area on the NK cell denoted by the dashed square in Fig. 6.32d. We can see that the surface of NK cells was a little rough. The section curve Fig. 6.32i showed that the NK cell had protrusions with the size 10–60 nm.

Figure 6.33 shows the results of probing FcR-rituximab interactions on primary NK cells by using rituximab-tethered tips. Figure 6.33a-c are the representative force curves with specific dissociation peaks. The left insets in Fig. 6.33a-c are the enlarged view of the retract curves in the range of 1.7–1.9 µm. The right insets in Fig. 6.33a-c are the cartoon diagrams of measuring the forces using functionalized tips. We can clearly see the specific unbinding peaks in the retract curves in Fig. 6.33a-c. The magnitude of peak (denoted by the double-head arrows) corresponded to the FcR-rituximab binding force. For control, force curves were obtained on erythrocytes. Figure 6.33d is a representative force curve obtained on erythrocytes. The left inset in Fig. 6.33d is the enlarged view of the retract curve in the range of 1.4–1.8 μm. We can see that there were no specific unbinding peaks in the retract curves. FcR are expressed on a wide range of effector cells, including macrophages, neutrophils, NK cells and dendritic cells [63, 64]. Erythrocytes do not express FcR and hence we cannot probe the specific FcR-rituximab molecular interactions. In order to demonstrate the specificity of molecular interactions, we obtained force curves on NK cells after the addition of free rituximabs. Figure 6.33e is a representative force curve obtained on blocked NK cells. The left inset in Fig. 6.33e is the enlarged view of the retract curve in the range of 1.4–1.7 μm, showing that the specific peaks vanished. This is because that the FcRs on the NK

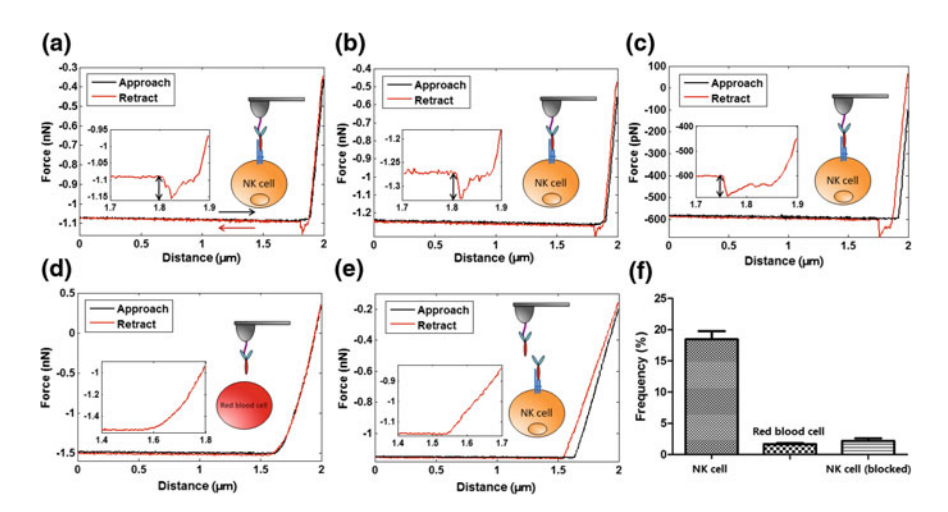


Fig. 6.33 Probing the FcR-rituximab interactions by obtaining force curves on the surface of primary NK cells with rituximab-tethered tips [64]. Representative force curves obtained on NK cells $(\mathbf{a}-\mathbf{c})$, erythrocytes (\mathbf{d}) , and rituximab-blocked NK cells (\mathbf{e}) . The insets in $\mathbf{a}-\mathbf{e}$ show the enlarged views of retract curves and the cartoon diagrams of measurements. \mathbf{f} Comparison of the molecular binding frequency observed in NK cells, erythrocytes, and rituximab-blocked NK cells

cells had been blocked by the free rituximabs. We statistically analyzed the molecular binding frequency occurred on NK cells, erythrocytes, and blocked NK cells, and the results are shown in Fig. 6.33f. We can see that the molecular binding frequency on NK cells was significantly larger than that on erythrocytes and blocked NK cells, confirming the specific FcR-rituximab interactions measured on NK cells using rituximab-conjugated tips.

Figure 6.34 shows the results of mapping the nanoscale distributions of FcRs on the surface of primary NK cells. 16×16 force curves were obtained in the local areas ($500 \times 500 \text{ nm}^2$) on the cell surface. Figure 6.34a—e are the gray maps obtained on NK cells, visually showing the distribution of FcR on NK cells. In order to demonstrate that the gray pixels corresponded to the FcRs on the NK cells, we performed blocking experiments. Figure 6.34f—j are the gray maps obtained on NK cells at different time after the addition of free rituximabs. Arrays of force curves were obtained at the different areas on the cell surface. We can see that the gray pixels decreased remarkably after the addition of rituximabs and eventually vanished about 2 h after the addition. This is because that the free rituximabs bound to the FcR on the cell surface, and as the increase of incubation time, more and more FcRs were masked by free rituximabs. The decrease of gray pixels may also be due to the lost of rituximab activity on the AFM tips, and hence we used the

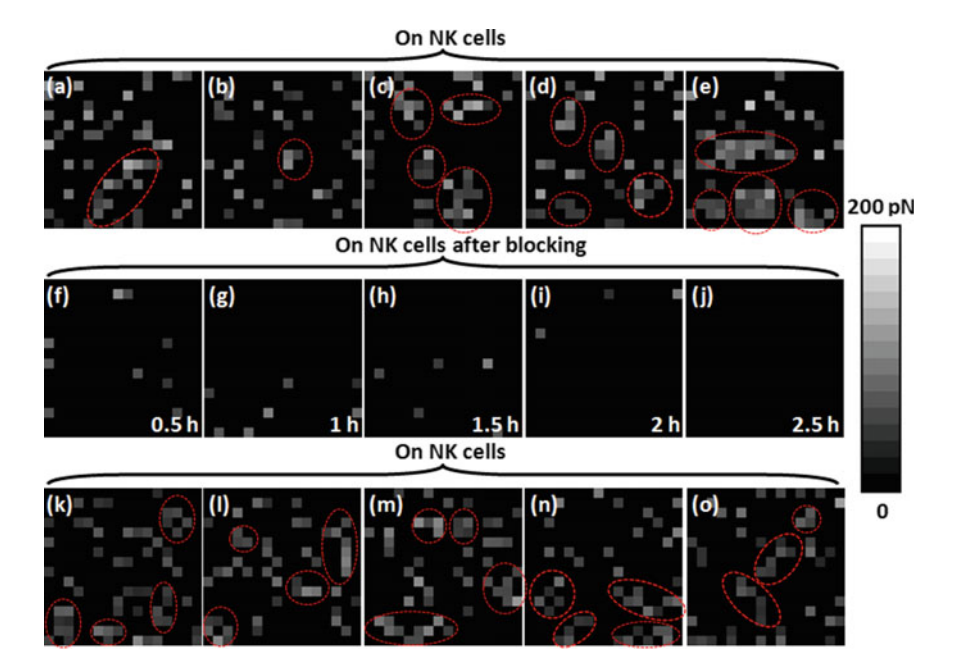


Fig. 6.34 Distributions of FcRs on the surface of primary NK cells by obtaining arrays of force curves in the local areas on the cell surface with rituximab-tethered tips [64]. **a–e** Force maps on NK cells before adding free rituximabs. **f–j** Force maps at different time after adding free rituximabs. **k–o** Force maps on NK cells (without adding rituximab)

AFM tips to obtain force curves again on NK cells which were not blocked. Figure 6.34k–o are the gray maps obtained on NK cells without blocking. We can see that many gray pixels occurred in the maps, proving that the rituximab on the AFM tips still had activities. The results in Fig. 6.34 demonstrated that the gray maps reflected the distribution of FcRs on the cell surface. From the gray maps, we can see that some FcRs clustered into nanodomains (denoted by the red dashed circles), while some FcRs distributed sparsely on the cell surface.

In summary, the experimental results demonstrate the capability of AFM in probing the FcR-rituximab interactions on primary NK cells prepared from the bone marrow of clinical lymphoma patients based on NKp46 fluorescence recognition, which is useful for in situ investigating the two types of molecular interactions (CD20-rituximab, FcR-rituximab) involved in rituximab's ADCC mechanism.

6.3 Comparison of AFM Detection Results and Clinical Therapeutic Outcomes

The established methods were applied on primary cells prepared from several B-cell NHL patients who received rituximab therapy. The results of AFM molecular measurements were compared with clinical outcomes to analyze the practical significance of detecting molecular interactions by AFM.

6.3.1 CD20-Rituximab Interaction on Patient Cancerous Cells and Clinical Efficacies

To investigate the CD20 affinity and nanoscale distribution of different lymphoma patients, we selected three B-cell NHL patients for the study. Clinical pathological tests confirmed that all of the three patients were with bone marrow infiltration. The three patients were treated by rituximab. ROR1 fluorescence labeling experiments were performed to confirm that there were ROR1s on the tumor cell surface of the three patients. The clinical information of the three patients is shown in Table 6.2. For each patient, their bone marrow cells were dropped onto the glass slides. Then chemical fixation and ROR1-fluorescence labeling were performed. Under the guidance of ROR1 fluorescence, about 10 tumor cells were selected and arrays of force curves were obtained on five different local areas on the surface of each cell using rituximab-tetered tips. Figure 6.35a-c are the CD20 binding affinities of tumor cells from patient 1, patient 2, and patient 3, respectively. The CD20 binding affinities to rituximab were computed from the force curves which had specific molecular unbinding peaks. From the histogram, the Gaussian fitting indicated that the CD20 binding affinities of the three patient were 78 ± 33 pN, 88 ± 66 pN, 80 ± 39 pN, respectively. We can see that the binding affinities were not

Case no.	Sex	Age	Tumor	Clinical therapy	Outcome
			subtype		
1	Female	64	Splenic marginal zone B-cell lymphoma	Rituximab + Fludarabine + Cyclophosphamide	Complete remission
2	Male	56	Small B-cell lymphoma	Rituximab + CHOP	Lesion stability
3	Female	51	Diffuse large B-cell lymphoma	Rituximab + CHOP	Partial remission

Table 6.2 Clinical information of three B-cell NHL patients [65]

remarkable variable between the three patients. Figure 6.35d shows the typical adhesion force maps of the three patients. To quantitatively characterize the nanoscale distribution of CD20s, we calculate the CD20 distribution frequency for each adhesion force map to characterize the CD20 density of the cells. For each adhesion force map, we can compute the number of gray and bright pixels (n), and the number of overall pixels of the adhesion force map was known $(16 \times 16 = 256)$. The CD20 distribution frequency of this adhesion force map was equal to the ratio (n/256). Figure 6.35e shows the CD20 distribution frequencies of the three patients. Analyzing the relationship between CD20 density and clinical therapy outcomes, we can find some interesting phenomenon. The combined therapy (rituximab + chemotherapy) was effective for patient 1 and patient 3, but was ineffective for patient 2. While the histogram of distribution frequencies indicated that the CD20 density of patient 2 was the smallest. This indicated that if there were more CD20s on the surface of tumor cells, the clinical efficacy of rituximab was better. However, the efficacy of patient 3 was worse than the efficacy of patient 1, while the CD20 density of patient 3 was larger than the CD20 density of patient 1. This indicated that the therapeutic effects were not linearly proportional to the CD20 density of the tumor cells. On the whole, the experimental results showed the potential links between CD20 density and rituximab's efficacies.

6.3.2 FcR-Rituximab Interaction Patient Effector Cells and Clinical Efficacies

The results of Fig. 6.35 indicate that only measuring the CD20-rituximab interactions can not fully characterize the practical effects of rituximab. Hence, we simultaneously measured the CD20-rituximab interactions on primary tumor cells and FcR-rituximab interactions on primary NK cells prepared from two B-cell NHL

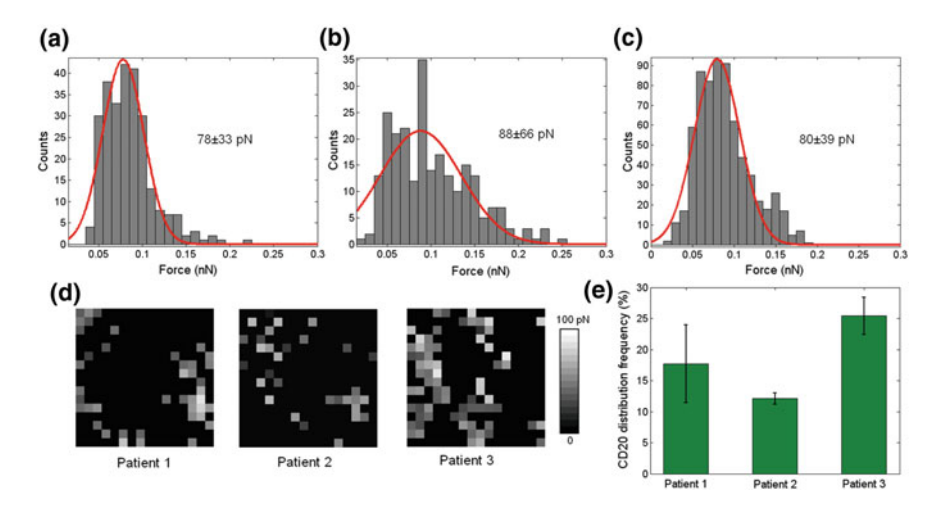


Fig. 6.35 CD20 binding affinity and distribution of different lymphoma patients [65]. Histogram and Gaussian fitting of CD20 binding affinity of patient 1 (a), patient 2 (b), and patient 3 (c). **d** Typical CD20 maps for the three patients. **e** Contrast of CD20 distribution probability of the three patients

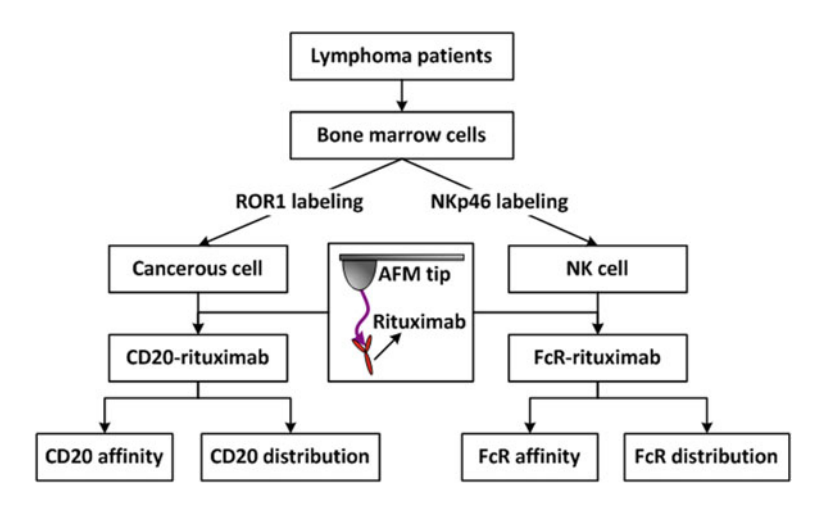


Fig. 6.36 Flow chart of simultaneously measuring CD20-rituximab interactions on primary cancerous cells and FcR-rituximab interactions on primary NK cells prepared from the bone marrow of lymphoma patients [64]

patients with bone marrow invasion. The flow chart is shown in Fig. 6.36. Cancerous cells were recognized by ROR1 fluorescence labeling and NK cells were recognized by NKp46 fluorescence labeling. Under the guidance of fluorescence, CD20-rituximab interactions were probed on cancerous cells and FcR-rituximab interactions were probed on NK cells [65].

Figure 6.37a is the histogram of FcR-rituximab binding forces measured on NK cells from patient one and Fig. 6.37b is the histogram of CD20-rituximab binding forces measured on tumor cells from patient one. The Gaussian fitting showed that the FcR-rituximab binding force was 65 ± 38 pN and the CD20-rituximab binding force was 95 \pm 46 pN. We can see that the binding force of CD20-rituximab was larger than the binding force of FcR-rituximab for patient one. Figure 6.37d, e are the histogram of FcR-rituximab binding forces measured on NK cells and the histogram of CD20-rituximab binding forces measured on tumor cells for patient two respectively. We can also see that the binding force of CD20-rituximab $(117 \pm 83 \text{ pN})$ was larger than that of FcR-rituximab (78 \pm 48 pN). Based on radioimmunoassay, the binding constant value between human CD20 and rituximab was from $2.0 \times 10^8 - 2.8 \times 10^8 \,\mathrm{M}^{-1}$ [66–68], and the binding constant between human FcR and human IgG1 was from $1.3 \times 10^{6} - 4 \times 10^{6} \,\mathrm{M}^{-1}$ [69, 70]. We know rituximab is a chimeric antibody with human IgG1 constant regions and murine variant regions [71]. FcR binds to the constant regions of rituximab and thus the binding affinity between FcR and rituximab is equal to the binding affinity between FcR and IgG1. In this work the measured CD20-rituximab binding forces were significantly larger than the FcR-rituximab binding forces, consistent with the results measured by traditional methods. Figure 6.37c shows the distribution frequency of FcR on NK cells and CD20 on tumor cells for patient one. The distribution frequency was computed according to the process in Fig. 6.35. We can see that the distribution frequency of CD20 on tumor cells (22.2%) was larger than the distribution frequency of FcR on NK cells (18.4%) for patient one. For patient two (Fig. 6.37f), the distribution frequency of FcR on NK cells (22.1%) was slightly less than the distribution frequency of CD20 on tumor cells (23.6%). One reason for the unprecedented success of rituximab in clinical practice is that CD20 is expressed at high levels on B lymphoma cells compared with most targets (often more than 250,000 molecules per cell), allowing dense accumulation of the antibody on the plasma membrane [1]. For the distribution of FcR, researches have shown that NK cells display a low level of expression of FcR on the plasma membrane [72]. Here the results obtained by SMFS showed that the distribution density of FcR on NK cells was less than the distribution density of CD20 on tumor cells for clinical patients, which was reasonable by comparing with the results obtained by traditional biochemical methods.

The clinical information of the two lymphoma patients is shown in Table 6.3. Patient one was a case of diffuse large B-cell lymphoma and patient two was a case of chronic lymphocytic leukemia. Both of the two patients were treated by combination of chemotherapy and rituximab therapy. After the treatment (6 cycles), patient one had partial remission, while patient two had complete remission. Comparing the FcR-rituximab interactions for the two patients, we can find that the FcR-rituximab binding force of patient one (Fig. 6.37a) was slightly less than the FcR-rituximab binding force of patient two (Fig. 6.37d), while the distribution density of FcR on NK cells of patient one (Fig. 6.37c) was significantly less than

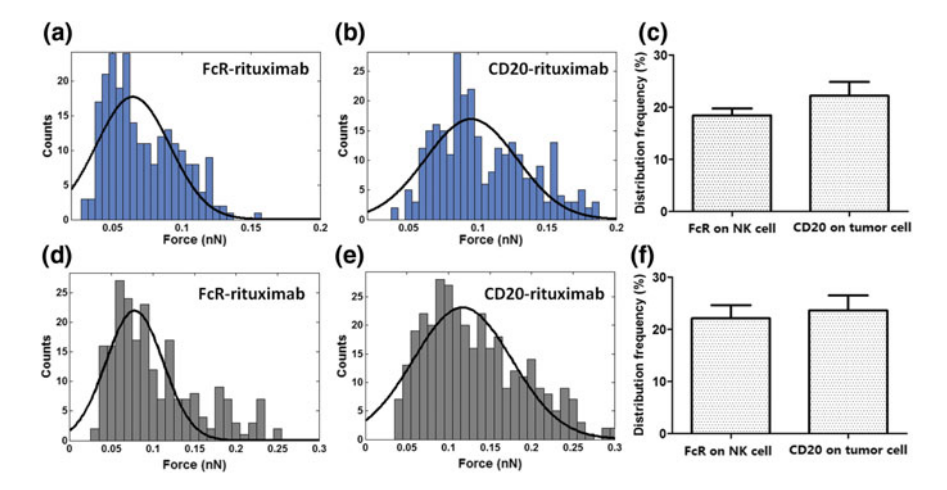


Fig. 6.37 Simultaneously measuring FcR-rituximab and CD20-rituximab interactions on primary samples from two B-cell NHL patients [64]. **a**–**c** are from patient 1. **d**–**f** are from patient 2. **a**, **d** Histogram of binding forces between FcR and rituximab measured on the surface of NK cells. **b**, **e** Histogram of binding forces between CD20 and rituximab measured on the surface of tumor cells. **c**, **f** Distribution frequency of FcR on NK cells and CD20 on tumor cells

the distribution density of FcR on tumor cells of patient two (Fig. 6.37f). Comparing the CD20-rituximab interactions, we can find that the CD20-rituximab binding force of patient one (Fig. 6.37b) was a little less than that of patient two (Fig. 6.37e), while the distribution density of CD20 on tumor cells of patient one (Fig. 6.37c) was similar to that of patient two (Fig. 6.37f). The comparing results showed that the larger of the binding affinity and distribution of FcR on NK cells and CD20 on tumor cells can get the better treatment outcomes. This can be explained that the larger binding affinity and distribution of FcR on NK cells and CD20 on tumor cells can make the connection between NK cells and tumor cells more stable. At this situation, more NK cells can be recruited to attack the tumor cells and the duration time of NK cells became longer, thus the killing effects are greatly improved. It should be noted that we only measured two patients in this study and it is difficult to discern the respective contribution of FcR-rituximab interactions and CD20-rituximab interactions from the results. In order to investigate the respective role of FcR-rituximab interactions and CD20-rituximab interactions in the rituximab clinical therapy of lymphomas, measurements on more clinical cases are needed in further studies. Collectively, the procedure of investigating the two types of molecular interactions involved in rituximab's ADCC mechanism on primary patient cells and correlating them with pratical rituximab therapeutic outcomes were established, which is useful for developing novel methods which can potentially be used to predict drug efficacies for personalized medicine.

Table 6.3 Clinical information of the two B-cell NHL patients [64]

Case	Sex	Age	Tumor subtype	Clinical therapy	Therapy	Outcome
no.					cycle	
-	Male	50	Diffuse large B-cell	Rituximab + CHOP	9	Partial remission
			lymphoma			
2	Female	47	Chronic lymphocytic	Rituximab + Fludarabine + Cyclophosphamide	9	Complete
			leukemia			remission

6.4 Summary 125

6.4 Summary

(1) AFM imaging and force measurements were combined with optical microscopy to reveal the dynamic and unique changes in cellular ultra-microstructures and cellular mechanics during rituximab's three killing mechanisms (PCD, ADCC, CDC), demonstrating the indicative role of cellular topography and mechanics in discerning different stages of rituximab's effects and also improving our understanding of rituximab's actions at the micro/nano scale.

(2) The methods which can measure the multiple types of molecular interactions (CD20-rituximab, FcR-rituximab) on primary cells prepared from the bone marrow of lymphoma patients were established based on fluorescence labeling of specific cell surface markers. The methods were applied on the primary samples of several lymphoma patients and the results demonstrated the close links between AFM-obtained molecular information (binding affinity, distribution density) and rituximab's pratical efficacies.

References

- Li M, Liu L, Xi N et al (2011) Imaging and measuring the rituximab-induced changes of mechanical properties in B-lymphoma cells using atomic force microscopy. Biochem Biophys Res Commun 404:689–694
- Li M, Liu L, Xi N et al (2012) Drug-induced changes of topography and elasticity in living B lymphoma cells based on atomic force microscopy. Acta Phys Chim Sin 28:1502–1508
- 3. Li M, Liu L, Xi N et al (2016) Applications of atomic force microscopy in exploring drug actions in lymphoma-targeted therapy at the nanoscale. Bionanoscience 6:22–32
- Hu M, Wang J, Zhao H et al (2009) Nanostructure and nanomechanics analysis of lymphocyte using AFM: from resting, activated to apoptosis. J Biomech 42:1513–1519
- Cai X, Yang X, Cai J et al (2010) Atomic force microscope-related study membrane-associated cytotoxicity in human pterygium fibroblasts induced by mitomycin C. J Phys Chem B 114:3833–3839
- Beers SA, Chan CHT, French RR et al (2010) CD20 as a target for therapeutic type I and II monoclonal antibodies. Semin Hematol 47:107–114
- El-Kirat-Chatel S, Dufrene YF (2012) Nanoscale imaging of the candida-macrophage interaction using correlated fluorescence-atomic force microscopy. ACS Nano 6: 10792–10799
- May RC, Machesky LM (2001) Phagocytosis and the actin cytoskeleton. J Cell Sci 114: 1061–1077
- McEarchern JA, Oflazoglu E, Francisco L et al (2007) Engineered anti-CD70 antibody with multiple effector functions exhibits in vitro and in vivo antitumor activities. Blood 109: 1185–1192
- Beers SA, French RR, Chan HTC et al (2010) Antigenic modulation limits the efficacy of anti-CD20 antibodies: implications for antibody selection. Blood 115:5191–5201
- Chen YY, Wu CC, Hsu JL et al (2009) Surface rigidity change of Escherichia coli after filamentous bacteriophage infection. Langmuir 25:4607–4614
- 12. Ohnesorge FM, Horber JKH, Haberle W et al (1997) AFM review study on pox viruses and living cells. Biophys J 73:2183–2194
- 13. Mogilner A, Keren K (2009) The shape of motile cells. Curr Biol 19:R762-R771

- Keren K, Pincus Z, Allen GM et al (2008) Mechanism of shape determination in motile cells. Nature 453:475–480
- 15. Pham T, Mero P, Booth JW (2011) Dynamic of macrophage trogocytosis of rituximab-coated B cells. Plos One 6:e14498
- Pollard TD (2003) The cytoskeleton, cellular motility and the reductionist agenda. Nature 422:741–745
- Kagiwada H, Nakamura C, Kihara T et al (2010) The mechanical properties of a cell, as determined by its actin cytoskeleton, are important for nanoneedle insertion into a living cell. Cytoskeleton 67:496–503
- 18. Greenberg S, Grinstein S (2002) Phagocytosis and innate immunity. Curr Opin Immunol 14:136–145
- Li M, Liu L, Xi N et al (2014) Nanoscale imaging and morphological analysis of Fc receptor-mediated macrophage phagocytosis against cancer cells. Langmuir 30:1609–1621
- 20. Manches O, Lui G, Chaperot L et al (2003) In vitro mechanisms of action of rituximab on primary non-Hodgkin lymphomas. Blood 101:949–954
- Adams GP, Weiner LM (2005) Monoclonal antibody therapy of cancer. Nat Biotechnol 23:1147–1157
- 22. Manches O, Lui G, Chaperot L et al (2003) In vitro mechanisms of action of rituximab on primary non-Hodgkin lymphomas. Blood 101:949–954
- Shan D, Ledbetter JA, Press OW (1998) Apoptosis of malignant human B cells by ligation of CD20 with monoclonal antibodies. Blood 91:1644–1652
- Li M, Liu L, Xi N et al (2015) Quantitative analysis of drug-induced complement-mediated cytotoxic effect on single tumor cells using atomic force microscopy and fluorescence microscopy. IEEE Trans Nanobiosci 14:84–94
- 25. Tegla CA, Cudrici C, Patel S et al (2011) Membrane attack by complement: the assembly and biology of terminal complement complexes. Immunol Res 51:45–60
- Weiland MH, Qian Y, Sodetz JM (2014) Membrane pore formation by human complement: functional importance of the transmembrane β-hairpin (TMH) segments of C8α and C9. Mol Immunol 57:310–316
- Tschopp J, Podack ER, Muller-Eberhard HJ (1982) Ultrastructure of the membrane attack complex of complement: detection of the tetramolecular C9-polymerizing complex C5b-8.
 Proc Natl Acad Sci USA 79:7474

 –7478
- 28. Cuerrier CM, Lebel R, Grandbois M (2007) Single cell transfection using plasmid decorated AFM probes. Biochem Biophys Res Commun 355:632–636
- 29. Vakarelski IU, Brown SC, Higashitani K et al (2007) Penetration of living cell membranes with fortified carbon nanotube tips. Langmuir 23:10893–10896
- Lam WA, Rosenbluth MJ, Fletcher DA (2007) Chemotherapy exposure increases leukemia cell stiffness. Blood 109:3505–3508
- 31. Fletcher DA, Mullins RD (2010) Cell mechanics and the cytoskeleton. Nature 463:485-492
- 32. Lombardi ML, Lammerding J (2010) Altered mechanical properties of the nucleus in disease. Methods Cell Biol 98:121–141
- 33. Yamada KM, Cukierman E (2007) Modeling tissue morphogenesis and cancer in 3D. Cell 130:601–610
- Li M, Xiao X, Liu L et al (2013) Atomic force microscopy study of the antigen-antibody binding force on patient cancer cells based on ROR1 fluorescence recognition. J Mol Recognit 26:432–438
- 35. Humburg MA, Collins FS (2010) The path to personalized medicine. N Engl J Med 363: 301–304
- 36. Li M, Xiao X, Liu L et al (2013) Nanoscale mapping and organization analysis of target proteins on cancer cells from B-cell lymphoma patients. Exp Cell Res 319:2812–2821
- Baskar S, Kwong K, Hofer T et al (2008) Unique cell surface expression of receptor tyrosine kinase ROR1 in human B-cell chronic lymphocytic leukemia. Clin Cancer Res 14:396–404

References 127

38. Fukuda T, Chen L, Endo T et al (2008) Antisera induced by infusions of autologous Ad-CD154-leukemia B cells identify ROR1 as an oncofetal antigen and receptor for Wnt5a. Proc Natl Acad Sci USA 105:3047–3052

- Uhrmacher S, Schmidt C, Erdfelder F et al (2011) Use of the receptor tyrosine kinase-orphan receptor 1(ROR1) as a diagnostic tool in chronic lymphocytic leukemia (CLL). Leuk Res 35:1360–1366
- 40. Barna G, Mihalik R, Timar B et al (2011) ROR1 expression is not a unique marker of CLL. Hematol Oncol 29:17–21
- 41. Bicocca VT, Chang BH, Masouleh BK et al (2012) Crosstalk between ROR1 and the pre-B cell receptor promotes survival of t (1;19) acute lymphoblastic leukemia. Cancer Cell 22: 656–667
- 42. Hanahan D, Weinberg RA (2000) The hallmarks of cancer. Cell 100:57-70
- 43. Hinterdorfer P, Dufrene YF (2006) Detection and localization of single molecular recognition events using atomic force microscopy. Nat Methods 3:347–355
- 44. Lee CK, Wang YM, Huang LS et al (2007) Atomic force microscopy: determining of unbinding force, off rate and energy barrier for protein-ligand interaction. Micron 38:446–461
- Sanchez SA, Tricerri MA, Gratton E (2012) Laurden generalized polarization fluctuations measures membrane packing micro-heterogeneity in vivo. Proc Natl Acad Sci USA 109:7314–7319
- Lingwood D, Simons K (2010) Lipid rafts as a membrane-organizing principle. Science 327:46–50
- 47. Casuso I, Khao J, Chami M et al (2012) Characterization of the motion of membrane proteins using high-speed atomic force microscopy. Nat Nanotechnol 7:525–529
- McMahon HT, Gallop JL (2005) Membrane curvature and mechanisms of dynamic cell membrane remodeling. Nature 438:590–596
- 49. Dufrene YF, Evans E, Engel A et al (2011) Five challenges to bringing single-molecule force spectroscopy into living cells. Nat Methods 8:123–127
- Nimmerjahn F, Ravetch JV (2008) Fc receptors as regulators of immune response. Nat Rev Immunol 8:34–47
- 51. Nimmerjahn F, Ravetch JV (2006) Fc receptors: old friends and new family members. Immunity 24:19–28
- Weiner LM, Murray JC, Shuprine CW (2012) Antibody-based immunotherapy of cancer. Cell 148:1081–1084
- 53. Pham T, Mero P, Booth JW (2011) Dynamics of macrophage trogocytosis of rituximab-coated B cells. PLoS ONE 6:e14498
- Shi X, Xu L, Yu J et al (2009) Study of inhibition effect of Herceptin on interaction between Heregulin and ErbB receptors HER3/HER2 by single-molecule force spectroscopy. Exp Cell Res 315:2847–2855
- 55. Bell GI (1978) Models for the specific adhesion of cells to cells. Science 200:618-627
- Evans E, Ritchie K (1997) Dynamic strength of molecular adhesion bonds. Biophys J 72:1541–1555
- Medalsy ID, Muller DJ (2013) Nanomechanical properties of proteins and membranes depend on loading rate and electrostatic interactions. ACS Nano 7:2642–2650
- 58. Zhang X, Shi X, Xu L et al (2013) Atomic force microscopy study of the effect of HER2 antibody on EGF mediated ErbB ligand-receptor interaction. Nanomedicine 9:627–635
- Jaron-Mendelson M, Yossef R, Appel MY et al (2012) Dimerization of NKp46 receptor is essential for NKp46-mediated lysis: characterization of the dimerization site by epitope mapping. J Immunol 188:6165–6174
- Mselle TF, Howell AL, Ghosh M et al (2009) Human uterine natural killer cells but not blood natural killer cells inhibit human immunodeficiency virus type 1 infection by secretion of CXCL12. J Virol 83:11188–11195
- 61. Silva MRG, Hoffman R, Srour EF et al (1994) Generation of human natural killer cells from immature progenitors does not require marrow stromal cells. Blood 84:841–846

- 62. Santo JPD, Vosshenrich CAJ (2006) Bone marrow versus thymic pathways of natural killer cell development. Immunol Rev 214:35–46
- Li M, Liu L, Xi N et al (2013) Imaging and measuring the biophysical properties of Fc gamma receptors on single macrophages using atomic force microscopy. Biochem Biophys Res Commun 438:709–714
- 64. Li M, Xiao X, Zhang W et al (2014) AFM analysis of the multiple types of molecular interactions involved in rituximab lymphma therapy on patient tumor cells and NK cells. Cell Immunol 290:233–244
- 65. Li M, Xiao X, Zhang W et al (2014) Nanoscale distribution of CD20 on B-cell lymphoma tumour cells and its potential role in the clinical efficacy of rituximab. J Microsc 254:19–30
- 66. Tan L, Lin P, Chisti MM et al (2013) Real time analysis of binding between rituxima (anti-CD20 antibody) and B lymphoma cells. Anal Chem 85:8543–8551
- 67. Smith MR (2003) Rituximab (monoclonal anti-CD20 antibody): mechanisms of action and resistance. Oncogene 22:7359–7368
- Silverman GJ, Weisman S (2003) Rituximab therapy and autoimmune disorders: prospects for anti-B cell therapy. Arthritis Rheum 48:1484–1492
- 69. Galon J, Robertson MW, Galinha A et al (1997) Affinity of the interaction between Fc gamma receptor type III (FcγRIII) and monomeric human IgG subclasses role of FcγRIII glycosylation. Eur J Immunol 27:1928–1932
- 70. Bruhns P, Iannascoli B, England P et al (2009) Specificity and affinity of human Fcγ receptors and their polymorphic variants for human IgG subclasses. Blood 113:3716–3725
- Maloney DG (2012) Anti-CD20 antibody therapy for B-cell lymphomas. N Engl J Med 366:2008–2016
- Fernandez-Segura E, Garcia JM, Lopez-Escamez JA et al (1994) Surface expression and distribution of Fc receptor III (CD16 molecule) on human natural killer cells and polymorphonuclear neutrophils. Microsc Res Tech 28:277–285

Chapter 7 Conclusion and Future Work

7.1 Conclusion

In this thesis, in order to address the issue of variable therapeutic outcomes between different B-cell NHL patients in the rituximab targeted therapy, series methods for in situ quantitatively detecting and characterizing the multiple physical properties of single cells and single molecules based on AFM nanorobotics have been established, including cellular immobilization, cellular morphological imaging, cellular mechanical measurement, molecular force measurement and visually mapping of membrane protein on cell surface. With these methods, systematic studies have been performed on both cell lines cultured in vitro and primary cells from clinical lymphoma patients to investigate the rituximab's actions. The experimental results revealed the close links between cellular/molecular physical properties and clinical drug efficacy, providing a useful exploration for promoting the biomedical applications of nanorobotics.

The innovation of the thesis includes:

- (1) A three-dimensional immobilization method based on micropillar/well mechanical trapping and poly-L-lysine electrostatic adsorption was developed for observing living mammalian suspended cells by AFM nanorobotics. Based on the method, single living lymphoma cells were firmly immobilized both in horizontal direction and in vertical direction, which allows visualizing the ultra-microstructures of cell surface, significantly improving the detection accuracy of nanorobotics on living mammalian suspended cells in aqueous conditions.
- (2) For the requirements of label-free detecting the physiological properties of living cells and native molecules with high-resolution in the field life sciences, a series of single-cell and single-molecule methods were established based on AFM nanorobotics, which allow the measurements of multiple cellular and

- molecular parameters (including cellular topography, cellular mechanics, molecular binding affinity, and molecular distribution density on cell surface), laying a solid foundation for the biomedical applications of AFM nanorobotics.
- (3) The established AFM single-cell and single-molecule detection methods were applied on the rituximab therapy of B-cell NHL and the experimental results reveal the dynamic changes of cellular ultra-microstructures and cellular mechanics during the three killing mechanisms (PCD, ADCC, CDC) of rituximab, improving our understanding of rituximab's actions. With the assistance of fluorescence labeling of cell surface specific markers, primary cells prepared from clinical lymphoma patients were examined and the results reveal the potential significance of molecular interactions in the clinical rituximab treatment, providing a feasible idea for developing novel methods for drug evaluation and efficacy prediction based on AFM nanorobotics.

The contribution of the thesis in automation and robotics includes:

- (1) Current studies of nanorobotics mainly focus on engineering fields, such as nanomanipulation and nanofabrication. The requirements of single-cell and single-molecule techniques in life sciences presents nanorobotics with huge opportunities. This thesis established series methods based on AFM nanorobotics to characterize the physical properties of single cells and single molecules, which significantly enhances the performance and functions of nanorobotics for biomedical applications.
- (2) The applications of AFM single-cell and single-molecule techniques in clinical cancer treatment were explored, which demonstrated the abilities of AFM in detecting the biophysical properties of human primary cells. The investigations on the primary cells prepared from the bone marrow of lymphoma patients showed the correlation between quantitative molecular parameters obtained by AFM and practical rituximab outcomes, providing a new idea for promoting the biomedical applications of nanorobotics.

7.2 Future Work

Future work may be carried out in the following points:

(1) ADCC mechanisms plays an important role in rituximab's anti-cancer effects. ADCC involves two types of effector cells, including macrophages which can engulf target cells and NK cells which can release cytotoxin to kill target cells. During ADCC, the F_{ab} portion of rituximab binds to CD20 on lymphoma cells, and the F_c portion of rituximab binds to FcR on effector cells. The thesis investigates the CD20-rituximab interactions on primary lymphoma cells and the FcR-rituximab interactions on primary NK cells from clinical lymphoma

7.2 Future Work 131

patients. In order to better understand the role of ADCC in rituximab's actions, directly investigating the FcR-rituximab interactions on primary macrophages from lymphoma patients is required, which will facilitates analyzing the exact contribution of macrophages and NK cells in rituximab's practical efficacies.

- (2) Primary cell samples from five B-cell NHL patients were tested and the experimental results showed the active role of the two types of rituximab's molecular interactions (CD20-rituximab and FcR-rituximab) in the practical therapeutic outcomes of rituximab. However, it should be noted that the number of tested lymphoma cases in the thesis is small and the situations (e.g., tumor subtype, treatment, sex, age) for these patients are diverse. In order to obtain results with statistical significance, applying the established methods to examine primary samples from more B-cell NHL patients is required. As the increase of primary samples, it is necessary to investigate the relation model between AFM-obtained molecular information and clinical rituximab therapeutic outcomes. In addition, observing the dynamics of molecular behaviors during the progress of clinical treatment will be meaningful.
- (3) The thesis measured the Young's modulus of cells to characterize cellular mechanics. Though Young's modulus has been an effective biomarker for indicating the states of cancerous cells, other mechanical behaviors of cells are involved in the metastasis of tumor, such as adhesion characteristics and rheological properties. During metastasis, cancerous cells need to firstly detach from the primary tissue [1], whereas the rheological behaviors of cells are closely related to the physiological functions of cells [2]. By attaching single cells onto the cantilever of AFM and then recording force curves on cells, adhesion forces between cells can be quantified [3]. By controlling AFM tip to perform stress relaxation experiments on cells, cellular viscoelasticity can be measured [4]. In order to examine the indicative role of adhesion characteristics and rheological properties, direct comparison studies on cancerous cells and their normal counterparts, particularly on primary cells prepared from clinical cancer patients, are required.
- (4) Several issues regarding the mechanical detection of clinical samples need to be resolved. Current studies have confirmed the indicative role of cell mechanics in discerning different stages of cancer. However, due to the complexity of biological systems, it may require a long time to realize the practical applications of mechanical detection. For clinical applications, the procedures of clinical sample preparation and AFM measurements need to be standardized and the related value ranges of cancerous cells and normal cells need to be confirmed. However, tumor tissue is highly heterogeneous. Not only there are genetic and phenotypic variations between individuals with the same tumor type (intertumor heterogeneity), but also there are subclonal diversities within a tumor (intratumor heterogeneity) [5], which present difficulties for sample preparation. In addition, tumor tissues contain cancerous cells, healthy cells (e.g., fibroblasts), vessels (e.g., blood vessel and lymphatic vessel), and

extracellular matrices [6]. Tumor microenvironment plays an important role in regulating tumor progression and metastasis [7], and thus combing AFM with other techniques (e.g., fluorescence) to discriminate the particular components in tumor microenvironment may help us to better understand the mechanical behaviors of tumor tissues.

References

- Wirtz D, Konstantopoulos K, Searson PC (2011) The physics of cancer: the role of physical interactions and mechanical forces in metastasis. Nat Rev Cancer 11:512–522
- Zhou EH, Martinez FD, Fredberg JJ (2013) Cell rheology: mush rather than machine. Nat Mater 12:184–185
- 3. Smolyakov G, Thiebot B, Campillo C et al (2016) Elasticity, adhesion, and tether extrusion on breast cancer cells provide a signature of their invasive potential. ACS Appl Mater Interfaces 8:27426–27431
- 4. Li M, Liu L, Xiao X et al (2016) Viscoelastic properties measurement of human lymphocytes by atomic force microscopy based on magnetic beads cell isolation. IEEE Trans Nanobiosci 15:398–411
- Burrell RA, McGranahan N, Bartek J et al (2013) The causes and consequences of genetic heterogeneity in cancer evolution. Nature 501:338–345
- Junttila MR, Sauvage FJ (2013) Influence of tumour microenvironment heterogeneity on therapeutic response. Nature 501:346–354
- Quail DF, Joyce JA (2013) Microenvironmental regulation of tumor progression and metastasis. Nat Med 19:1423–1437

Curriculum Vitae



Mi Li
Associate Professor
State Key Laboratory of Robotics
Shenyang Institute of Automation
Chinese Academy of Sciences
Shenyang, China
E-mail: limi@sia.cn

Education:

2009.03–2015.01 Ph.D. in Pattern Recognition and Intelligent Systems. Shenyang Institute of Automation, Chinese Academy of Sciences, Shenyang, China 2006.09–2008.12 M.E. in Pattern Recognition and Intelligent Systems. College of Automation, Huazhong University of Science and Technology, Wuhan, China 2002.09–2006.06 B.E. in Software Engineering. College of Software, Huazhong University of Science and Technology, Wuhan, China

Career:

2016.01-now Associate Professor, Shenyang Institute of Automation, Chinese Academy of Sciences, Shenyang, China

2016.09–2017.08 Visiting Scholar, Department of Biomedical Engineering, The Ohio State University, Columbus, USA

2015.02–2015.12 Assistant Professor, Shenyang Institute of Automation, Chinese Academy of Sciences, Shenyang, China

2014.03–2015.01 Assistant Professor, Shenyang Institute of Automation, Chinese Academy of Sciences, Shenyang, China

134 Curriculum Vitae

Awards:

- 1. Springer Theses Award, Germany (2017)
- 2. Outstanding Doctoral Dissertation Award, Chinese Academy of Sciences (2016)
- 3. Special Prize of President Scholarship for Postgraduate Students, Chinese Academy of Sciences (2015)
- 4. Zhuliyuehua Scholarship for Excellent Ph.D. Students, Chinese Academy of Sciences (2014)
- 5. National Scholarship for Ph.D. Students, Ministry of Education of China (2013)
- 6. National Scholarship for Ph.D. Students, Ministry of Education of China (2012)
- 7. President Scholarship for Postgraduate Students, Chinese Academy of Sciences (2012)
- 8. BHP Billiton Scholarship for Postgraduate Students, Chinese Academy of Sciences (2012)
- 9. Pacemaker to Merit Student, Graduate University of Chinese Academy of Sciences (2011)

Selected publication lists:

- Mi Li, Haichang Li, Xiangguang Li, Hua Zhu, Zihui Xu, Lianqing Liu, Jianjie Ma, Mingjun Zhang. A bioinspired alginate-gum arabic hydrogel with micro-/ nanoscale structures for controlled drug release in chronic wound healing. ACS Applied Materials & Interfaces, 2017, 9(27): 22160–22175.
- 2. **Mi Li**, Dan Dang, Lianqing Liu, Ning Xi, Yuechao Wang. Atomic force microscopy in characterizing cell mechanics for biomedical applications: a review. **IEEE Transactions on Nanobioscience**, 2017, 16(6): 523–540.
- 3. **Mi Li**, Lianqing Liu, Ning Xi, Yuechao Wang. Applications of micro/nano automation technology in detecting cancer cells for personalized medicine. **IEEE Transactions on Nanotechnology**, 2017, 16(2): 217–229.
- Mi Li, Lianqing Liu, Xiubin Xiao, Ning Xi, Yuechao Wang. The dynamic interactions between chemotherapy drugs and plasmid DNA investigated by atomic force microscopy. SCIENCE CHINA Materials, 2017, 60(3): 269–278.
- Mi Li, Xiubin Xiao, Lianqing Liu, Ning Xi, Yuechao Wang. Nanoscale quantifying the effects of targeted drug on chemotherapy in lymphoma treatment using atomic force microscopy. IEEE Transactions on Biomedical Engineering, 2016, 63(10): 2187–2199.
- Mi Li, Lianqing Liu, Xiubin Xiao, Ning Xi, Yuechao Wang. Viscoelastic properties measurement of human lymphocytes by atomic force microscopy based on magnetic beads cell isolation. IEEE Transactions on Nanobioscience, 2016, 15(5): 398–411.
- Mi Li, Xiubin Xiao, Lianqing Liu, Ning Xi, Yuechao Wang. Rapid recognition and functional analysis of membrane proteins on human cancer cells using atomic force microscopy. Journal of Immunological Methods, 2016, 436: 41–49.

Curriculum Vitae 135

8. **Mi Li**, Lianqing Liu, Ning Xi, Yuechao Wang. Nanoscale monitoring of drug actions on cell membrane using atomic force microscopy. **Acta Pharmacologica Sinica**, 2015, 36(7): 769–782.

- 9. **Mi Li**, Lianqing Liu, Ning Xi, Yuechao Wang, Xiubin Xiao, Weijing Zhang. Quantitative analysis of drug-induced complement-mediated cytotoxic effect on single tumor cells using atomic force microscopy and fluorescence microscopy. **IEEE Transactions on Nanobioscience**, 2015, 14(1): 84–94.
- 10. **Mi Li**, Lianqing Liu, Ning Xi, Yuechao Wang, Xiubin Xiao, Weijing Zhang. Nanoscale imaging and mechanical analysis of Fc receptor-mediated macrophage phagocytosis against cancer cells. **Langmuir**, 2014, 30(6): 1609–1621.
- 11. **Mi Li**, Xiubin Xiao, Weijing Zhang, Lianqing Liu, Ning Xi, Yuechao Wang. AFM analysis of the multiple types of molecular interactions involved in rituximab lymphoma therapy on patient tumor cells and NK cells. **Cellular Immunology**, 2014, 290(2):233–244.
- 12. **Mi Li**, Xiubin Xiao, Lianqing Liu, Ning Xi, Yuechao Wang, Zaili Dong, Weijing Zhang. Nanoscale mapping and organization analysis of target proteins on cancer cells from B-cell lymphoma patients. **Experimental Cell Research**, 2013, 319(18):2812–2821.
- 13. **Mi Li**, Xiubin Xiao, Lianqing Liu, Ning Xi, Yuechao Wang, Zaili Dong, Weijing Zhang. Atomic force microscopy study of the antigen-antibody binding force on patient cancer cells based on ROR1 fluorescence recognition. **Journal of Molecular Recognition**, 2013, 26(9):432–438.
- Mi Li, Lianqing Liu, Ning Xi, Yuechao Wang, Zaili Dong, Xiubin Xiao, Weijing Zhang. Atomic force microscopy imaging and mechanical properties measurement of red blood cells and aggressive cancer cells. SCIENCE CHINA Life Sciences, 2012, 55(11): 968–973.
- 15. Mi Li, Lianqing Liu, Ning Xi, Yuechao Wang, Zaili Dong, Osamu Tabata, Xiubin Xiao, Weijing Zhang. Imaging and measuring the rituximab-induced changes of mechanical properties in B-lymphoma cells using atomic force microscopy. Biochemical and Biophysical Research Communications, 2011, 404(2):689–694.